rnal of Research of the National Bureau of Standards Vol. 48, No. 4, April 1952 Research Paper 2312

Pressure-Humidity Apparatus[1]

Arnold Wexler and Raymond D. Daniels, Jr.

An apparatus for producing atmospheres of known relative humidity, based on the "two-pressure principle", is described. It has a working space (test chamber) of 1 cubic foot, in which the relative humidity may be varied and controlled from 10 to 98 percent, the temperature from −40° to +40° C, the air flow up to 150 liters per minute, and the test-chamber pressure from ½ to 2 atmospheres. The humidity in the test chamber may be set and maintained to an accuracy of at least ½ of 1-percent relative humidity.

1. Introduction

The pressure-humidity equipment is a laboratory apparatus for producing atmospheres of known relative humidity by control of the pressure in the test chamber of air saturated at a higher pressure. As this apparatus was developed primarily for hygrometer research and calibration, especially on electric hygrometer elements, which, during use, are subjected to a wide temperature range, it was essential that the temperature of the working space should be adequately controlled and maintained at any desired value from −40° to +40° C. Futhermore, it was desirable that any relative humidity, from 10 to 98 percent, should be conveniently produced and that a change could be made rapidly from any one value of relative humidity to any other value. Finally, it was also desirable to have a means of varying the rate of air flow through the working space, selected to have a volume of about 1 ft³.

An apparatus has been developed that successfully meets the above requirements. It operates on what may be called the "two-pressure principle." Basically, the method, shown in elemental schematic form in figure 1, involves saturating air, or any gas, with water vapor at a high pressure and then expanding the gas to a lower pressure. If the temperature is held constant during saturation and upon expansion, and the perfect gas laws are assumed to be obeyed, then the relative humidity, RH, at the lower pressure, P_t, will be the ratio of the absolute values of the lower pressure, P_t, to the higher pressure, P_s, that is, $RH=100\times P_t/P_s$.

Water vapor-air mixtures depart from ideal gas behavior, so that the simple pressure ratio does not strickly define the relative humidity. Weaver [2, 3] has shown that an empirical equation of the form

$$RH=100\times\frac{P_t}{P_s}\frac{(1-KP_t)}{(1-KP_s)},$$

where the constant K has a value of 0.00017 when the pressure is expressed in pounds per square inch, more closely yields the true relative humidity. The magnitude of the correction introduced by the term $(1-KP_t)/(1-KP_s)$ is shown in table 1 for the applicable range of test-chamber pressures (½ to 2 atm) and relative humidities (10 to 100%). With atmospheric pressure in the test chamber the maximum error does not exceed ¼ of 1-percent relative humidity and hence, for most work, may be neglected. Even at a test-chamber pressure of 2 atm, the maximum error is less than 0.5-percent relative humidity. For very precise work, it is preferable to use the empirical equation.

TABLE 1. *Error due to nonideal behavior of water-vapor–air mixtures*

Test-chamber pressure	Relative humidity, percent					
	100	80	60	40	20	10
	Error in relative humidity, percent					
atm						
½	0	0.02	0.05	0.08	0.10	0.11
1	0	.05	.10	.15	.20	.23
2	0	.10	.20	.30	.41	.47

The pressure method was developed by Weaver and Riley (see footnote 2) for the calibration of electrically conducting hygroscopic films used in the measurement of water vapor in gases. Their equipment was designed for low rates of gas flow and was used under ambient room-temperature conditions.

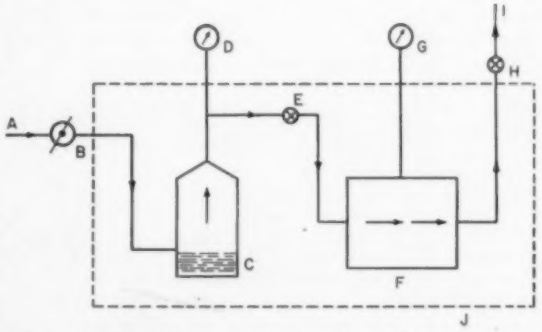

FIGURE 1. *Simplified schematic drawing of the principle of operation of the pressure-humidity apparatus.*

A, high-pressure air source; B, pressure regulator; C, saturator; D, pressure gage; E, expansion valve; F, test chamber; G, pressure gage; H, exhaust valve; I, atmosphere or vacuum source; J, constant-temperature bath.

[1] The development of this apparatus was sponsored by the Aerology Branch of the Bureau of Aeronautics.
[2] E. R. Weaver, and R. Riley, J. Research NBS **40**, 169 (1948) RP1865.
[3] E. R. Weaver, Anal. Chem. **23**, 1076 (1951).

Their saturator was a small cylinder, containing water and filled with fragments of pumice or stream-washed gravel through which the gas could be bubbled under pressure.

2. Description of Apparatus

The apparatus is shown in block diagram in figure 2 and schematically in figure 3. It consists, essentially, of the following functional components, through which air flows continuously: A high-pressure air source, a low-temperature drying system, a filtering system, a warm-up unit, a pressure regulator, a humidifying system, an expansion valve, a test chamber, and an exhaust control system.

Air is supplied from a 250-psig reciprocating compressor, *A1*, figure 3, capable of delivering 5 ft^3/min of free air at room temperature. This air is filtered (*A2*) to remove pipe scale, dirt, dust, or other solid material, and is then introduced into the drying system (fig. 4).

Water from the air at the supply pressure is removed by freezing in a train of four drying units immersed in a bath, *D*, containing a mixture of dry ice and Stoddard solvent. The first two units, *A4* and *A5*, are large-capacity centrifugal water separators. These are followed by a copper coil, *A6*, and a baffle dryer, *A7*. Particles of snow or ice and droplets of oil (from the compressor) are caught by a filter, *A8*, which is maintained immersed in the same low-temperature bath, *D*.

The air emerges from the dryer at about −78° C. It is then heated in the warm-up unit to a temperature somewhat greater than that being maintained in the thermostatted liquid bath, *B*. The warm-up unit consists of an electric heater, *A9*, that is controlled by a thermoregulator, *A10*. Two pressure regulators, *A13*, and *A14*, in series reduce the pressure and maintain it constant in the hymidifying system.

Saturation is accomplished in four stages. The air is first passed through the external gross saturator, *A15*, which is kept at a higher temperature than the bath, *B*, and then through the three bath saturators, *A18*, *A20*, and *A22*. The gross saturator, because of its higher temperature, introduces water vapor in excess of that required for complete saturation at bath temperature. The combination of heat exchangers *A17*, *A19*, and *A21* and centrifugal saturators *A18*, *A20*, and *A22* precipitates this excess water vapor so that just complete saturation is obtained in the final saturator, *A22*. The bath saturators and heat exchangers are shown in figure 5.

The saturators are simple in design and function equally well below as well as above the freezing point of water. They are similar to a type previously used [4] with considerable success. Each saturator consists of a cylinder to which water is added to a convenient depth. Air is discharged through a nozzle into the chamber above the water surface and tangential to the vertical walls and is exhausted through a central port in the top. The centrifugal force creates a whirlpool action that thoroughly mixes the water vapor with air. Spray and liquid water are forced to the walls by centrifugal force, so there is little tendency for liquid water

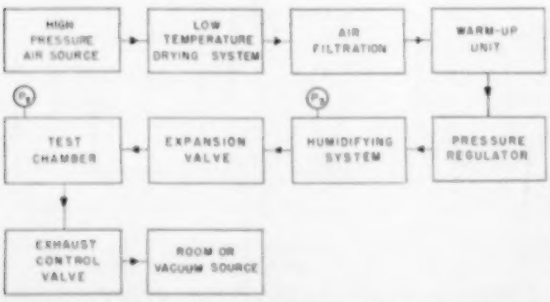

FIGURE 2. *Block diagram of the pressure-humidity apparatus.*

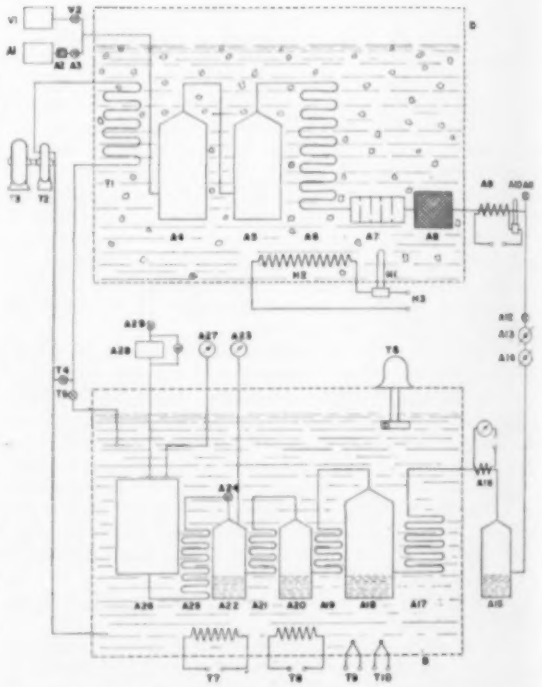

FIGURE 3. *Schematic flow diagram of the pressure-humidity apparatus.*

A1, high-pressure source; A2, filter; A3, valve; A4, centrifugal water separator; A5, centrifugal water separator; A6, copper cooling coil; A7, fin air dryer; A8, low-temperature filter; A9, electric heater; A10, bimetal thermoregulator; A11, air reversal valve; A12, shut-off valve; A13, pressure regulator; A14, pressure regulator; A15, external gross saturator; A16, resistance thermometer and indicator; A17, 19, 21, 25, copper coil heat exchangers; A18, 20, 22, centrifugal saturators; A23, 27, pressure gages; A24, expansion valve; A26, test chamber; A28, linear flowmeter; A29, exhaust control valve; B, insulated liquid (Stoddard solvent, constant-temperature bath; D, insulated dry-ice bath; H1, bimetal thermoregulator; H2, electric heater; H3, input voltage; T1, Stoddard solvent cooling coil; T2, positive rotary displacement pump; T3, motor; T4, Stoddard solvent bypass valve; T5, Stoddard solvent control valve; T6, centrifugal stirrer; T7, constant electric heater; T8, intermittent electric heater; T9, 10, thermistors; V1, vacuum source; V2, vacuum shut-off valve.

[4] Arnold Wexler, J. Research NBS 45, 357 (1950) RP2145.

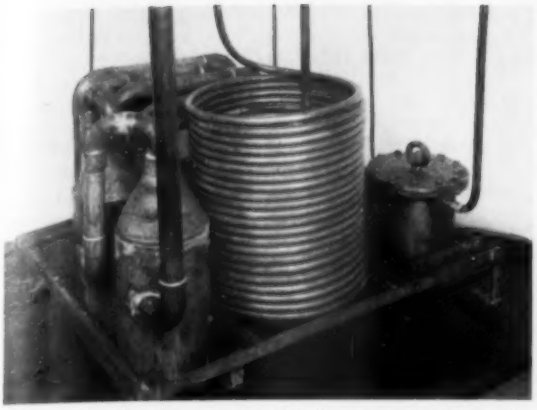

FIGURE 4. *Drying system and Stoddard solvent cooling coil.*

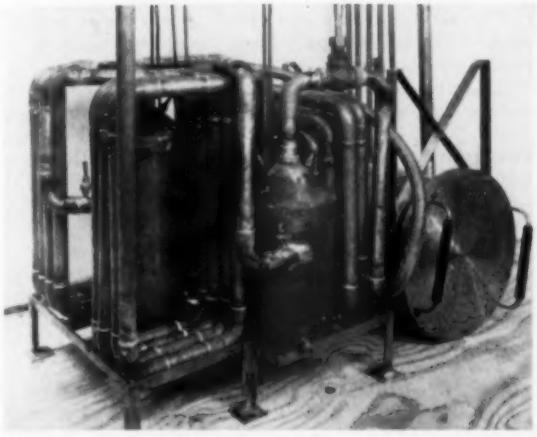

FIGURE 5. *Bath saturators, heat exchangers, and test chamber.*

FIGURE 6. *Test chamber with cover removed.*

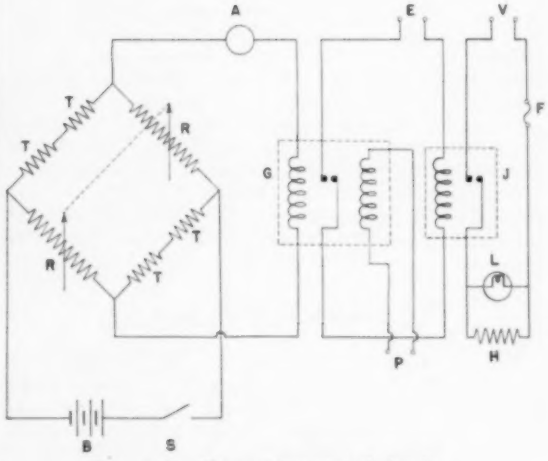

FIGURE 7. *Temperature control circuit.*

T, Thermistor; R, precision helical rheostat; B, 22½-v battery; S, battery switch; A, microammeter; G, ½ a galvanometer relay; P, input from pulsing circuit; F, fuse; J, power relay; E, input voltage for power relay coil; H, intermittent bath heater; V, input voltage for intermittent heater; L, pilot lamp.

to emerge through the exit port. A multilayer fine-wire screen baffle is used at the exit as a further guard against the escape of liquid water. As air does not bubble through the water but only passes over its exposed surface, the water may be frozen without impairing the functioning of the saturator.

Upon emerging from the final saturator, *A22*, the pressure of the air is reduced by expansion valve *A24*. Because a temperature drop may occur in the air at the expansion valve, a final heat exchanger, *A25*, is provided for bringing the air to bath temperature before it enters the test chamber, *A26*.

The working space, *A26*, is a cylindrical chamber having a nominal volume of 1 ft³. It is shown with the cover removed in figure 6. Tubular outlets extend from the chamber to allow electric leads to be brought in and out of the working space. The air discharges from the chamber into a linear flowmeter, *A28*, and then through an exhaust control valve, *A29*, into a vacuum source or simply into the room air. The chamber is suspended from a counterweight system so that it can be easily raised above or immersed into the liquid bath, *B*. A length of flexible metal hose, between the test chamber, *A26*, and the final heat exchanger, *A25*, permits the test chamber to have the required motion.

The saturation pressure, P_s, is measured in the final saturator, *A22*, by gage *A23*, and the test pressure is measured in the test chamber by gage *A27*. These measurements are made with high-precision

laboratory test gages that have been calibrated against the National Bureau of Standards pressure standards. For atmospheric or reduced pressures, a high-quality calibrated aneroid barometer is used. From atmospheric pressure up to 2 atm, a mercurial manometer is employed. The higher pressures are determined with either a 0- to 50-psig or a 0- to 200-psig Bourdon tube gage.

The temperature of the liquid bath, *B*, can be adjusted to and closely regulated at any temperature from −40° to +40° C by a simple on-off thermostatting system. Stoddard solvent, which is used as the bath liquid so that low temperatures may be attained, is actively agitated by a centrifugal stirrer, *T6*, and is circulated from the bath, *B*, by a positive rotary displacement pump, *T2*, through a copper coil, *T1*, immersed in a mixture of dry ice and Stoddard solvent in bath *D* and back into bath *B*. By proper manual setting of a bypass valve, *T4*, and a control valve, *T5*, the rate of Stoddard solvent flow is adjusted so that the bath *B* tends to cool slightly. The desired bath temperature is established by resistances (coupled helical precision rheostats), *R*, in a Wheatstone bridge circuit, figure 7. Thermistors, *T*, with temperature coefficients of 4 percent/deg C, are employed as the temperature-sensitive elements. Any cooling disturbs the bridge balance, which is sensed by a galvanometer relay, *G*. A current of ½*ma* deflects the galvanometer pointer against a magnetic contact, actuating a power relay, *P*, and, in turn, intermittent bath heater, *H*. The operation of an electromagnetic plunger returns the pointer to a sensing position. If the bridge is unbalanced, the pointer will deflect and again throw on the heater; if the bridge is in balance, the pointer will remain in a null position. An electronic pulsing circuit, *P*, periodically triggers the plunger so that the pointer may sense the bridge balance.

3. Operation of Apparatus

The method of operation of this equipment is simple. The instrument, material, or device under investigation is inserted into the test chamber, the latter closed and immersed into the liquid bath. Distilled water is added to each saturator to an appropriate depth. Solid carbon dioxide is then added to the dry-ice bath, *D*. The temperature of the liquid bath is brought to and maintained at the desired value. Air from the high-pressure source is allowed to pass through the apparatus and the pressures in the saturators and test chamber adjusted to give any preselected relative humidity. The thermoregulator controlling the temperature of the air passing through the warm-up unit is set to maintain a temperature in the external saturator several degrees higher than in the liquid bath. When thermal equilibrium had been established in the components in the liquid bath, the pressure ratio indicates the correct relative humidity in the test chamber. Changing the relative humidity primarily involves adjusting the pressure regulators so that they will maintain a new pressure in the saturators. To maintain a constant air flow, a minor adjustment of the expansion valve is also made.

When atmospheric pressure is desired in the test chamber, the air emerging from the chamber is allowed to exhaust directly into the room. Elevated pressures in the chamber are obtained by throttling the flow from the chamber by means of the exhaust control valve, *A29*, figure 3. Reduced pressures in the chamber are achieved by attaching a vacuum source to the exhaust control valve and adjusting the valve to give the required reduced pressure.

In operating below freezing, one precaution must be observed. The level of the water in each saturator must be kept below the inlet nozzle, otherwise, on freezing, the opening will be sealed by ice.

The equipment may be operated continuously for 8 to 16 hr, after which the accumulated water in the dryer should be removed. Failure to do so may result in clogging of the dryer by ice and the reduction, or even complete stoppage, of air flow.

The removal of water from the dryer is accomplished in two steps. First the dry ice bath is raised to room temperature by a thermostat, *H1*, and heater, *H2*. Then suction is applied by vacuum source *V1* and room air drawn through the reversal valve, *A11*, and dryer until all the water has been evaporated. Overnight operation usually suffices to remove most of the water.

4. Performance and Accuracy

The psychrometric and dew-point methods of humidity measurement were used independently to evaluate the accuracy of the humidity produced by the equipment. A thermocouple wet-and-dry-bulb hygrometer was employed over a wide range of relative humidities and at temperatures from 0° to 30° C. A dew-point instrument having a thermocouple embedded just below the surface of a small (¼ in. in diameter) mirror for temperature measurement, manually controlled heating and cooling of the mirror, and visual observation through a telescope for dew and frost detection, was constructed and used to measure dew points from room temperature down to −27° C. A series of experiments was made in which the relative humidity measured by the above two methods was compared with the relative humidity given by the ratio of the test-chamber pressure to the saturator pressure. The results are shown in table 2. The average difference in percentage of relative humidity between the psychrometrically determined values and the apparatus values given by the pressure ratio is ±0.4 percent, and the average difference in percentage of relative humidity between the value determined by dew-point measurement, and the apparatus value given by the pressure ratio is ±0.6 percent. Similarly, the algebraic average differences are −0.2 and 0.0 respectively. It may be assumed that as there is no marked tendency for the differences to be either positive or negative, the air passing through the saturators emerges neither supersaturated or undersaturated.

TABLE 2. *Summary of calibration*

Date of run	Nominal ambient bath temperature	Relative humidity produced by pressure-humidity apparatus	Relative humidity measured by—		Difference in relative humidity between pressure-humidity apparatus and—	
			Dew-point hygrometer	Psychrometer	Dew-point measurement	Psychrometric measurement
	°C	%	%	%	%	%
3-28-51	23.5	98.1	----	96.2	----	−0.1
		90.1	----	91.1	----	−1.0
		81.6	----	82.3	----	−0.7
		74.4	----	75.2	----	−.8
		59.6	----	59.7	----	−.1
		50.1	----	50.5	----	−.4
		38.0	----	38.4	----	−.4
		25.1	----	25.4	----	−.3
3-28-51	9.7	92.9	----	92.4	----	+.5
		79.8	----	79.8	----	.0
		61.0	----	61.0	----	.0
		49.5	----	49.3	----	+.2
		37.2	----	37.0	----	+.2
		24.6	----	24.2	----	+.4
3-28-51	30.4	92.6	----	92.9	----	−.3
		78.3	----	78.6	----	−.3
		59.6	----	59.7	----	−.1
		49.2	----	49.4	----	−.2
		37.0	----	37.2	----	−.2
		24.9	----	24.8	----	+.1
4-6-51	24.7	97.9	96.7	----------	+1.2	-----
		88.8	88.7	----------	+0.1	-----
		77.6	75.9	----------	+1.7	-----
		77.4	77.9	----------	−0.5	-----
		54.8	55.4	----------	−.6	-----
		36.9	37.3	----------	−.4	-----
		23.0	23.9	----------	−.9	-----
4-16-51	6.0	96.9	97.0	96.9	−.1	0.0
		90.6	92.1	91.4	−1.5	−.8
		77.9	78.6	78.5	−0.7	−.6
		57.7	58.5	58.2	−.8	−.5
		42.7	42.9	42.6	−.2	+.1
4-18-51	6.0	96.2	96.3	94.7	−.1	+1.5
		53.9	54.7	53.8	−.8	+0.1
		36.6	36.6	36.7	.0	−.1
		28.3	28.4	28.8	−.1	−.5
		23.2	23.1	23.5	+.1	−.3
4-19-51	−4.8	98.8	97.1	----------	−.3	-----
		86.0	86.7	----------	−.7	-----
		74.7	74.7	----------	.0	-----
4-24-51	−9.6	76.4	75.9	----------	+.5	-----
		68.3	68.2	----------	+.1	-----
		54.1	53.5	----------	+.6	-----
4-25-51	−19.8	96.3	95.6	----------	+.7	-----
		88.0	89.1	----------	−1.1	-----
		78.7	78.2	----------	+0.5	-----
		66.4	65.0	----------	+1.4	-----
		56.7	55.6	----------	+1.1	-----
				Arithmetic avg	±0.6	±0.4
				Algebraic avg	.0	−.2

The relative-humidity range obtainable is limited by the range of ratios of test-chamber pressure to saturator pressure. The maximum saturator pressure that can be employed with this apparatus is about 150 psi. When the test chamber is maintained at its maximum pressure (about 2 atm), the minimum relative humidity is about 20 percent. At atmospheric pressure, a relative humidity as low as 10 percent is readily produced, and at a reduced pressure of ½ atm, the minimum relative humidity decreases to 5 percent.

The temperature range of the equipment extends from −40° to +40° C. The upper end is limited by the flash point of the bath liquid (Stoddard solvent). However, by substituting water for Stoddard solvent as the bath liquid, the upper end of the temperature range may be extended to about 90° C.

The accuracy with which any desired relative humidity may be established is a function of the uniformity of temperature in the apparatus, particularly in the final saturator and the test chamber. The relative humidity in the test chamber will be equal to the pressure ratio of the test chamber to final saturator only if these two units are at the same temperature. The distribution of temperature within the saturators, test chamber, and surrounding liquid bath was explored by means of thermocouples, located at the inlet, outlet, and in the water of each saturator, near the front and rear of the test chamber, and at four separate points within the liquid of the bath. As an indication of the variations in temperature that may exist in the apparatus, data are presented in table 3 of the average temperatures at various locations for three 2-hour runs at different ambient temperatures. It may be seen that the differentials are of minor magnitude, especially between the final bath saturator and the test chamber.

TABLE 3. *Temperature distribution*

Location	Temperature		
Initial bath saturator:	°C	°C	°C
Air inlet	9.55	23.33	30.24
Air outlet	9.57	23.30	30.25
Water	9.66	23.29	30.30
Intermediate bath saturator:			
Air inlet	9.63	23.35	30.45
Air outlet	9.65	23.36	30.44
Water	9.63	23.29	30.39
Final bath saturator:			
Air inlet	9.64	23.39	30.48
Air outlet	9.65	23.40	30.44
Water	9.66	23.36	30.43
Test chamber:			
Front	9.64	23.35	30.40
Rear	9.61	23.35	30.37
Bath:			
Side of test chamber	9.64	23.38	30.40
Expansion valve	9.64	23.39	30.40
Rear of test chamber	9.61	23.39	30.39
Bottom	9.58	23.38	30.39

The constancy of bath temperature is of importance, for quite often materials or hygrometers under investigation are temperature dependent. The control system has effectively regulated the bath at temperatures from −40° to +40° C. For periods of time of 2 to 5 hours, average fluctuations of 0.02 to 0.05 deg. have been observed.

5. Discussion

This equipment has been used successfully for calibration testing and research. The working space of 1 ft^3 is ample for most instruments, materials, and devices that have to be completely immersed in an atmosphere of known relative humidity. There is no theoretical limitation on the size of the test chamber that may be employed with this type of

equipment; a larger sized chamber would simply require a larger surrounding liquid bath. Neither is there any limitation on the geometry of the test chamber. A cylinder was chosen in this case for ease of construction, but any other space configuration can be substituted. Even in the present design, the cylindrical test chamber can be uncoupled from the setup, and, within the limitation of the available bath space, any other size, shape, or design of chamber can be attached.

Occasionally air of known or preestablished dew point is required at a place or instrument remote from the test chamber. The desired dew point can be readily produced by the apparatus, and all or part of the air from the test chamber can be piped wherever needed. The only limiting factor involves the temperature of the ambient air, which must not drop below the dew point of the air flowing through the transmission tubing, because condensation may occur in the lines.

The range of relative humidities obtainable with this type of equipment may be extended to much lower values by using a higher pressure source. A 250-psig compressor, operating between 150 to 200 psig, is used in the present design and provides relative humidities that are sufficiently low for most purposes. Much higher pressures would necessitate components capable of withstanding those high pressures. Similarly, for flows in excess of 5 ft^3/min, a compressor having a larger volume capacity would be required.

The rapidity with which the relative humidity may be changed depends primarily on the time involved in adjusting the pressure regulator, which controls the saturation pressure. Minor adjustments of the expansion valve and the exhaust control valve may be required after the major pressure adjustment has been made. These operations can easily be executed within 30 sec. At low rates of flow, the limiting factor ceases to be the time required for performing the above mechanical operations and becomes, instead, the time involved in purging air of one relative humidity, with air of another relative humidity. The component with the maximum air volume is the test chamber. It has a space of about 1 ft^3, so that the purging time depends upon the rate of air flow through this 1-ft^3 volume.

6. Summary

An apparatus of versatility and convenience for producing atmospheres of known relative humidity has been developed and constructed at the Bureau. It operates on the "two-pressure principle," whereby air is saturated at a high pressure and expanded to a lower pressure, the relative humidity at the lower pressure being the ratio of the lower to higher pressure, provided the operation is performed at constant temperature.

Important parameters can be varied and controlled over wide ranges: relative humidity from 10 to 98 percent; temperature from −40° to +40° C; flow up to 150 liters/min; test-chamber pressure from ½ to 2 atm. The relative humidity can easily be changed from one value to another within 30 sec.

Independent checks on the accuracy of the relative-humidity production with the psychrometric and dew-point methods have yielded average agreements of ±0.4 to ±0.6 percent. As the latter methods of measurement are probably no more accurate than about ±0.5 percent, it is reasonable to assume that the apparatus produces relative humidities that are known to at least ±0.5-percent relative humidity.

Washington, December 12, 1951

Heats of Copolymerization of Butadiene and Styrene from Measurements of Heats of Combustion

Raymond A. Nelson, Ralph S. Jessup, and Donald E. Roberts

The heats of combustion of two samples of polybutadiene and four copolymers of butadiene and styrene prepared at 50° C (122° F), and one sample of polybutadiene and four copolymers polymerized at 5° C (41° F) were measured in a bomb calorimeter. The styrene contents in the copolymers varied from approximately 8 to 55 weight percent.

A value for the heat of polymerization (or copolymerization) was calculated for each sample by combining the experimental value for the heat of combustion with other known thermochemical data. The mean value obtained for the heat of polymerization ($-\Delta H_p°$) of polybutadiene is 17.4 kcal per monomer unit, and the values obtained for the heat of copolymerization varied from 17.1 to 17.7 kcal per monomer unit. No apperciable difference was found between the heats of copolymerization of the 5° C and 50° C polymers. The heat of copolymerization can be represented as a function of styrene content of the polymer by an equation of a form derived theoretically by Alfrey and Lewis, although the conditions under which the polymers were formed were such that some of the assumptions underlying the derivation of the equation were not satisfied.

1. Introduction

Measurements have been made, by means of a bomb calorimeter, of the heats of combustion of three samples of polybutadiene and eight copolymers of butadiene and styrene, ranging in styrene content from approximately 8 to 55 percent by weight (5 to 40 mole %). Two of the samples of polybutadiene and four of the copolymers were prepared by polymerization at 50° C (122° F), whereas the others were polymerized at 5° C (41° F). The data have been combined with other thermochemical data to obtain values for heats of polymerization and copolymerization.

2. Source and Purity of Material

The materials used in this investigation were made available by the Reconstruction Finance Corp., Office of Rubber Reserve, and were purified in the Rubber Section of the Bureau. Some of the properties of the purified materials are given in table 1. The polymers were prepared by emulsion polymerization. The "modifiers" used were commercial *n*-dodecyl mercaptan (DDM) for the 50° C polymers, and commercial tert-dodecyl mercaptan (Sulfole) for the 5° C polymers.

The purification procedure involved dissolving the sample in benzene and precipitating it by pouring the solution slowly into methyl alcohol while stirring. This was done three times. Then the purified sample was again dissolved in benzene, a small amount of phenyl-beta-naphthylamine was added as an antioxidant, the mixture was frozen, and the benzene was removed by sublimation in vacuum to give a product similar to foam rubber in appearance. This procedure removed soap, fatty acid, and stabilizer, as well as some of the low-molecular-weight polymer. In the present work no significant difference was found in the heats of combustion of samples burned as received after the treatment described above and after further evacuation to about 10^{-4} mm of mercury for several days at room temperature.

TABLE 1. *Analyses of polymer samples*

Polymer	Styrene	Carbon	Hydrogen	Oxygen	Sulfur	Ash	Phenyl-beta-naphthyl-amine
			50° C (122° F) polymers				
	wt %	*wt %*	*wt %*	*wt %*	*wt %*	*wt %*	*wt %* [a]
A	0	88.486	11.166	0.145	0.109	0.100	0.00
GL-657	0	88.656	11.1795	.145	[b].072	.097	.12
GL-658	8.58	88.907	10.8982	.16	.136	.104	.1
X-452	23.89	89.42	10.36	.096	.087	.13	.07
GL-662	42.98	90.100	9.7100	.14	.081	.111	.1
48-B	55.73	90.561	9.2643	.15	.046	.158	.07
			5° C (41° F) polymers				
B	0	88.474	11.1600	0.12	0.083	0.34	0.14
X-454	8.58	88.869	10.872	.235	[b].056	.18	.13
X-478	22.61	89.443	10.4008	.15	.048	.098	.11
GL-660	36.26	89.913	9.9342	.08	.030	.095	.11
GL-661	53.09	90.513	9.3585	.11	.045	.097	.11

[a] Added after analysis.

[b] The values reported here are corrected values for sulfur content. For GL-657 the experimentally determined value is 0.150% S and for X-454 0.087% S. See text p. 275.

The purified samples were analyzed quantitatively, and the results are reported in table 1. The styrene contents reported in this table were calculated from the carbon-hydrogen ratios (corrected for mercaptan).

A part of the experimentally determined sulfur content of sample X–454 was found to be present as an inorganic impurity, rather than as mercaptan attached to the polymer chain. The sulfur content reported in table 1 for this sample is the excess of the total observed sulfur over that found to be present in the inorganic impurity. The experimentally determined sulfur content of sample GL–657, which contained no styrene, was higher than that calculated from the observed carbon-hydrogen ratio on the as-

sumption that the sample consisted entirely of dodecyl mercaptan and polybutadiene. It was assumed that the difference was due to sulfur in inorganic impurity (as in the case of sample X–454), and the sulfur content reported is that calculated from the carbon-hydrogen ratio.

3. Method and Apparatus

The apparatus and procedure used in the bomb calorimetric measurements have been described previously [1, 2, 3, 12].[1] The bomb used has a capacity of 381 ml. One milliliter of water was placed in the bomb before each combustion experiment. The polymer samples used were first compressed into pellets.

The calorimetric system was calibrated with NBS Standard Sample 39g of benzoic acid, using the value 26433.8 abs j/g for the heat of combustion of this material under the conditions of the standard bomb process [3, 4, 5].

In calculating the results of the heat of combustion measurements, the amount of the combustion reaction in each experiment was determined from the mass of carbon dioxide formed, using the value 44.010 g for the molecular weight of carbon dioxide [21]. Tests were made for carbon monoxide in the gaseous products of combustion after the carbon dioxide had been removed, using a colorimetric method developed at the Bureau [6]. No carbon monoxide was found, and no soot or other evidence of incomplete combustion was found in the bomb in any experiment.

Corrections were applied to the observed heat of combustion in each experiment for heat of stirring, heat transfer between calorimeter and surroundings, ignition energy (22 j), and energy produced by the formation of aqueous nitric (58.8 kj/mole) and sulfuric (305.7 kj/mole) acids in the bomb. The last two corrections were made on the basis of the analysis of the washings from the bomb after each combustion experiment. The air initially in the bomb was not flushed out with oxygen in these experiments. The atmospheric nitrogen was left in the bomb because the oxides of nitrogen are known to catalyze the formation of sulfuric acid from sulfur dioxide, oxygen, and water.

The aqueous solution in the bomb at the end of each experiment was analyzed for the acids formed during the combustion by first determining the total acidity of the bomb washings by titration with a standard solution of sodium hydroxide, using methyl orange as the indicator, then removing the nitrate by evaporating the solution to dryness, and finally, determining the sulfur by precipitation as barium sulfate and weighing. The percentage of sulfur so determined averaged 0.01 lower than the values reported in table 1. The total correction for acids did not amount to more than 0.2 percent of the total heat produced in the combustion reaction.

The observed heat of combustion, $-\Delta U_B$, in each experiment was reduced to the value of $-\Delta U_c^\circ$, the decrease in intrinsic energy accompanying the reaction

$$C_aH_bO_cS_d(\text{solid polymer}) + \left(a + d + \frac{b-2c}{4}\right)O_2(g) \longrightarrow$$

$$a\,CO_2(g) + d\,SO_2(g) + \frac{b}{2}H_2O(\text{liq}), \qquad (1)$$

using the Washburn procedure [7] modified so as to apply to 28° C and to the energy content of the gases at zero pressure instead of 1 atm.

The measurements were made in terms of the absolute joule as the unit of energy. Conversion to the conventional thermochemical calorie was made by means of the relation

$$1\ \text{cal} = 4.1840\ \text{abs j}.$$

4. Results of the Calibration Experiments

All the measurements of heat of combustion reported in this paper were made with the same calorimetric system. However, the work was carried out over a period of about 2 years, and, because of necessary repairs to the calorimetric system, it was recalibrated several times during the course of the work. Table 2 presents a summary of the values obtained for the energy equivalent of the calorimeter and the numbers of the polymer samples whose heats of combustion were measured, using each value for the energy equivalent.

TABLE 2. *Energy equivalent of calorimeter*

Energy equivalent	Polymers investigated
j/°C	
13784.4±0.7[a]	A
13972.2±0.8	48–B, X–452, GL–658
13979.2±1.8	GL–657
13964.9±1.8	GL–662
13956.7±1.4	GL–660
	GL–661 (experiments 1 and 2)
13956.9±1.4	GL–661 (experiments 3 and 4)
	X–454
13943.4±0.5	X–478
13933.1±1.0	B

[a] The numbers following the ± signs are the standard deviations of the corresponding mean values of energy equivalent.

5. Experimental Results

The results of the heat of combustion experiments are reported in tables 3 and 4, where $-\Delta U_B$ represents the observed heat of combustion at 28° C under the conditions specified by the volume (381 ml) of the bomb, the mass (1 g) of water placed in the bomb before each experiment, the temperature (28° C) to which the combustion reaction is referred, and the data given in columns 3 and 5; and where $-\Delta U_c^\circ$ represents the decrease in intrinsic energy accompanying reaction (1) with all the reactants and products in their standard thermodynamic states at 28° C. (The data on sample A of 50° C polybutadiene are for 30° C.)

[1] Figures in brackets indicate the literature references at the end of this paper.

TABLE 3. *Results of bomb-calorimetric measurements*

50°C polymers

Experiment	Mass of sample	Mass of CO_2	Initial O_2 pressure at 28°C	Energy of combustion at 28°C.	
				$-\Delta U_B$	$-\Delta U_c^\circ$
Sample A[a]					
	g	*g*	*atm*	*j/g* CO_2	*j/g* CO_2
1	0.90914	2.94555	31.9	13878.2	13872.8
2	.92983	3.01269	31.9	13884.5	13879.2
3	.90266	2.92347	32.0	13883.4	13878.0
4	.90516	2.93225	32.2	13882.0	13876.6
Mean					13876.6
Standard deviation of the mean					±1.7
Sample GL–657					
1	0.93720	3.04067	31.8	13898.3	13892.6
2	.89631	2.81143	32.1	13890.8	13885.2
3	.89738	2.91277	32.3	13891.8	13886.1
4	.83177	2.70001	32.9	13894.7	13889.0
5		2.85568	32.8	13899.5	13893.8
6	.89462	2.90321	31.9	13892.8	13887.2
Mean					13889.0
Standard deviation of the mean					±1.4
Sample GL–658					
1	0.92538	3.01453	31.8	13747.3	13741.6
2	.89375	2.91014	32.0	13753.4	13747.7
3	.90330	2.94001	31.2	13747.1	13741.5
4	.88723	2.88905	31.3	13747.3	13741.7
5	.85106	2.77228	30.6	13747.2	13741.7
6	.88153	2.87141	31.0	13746.3	13740.7
Mean					13742.5
Standard deviation of the mean					±1.2
Sample X–452					
1	1.15567	3.78352	31.4	13498.7	13492.5
2	0.95626	3.13200	30.7	13491.9	13486.7
3	.78384	2.56602	31.5	13499.7	13494.0
4	.80454	2.63482	30.8	13498.2	13492.6
5	.89381	2.92658	31.7	13500.6	13494.8
6	.88746	2.90539	30.7	13495.3	13489.6
7	.85707	2.80670	31.6	13501.1	13495.3
Mean					13492.1
Standard deviation of the mean					±1.2
Sample GL–662					
1	0.94737	3.12010	31.6	13183.4	13177.3
2	.94541	3.12019	32.0	13180.1	13173.9
3	.90305	2.97821	31.6	13189.0	13182.8
4	.85475	2.82085	31.7	13183.8	13177.9
5	.89713	2.96068	30.7	13182.3	13176.3
6	.89258	2.94579	31.5	13188.2	13182.2
Mean					13178.4
Standard deviation of the mean					±1.4
Sample 48–B					
1	0.92042	3.05117	33.9	12963.7	12957.1
2	.91594	3.03606	30.6	12963.9	12957.8
3	.94733	3.13950	30.9	12965.5	12959.4
4	.93335	3.09382	31.4	12965.4	12959.2
5	.96567	3.20112	30.9	12970.3	12964.2
6	.94315	3.12581	30.8	12971.1	12965.0
Mean					12960.4
Standard deviation of the mean					±1.4

[a] The data on this sample are for 30° C.

TABLE 4. *Results of bomb-calorimetric measurements*

5° C polymers

Experiment	Mass of sample	Mass of CO_2	Initial O_2 pressure at 28°C	Energy of combustion at 28° C.	
				$-\Delta U_B$	$-\Delta U_c^\circ$
Sample B					
	g	*g*	*atm*	*j/g* CO_2	*j/g* CO_2
1	0.90075	2.91395	30.9	13876.6	13871.1
2	.94306	3.04831	31.6	13875.0	13869.3
3	.93426	3.02307	31.8	13875.3	13869.6
4	.91407	2.95543	31.2	13885.8	13880.2
Mean					13872.6
Standard deviation of the mean					±2.6
Sample X–454					
1	0.90962	2.95790	31.6	13670.5	13664.8
2	.91191	2.96572	32.6	13672.7	13666.9
3	.89449	2.90638	33.4	13675.1	13669.2
4	.90816	2.95355	32.1	13665.1	13659.3
Mean					13665.1
Standard deviation of the mean					±2.1
Sample X–478					
1	0.91363	2.99146	32.0	13508.7	13504.6
2	.94549	3.09588	31.6	13502.7	13498.7
3	.89638	2.93456	31.9	13498.7	13494.6
4	.92084	3.01664	31.2	13501.7	13495.9
Mean					13498.4
Standard deviation of the mean					±2.2
Sample GL–660					
1	0.91793	3.02034	31.9	13287.8	13281.8
2	.93561	3.07698	32.1	13289.6	13283.5
3	.88791	2.92170	32.0	13283.4	13277.4
4	.87460	2.87793	32.0	13284.0	13278.0
5	.93032	3.06082	31.9	13292.2	13286.1
Mean					13281.4
Standard deviation of the mean					±1.7
Sample GL–661					
1	0.93293	3.08957	32.7	13015.4	13009.1
2	.92041	3.04775	32.6	13011.2	13004.9
3	.90656	3.00149	32.6	13015.4	13009.1
4	.91953	3.04417	32.9	13023.4	13017.0
Mean					13010.0
Standard deviation of the mean					±2.6

The values obtained experimentally for the mass of carbon dioxide formed during the combustion are less than those calculated from the carbon content of the samples based on the elemental analysis, the maximum difference being about 0.2 percent. The apparatus for determining the carbon dioxide was tested several times during the course of the work, using NBS Standard Sample 39g of benzoic acid, and was found to give results that check the stoichiometric values within 0.01 percent on the average. The difference between the observed and stiochiometric values for the mass of carbon dioxide formed during the combustion of a polymer is probably due to moisture absorbed by the sample.

The results reported in tables 3 and 4 include the heat of combustion of the phenyl-beta-naphthylamine that was added to the samples as an antioxident. These results were corrected for the heat

983374—52——2

of combustion, ($-\Delta U_c^\circ$, 25° C=8305.7 kj/mole, [9]) of this material on the assumption that there was no reaction between the antioxident and the polymer or air. Table 5 presents these corrected values of $-\Delta U_c^\circ$ and also the corresponding values for $-\Delta H_c^\circ$ (25° C) and ΔH_f° (25° C) used in the calculations of heat of polymerization.

TABLE 5. *Corrected values of heat of combustion, and the corresponding values of heat of formation per gram of carbon dioxide formed in combustion*

Sample	Butadiene	Styrene	Mercaptan	$-\Delta U_c^\circ$ (28° C)	$-\Delta H_c^\circ$ (25° C)	ΔH_f° (25° C)
50° C polymers						
	Mole%	*Mole%*	*Mole%*	*j/g* CO_2	*j/g* CO_2	*j/g* CO_2
A	99.815	0	0.184	13877.9 ±3.3[a]	13901.0	73.3
GL-657	99.878	0	.122	13891.5 ±3.6	13914.6	92.0
GL-658	95.123	4.656	.241	13744.4 ±3.2	13769.9	78.8
X-452	85.840	13.994	.166	13493.2 ±3.1	13514.6	87.5
GL-662	71.742	28.085	.173	13179.7 ±3.6	13200.0	86.5
48-B	60.402	39.492	.107	12861.2 ±3.1	12880.3	79.3
5° C polymers						
B	99.859	0	0.141	13875.4 ±4.0	13898.6	74.5
X-454	95.258	4.644	.099	13667.5 ±3.8	13690.0	13.5
X-478	86.746	13.162	.091	13498.4 ±3.7	13519.8	77.8
GL-660	77.114	22.784	.103	13283.0 ±3.5	13302.5	84.6
GL-661	62.916	36.982	.102	13011.3 ±4.0	13030.4	87.1

[a] The number following each ± sign was obtained by appropriately combining the standard deviations of the mean results of calibration and combustion experiments with an estimate (0.005%) of the standard deviation of the value used for the heat of combustion of benzoic acid, and an allowance (0.02%) for systematic errors due to other factors, especially impurities in the samples.

6. Calculation of Heat of Polymerization

In the case of a polymer such as polystyrene, which consists entirely of styrene units joined together, the heat of polymerization is easily calculated as the difference between heats of combustion per monomer unit of monomer and polymer. A similar calculation could also be made of the heat of copolymerization of two monomers, provided the copolymer contained practically nothing except the two kinds of monomer units. The polymers and copolymers investigated in the present work, however, were prepared by using dodecyl mercaptan as a modifier, so that the calculation of heat of polymerization could not be made by the simple method indicated above.

The calculations made here are based on the chain-transfer theory of polymerization, from which it can be assumed that each polymer molecule contains one dodecyl mercaptan molecule chemically combined with it [10, 11]. In other words, it is assumed that the formula for a polymer molecule can be written $C_{12}H_{25}S\ (C_4H_6)_m(C_8H_8)_nH$, where m and n represent the number of butadiene and styrene units, respectively, in the molecule.[2] The values of m and n can be calculated from the elemental analysis of the sample. Then the heat of formation of this molecule can be obtained by combining the experimental value for its heat of combustion, according to eq 1 with values for the heats of formation of gaseous carbon dioxide, gaseous sulfur dioxide, and liquid water. The heat, ΔH°, of the reaction

$$C_{12}H_{25}SCH_2CH{=}CHCH_3(liq)+(m-1)CH_2{=}CHCH{=}CH_2(liq)+n\ CH_2{=}CHC_6H_5\ (liq)\rightarrow C_{12}H_{25}S(C_4H_6)_m(C_8H_8)_nH(solid\ polymer) \quad (2)$$

can then be calculated from the heats of formation of the solid polymer and of the reactants. The heat of copolymerization is taken as $(\Delta H_p^\circ=\Delta H^\circ/[(m+n)]$.

Accurate values for the heats of formation of 1,3-butadiene [13, 17] and styrene [18] are available, and are given in table 6. No data on the heat of formation of $C_{12}H_{25}SCH_2CH{=}CHCH_3$ have been found in the literature. Fortunately, only an approximate value is required for the present purpose, and such an approximate value was calculated from other data given in table 6, together with the indicated estimated values for the heats of the following reactions at 25° C:

$$nC_{16}H_{34}(liq)+S(rhombic)\rightarrow nC_{16}H_{33}SH(liq);\Delta H^\circ=5.6\ kcal \quad (3)$$

$$nC_{16}H_{33}SH(liq)\rightarrow nC_{12}H_{25}SC_4H_9(liq);\Delta H^\circ=2.4kcal \quad (4)$$

$$nC_{12}H_{25}SC_4H_9(liq)\rightarrow nC_{12}H_{25}SCH_2CH{=}CHCH_3(liq)+H_2(g);\Delta H^\circ=28.1\ kcal. \quad (5)$$

The value of ΔH° for reaction (3) was taken as equal to the difference between the heats of formation of *n*-pentane and *n*-pentanethiol; the value for reaction (4) was taken as the difference between the heats of formation of liquid ethanethiol and liquid dimethylsulphide; the value for reaction (5) was taken as the difference between the heat of formation of liquid *n*-butane and the mean of the heats of formation of *cis*- and *trans*-2-butene. The values for the heats of formation of the two butenes were obtained from the corresponding values for the ideal gases [13], together with values of heats of vaporization at 25° C to the real gases at saturation pressure [22], that is, the difference in heat content between the real and ideal gases was neglected. The value for the heat of formation of liquid $C_{12}H_{25}SCH_2CH{=}CHCH_3$ obtained in the manner indicated is −72.5 kcal/mole. As suggested previously, and as is evident from the method of calculation, this value can only be regarded as approximate.

Values of heats of polymerization and copolymerization calculated as described above are given in table 7, and are shown plotted against styrene content in figure 1, where the value $-\Delta H_p^\circ=16.68$ kcal per monomer unit for styrene [12] is also shown.

[2] Although this assumption is plausible, and is supported by experimental data [10], it is made here merely as a matter of convenience, in order to simplify the calculation of heats of polymerization. Substantially the same result would be obtained if it were assumed that some of the polymer molecules had mercaptain units at both ends and that the others had hydrogen atoms at both ends. The calculations were actually made on the assumption that a butadiene unit was attached to the mercaptan unit in each molecule. The results would not be changed appreciably by assuming that a styrene unit was attached to the mercaptan.

TABLE 6. *Values of heats of formation at 25° C used in calculating heats of polymerization*

Compound	ΔH_f°	Reference
	kcal/mole	
n-Pentane (liq)	−41.36	[14]
n-Pentanethiol (liq)	−35.8	[15]
Ethanethiol (liq)	−16	[16]
Dimethylsulfide (liq)	−13.6	[16]
n-Butane (liq)	−35.51	[13, 14]
1-Butene (liq)	−7.43	[13, 22]
1,3-Butadiene (liq)	+20.88	[13, 17]
Styrene (liq)	+24.83	[18]
n-Hexadecane (liq)	−108.59	[14]

[a] Mean of values for *cis* and *trans* isomers.

TABLE 7. *Heats of polymerization*

Sample	Styrene content	$-\Delta H_p^\circ$ (25° C)
50° C polymers		
	Mole % [a]	*kcal/monomer unit*
A	0	17.6
GL-657	0	16.9
GL-658	4.65	17.4
X-452	14.02	17.1
GL-662	28.13	17.2
48-B	39.53	17.7
Polystyrene	100	[b] 16.7
5° C polymers		
B	0	17.6
X-454	4.65	20.4
X-478	13.17	17.6
GL-660	22.84	17.3
GL-661	37.02	17.2

[a] Mole percent styrene plus mole percent butadiene = 100.
[b] Roberts, Walton, and Jessup [12]. This sample contained no sulfur, and the heat of polymerization was calculated as the difference between the heatof combustion per monomer-unit of polymer and monomer.

7. Discussion

It is apparent from figure 1 that the value 20.4 kcal per monomer unit for $-\Delta H^\circ_p$ for the 5° C polymer X–454 is entirely out of line with the values for the other polymers, which range from 16.9 to 17.7 kcal per monomer unit. No satisfactory explanation of this high value has been found, but the reasonably good consistency of the data on the other polymers suggests that the high value of $-\Delta H^\circ_p$ for sample X–454 may be related to some abnormality in the composition of this sample. Some abnormality in this sample is also indicated by a correlation of the refractive indices of the various polymers with styrene content [20]. It has been found that the styrene contents of the other 5° C polymers, as determined from analyses for carbon, hydrogen, and sulfur, can be represented by an empirical function of refractive index within a few thousandths of 1 percent of styrene. However, this relation gives a value for styrene content for sample X–454 that is lower than the value calculated from the analysis of the sample by approximately 0.5 percent.

As stated previously, a part of the sulfur in sample X–454 was present as inorganic impurity, and it may be that the inorganic sulfur compound took part in some reaction in the bomb. Since the nature of the sulfur compound is not known, no correction for the effect of such reactions could be made. Calculated values of the correction on the basis of various assumptions as to what sulfur compounds may have been present and what reactions may have taken place indicate that the error introduced by neglecting the thermal effect of the reaction, and by making corrections for nitric and sulfuric acids as described previously, probably does not exceed 0.02 or 0.03 percent of the heat of combustion. This is far too small to account for the abnormal result obtained with sample X–454.

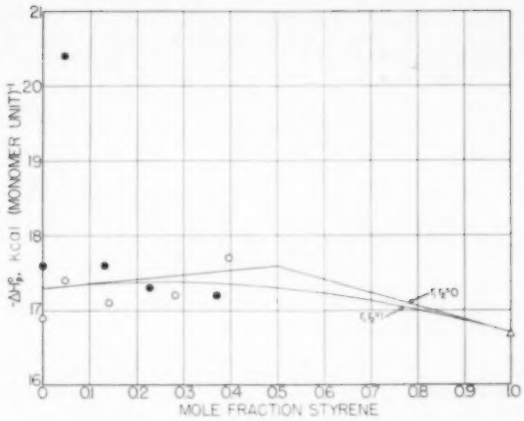

FIGURE 1. *Heats of copolymerization.*
○, 50° C polymers; ●, 5° C polymers; △, polystyrene.

It will be seen from figure 1 that the values of $-\Delta H^\circ_p$ for samples other than X–454 do not indicate any appreciable difference between the 5° C and the 50° C polymers. It will be seen also that the points for polymers other than X–454 lie reasonably near to the curves shown. The maximum deviation from either curve corresponds to about 0.06 percent in heat of combustion of the polymer. This is probably as good agreement as could be expected, considering the nature of the polymeric materials and the approximations made in calculating the heats of polymerization.

The curves shown in figure 1 were calculated from an equation of a form derived theoretically by Alfrey and Lewis [19], which expresses heat of copolymerization as a function of copolymer composition. A value for one of the two parameters in this equation was chosen empirically to fit the experimental data. According to Alfrey and Lewis [19] the other parameter, designated as r_1r_2, was less than or equal to unity in all copolymer pairs studied by them. The two curves shown in figure 1 may therefore represent the limits between which the best theoretical curve would lie. It is seen from figure 1 that the data are at least not inconsistent with the theoretical curves. It may be noted also that the deviation of the curves from a straight line connecting the values for 0 and 100 percent of

styrene is in the direction predicted by Alfrey and Lewis. It should be pointed out, however, that the polymers investigated here were prepared under conditions such that conversion ranged from 60 to 75 percent, whereas Alfrey and Lewis [19] state that their analysis applies only for low-conversion polymerization, without appreciable drift in monomer ratio.

It seems unlikely from the information available on the polymers investigated and from the results of infrared studies on similar polymers by Hart and Meyer [8] that any appreciable differences in heat of polymerization would arise from differences in the relative amounts of 1,2 and *cis*- and *trans*-1,4 structures in various polymer samples.

The authors are indebted to Max Tryon of the Rubber Section of the Bureau for purifying the various polymer samples; to Rolf A. Paulson of the Analytical Chemistry Section for the chemical analyses reported in table 1; to W. N. Hubbard and Guy Waddington, U. S. Bureau of Mines Experiment Station, Bartlesville, Okla., for permission to use their preliminary value for the heat of formation of *n*-pentamethiol.

8. References

[1] H. C. Dickinson, Bul. BS **11,** 189 (1914) S230.
[2] R. S. Jessup and C. B. Green, J. Research NBS **13,** 469 (1934) RP721.
[3] R. S. Jessup, J. Research NBS **29,** 247 (1942) RP1499.
[4] R. S. Jessup, J. Research NBS **36,** 421 (1946) RP1711.
[5] F. B. Silsbee, NBS Circular 475 (1949).
[6] M. Shepherd, Anal. Chem. **19,** 77 (1947).
[7] E. W. Washburn, BS J. Research **10,** 525, (1933) RP546.
[8] E. J. Hart and A. W. Meyer, J. Am. Chem. Soc. **71,** 1980 (1949).
[9] D. E. Roberts and R. S. Jessup, J. Research NBS **40,** 281 (1948) RP1873.
[10] H. R. Snyder, J. M. Stewart, R. E. Allen, and R. J. Dearborn, J. Am. Chem Soc. **68,** 1422 (1946).
[11] F. T. Wall, F. W. Banes, and G. D. Sands, J. Am. Chem. Soc. **68,** 1429 (1946).
[12] D. E. Roberts, W. W. Walton, and R. S. Jessup, J. Research NBS **38,** 627 (1947) RP1801.
[13] E. J. Prosen, F. W. Maron, and F. D. Rossini, J. Research, NBS **46,** 106 (1951) RP2181.
[14] E. J. Prosen and F. D. Rossini, J. Research NBS **34,** 263 (1945) RP1642.
[15] W. N. Hubbard and Guy Waddington, U. S. Bureau of Mines Experiment Station, Bartlesville, Okla., Unpublished data.
[16] Selected values of chemical thermodynamic properties, NBS Circular 500 (1952).
[17] E. J. Prosen and F. D. Rossini, J. Research NBS **34,** 59 (1945) RP1628.
[18] American Petroleum Institute Research Project 44 at the National Bureau of Standards. Selected values of properties of hydrocarbons. Table 13p, Styrenes (Feb. 28, 1949).
[19] T. Alfrey, Jr. and Charles Lewis, J. Polymer Sci. **IV,** 221 (1949).
[20] Max Tryon, Rubber Section, National Bureau of Standards, unpublished data. See also Specifications for Government Synthetic Rubber, Revised ed., issued by Reconstruction Finance Corp., Office of Rubber Reserve, 811 Vermont Ave., Washington 25, D. C., Section C 6, 1–1–51.
[21] E. Wichers, J. Am. Chem. Soc. **72,** 1431 (1950).
[22] Selected values of properties of hydrocarbons, NBS Circular 461, Table 8m, p. 139 (1947).

WASHINGTON, July 26, 1951.

Journal of Research of the National Bureau of Standards Vol. 48, No. 4, April 1952 Research Paper 2314

Infrared Spectra of Methanol, Ethanol, and *n*-Propanol

Earle K. Plyler

The infrared absorption spectra of methanol, ethanol, and *n*-propanol have been measured with prism instruments. Studies have been made of the vapors and of several dilute solutions. The methanol spectra, between 2 to 15 microns, provided a direct comparison with the other two alcohols and confirmed earlier work on the existence of a number of low-intensity bands. The two other alcohols were studied from 2 to 36 microns. The bands have been classified in relation to the O—H, C—H, C—O, and C—C vibrations within the molecules. The long-wave absorption, in the region beyond 30 microns, for each alcohol, is attributed to the hindered rotation of OH. The object of the present study was to confirm the assignments for methanol and to study and assign the vibrational spectra of ethanol and *n*-propanol.

1. Introduction

The infrared absorption spectrum of methanol in the vapor state was measured by Borden and Barker [1][1] with a grating spectrometer. The stronger bands were resolved so that the rotational structure was apparent. Their observations showed which bands were of the perpendicular and which were of the parallel type. Noether [2], using a prism instrument, also measured the spectrum of methanol and observed several weak bands in addition to those studied by Borden and Barker. Some of these weak bands have been classified as fundamentals and combinations [3]. The object of the present study was to confirm the assignments for methanol and to study and assign the vibrational spectra of ethanol and *n*-propanol. These alcohols have not been measured previously over an extended infrared region, and their spectra have not been classified.

In the present work, the spectra of ethanol and *n*-propanol have been measured from 2 to 40 μ in the vapor state and from 2 to 15 μ in solutions of CCl_4 and CS_2. Because of the similarity in structure of these alcohols, the positions of many absorption bands appear in the same regions. No attempt was made to repeat the long wavelength region in methanol, as it would not be possible to improve on the grating measurements of Borden and Barker with a prism spectrograph. However, the 2- to 15-μ region was measured as this region had not been recorded on a double-beam instrument.

2. Experimental Procedure

The methanol, ethanol, and *n*-propanol were purified under the direction of F. D. Rossini. They were found to be of high purity, which is essential in order to attribute weak bands to the spectra of the alcohols.

The absorption spectra of the vapors were determined with Perkin-Elmer infrared spectrometers, models 12A and 12C, using interchangeable prisms of lithium fluoride, sodium chloride, potassium bromide, and thallium bromide-iodide. This allowed measurements to be made from 2 to approximately 38 μ. The properties and use of prisms of thallium bromide-iodide have been described elsewhere [4]. The standard Perkin-Elmer thermocouple was used as a detector with all but the thallium bromide-iodide prism. Here a Golay detector was substituted for the thermocouple. The spectrometers were equipped with a slit-control device [5], and except for the Golay cell, the experimental arrangements were the same as those described in a previous paper [5]. Gas cells of different thicknesses with various pressures were used. The experimental arrangement did not allow the partial pressures of the vapor to be determined as all the cells could not be evacuated.

The absorption spectra of the liquids, diluted with carbon tetrachloride and carbon disulfide, were measured on a Baird recording infrared spectrometer with a sodium chloride prism. Solutions of different concentrations as well as cells of various thicknesses were used. To obtain a higher resolution from 2.6 to 3.6 μ, measurements in this region were repeated, with a lithium-fluoride prism in the Perkin-Elmer spectrometer.

3. Results and Discussion

The experimental results are given in six figures and two tables. Figure 1 presents the vapor absorption spectra between 2 and 15 μ of methanol, ethanol, and *n*-propanol. In the regions of strong water vapor absorption, bands in the alcohols could not be measured with reasonable accuracy; hence, dotted lines are used to denote the uncertainty of the absorption in these regions.

As shown in figure 1, methanol has a broad region of absorption centering near 7.43 μ. This region was restudied with the Perkin-Elmer model 21 spectrometer to take advantage of the higher resolution made possible by the improved amplifier and to eliminate the effect of the water vapor bands. The results are shown in figure 2.

Figure 3 shows the long wavelength spectra of ethanol and *n*-propanol in the vapor state. Ethanol was examined in the region from 16 to 20 μ, using an absorption cell 1 m thick, but as there was no apppreciable absorption the curve is not shown. In the region from 20 to 38 μ lithium-fluoride, calcium-fluoride, and sodium-fluoride reflectors were substituted successively for the usual aluminized mirror.

[1] Figures in brackets indicate the literature references at the end of this paper.

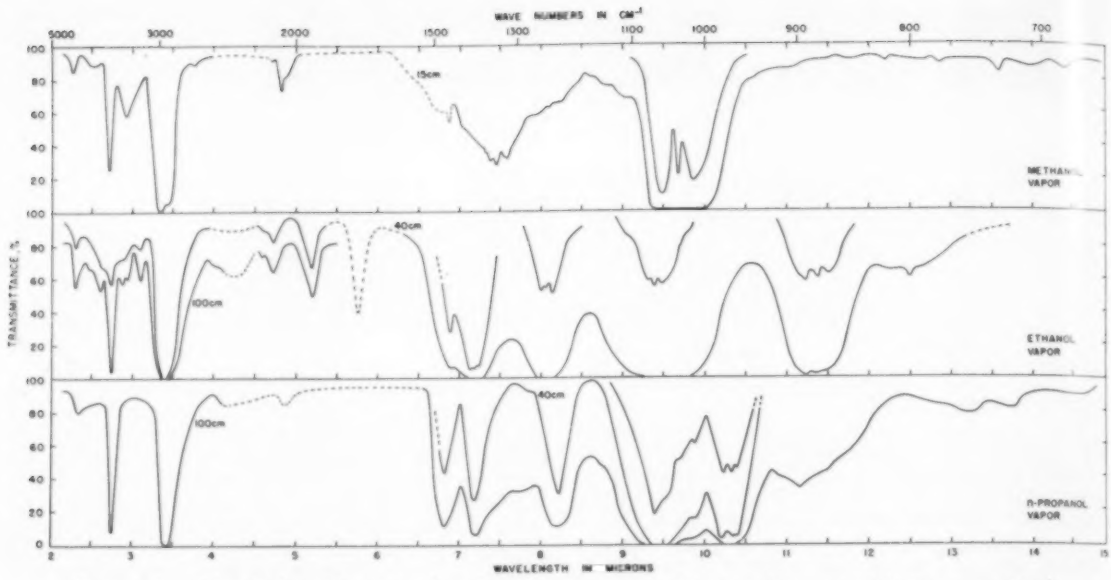

FIGURE 1. *Infrared absorption spectra from 2 to 15 μ of methanol, ethanol, and n-propanol in the vapor state.*

The pressures are saturated vapor pressures at room temperature except for the inserts, which were obtained by removing some of the vapor from the thinnest cell used for each alcohol.

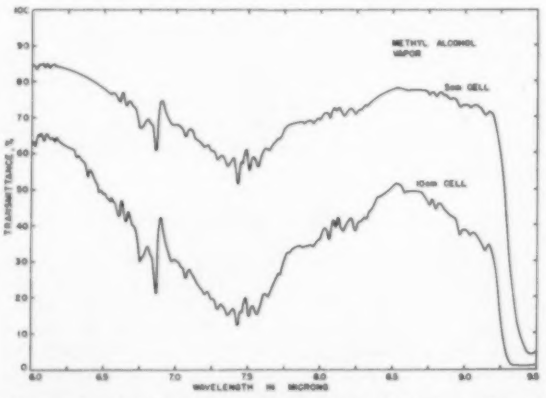

FIGURE 2. *Infrared absorption spectrum from 6 to 10 μ of methanol in the vapor state.*

The pressure is saturated vapor pressure at room temperature except for the upper curve, which is at a pressure of 6 cm of Hg.

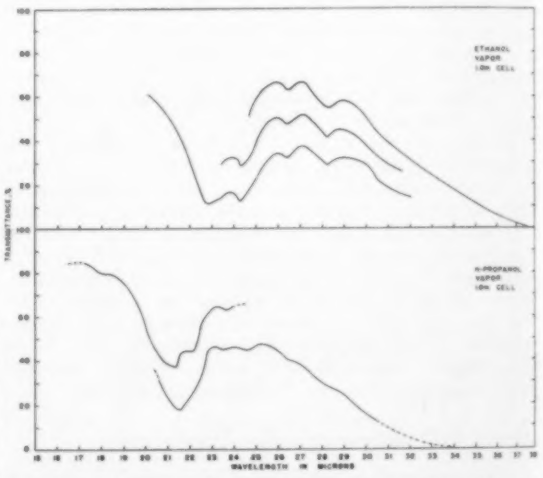

FIGURE 3. *Infrared absorption spectra from 15 to 38 μ of ethanol and n-propanol in the vapor state.*

The pressures are saturated vapor pressures for the curves of greatest absorption.

Although this resulted in some loss in the total reflected energy, the stray radiation was reduced considerably.

Table 1 lists the maxima observed in methanol, ethanol, and *n*-propanol, incorporating some of the results of the higher resolution work in the 6- to 10-μ region of methanol. The wavelength in microns, the wave number in cm^{-1}, and the observed intensity are given for each band. The intensity estimates are divided into five categories, extending from very weak to very strong. In the regions of considerable overlapping, it was not easy to determine the band centers. With the exception of the 7.43-μ region of methanol, which is more complicated and whose individual maxima may even be of a rotational nature, all the maxima of absorption are listed. As a result, some of the maxima in table 1 may be parts of bands, such a *P*, *Q*, or *R* branches, as well as separate bands. This doubt as to the nature of the maxima in table 1 includes

TABLE 1. *Observed bands of methanol, ethanol, and n-propanol in the vapor state*

Wave-length	Wave number	Intensity	Wave-length	Wave number	Intensity	Wave-length	Wave number	Intensity
				Methanol				
μ	cm^{-1}		μ	cm^{-1}		μ	cm^{-1}	
2.26	4425	W	6.61	1512	VW	8.75	1142	VW
2.49	4016	VW	6.66	1501	VW	8.80	1136	VW
2.71	3687	M	6.76	1479	M	8.97	1114	VW
2.94	3401	W	6.87	1455	M	9.04	1106	VW
3.315	3017	M	6.98	1432	VW	9.14	1094	VW
3.346	2989	M	7.07	1415	VW	9.47	1056	VW
3.360	2976	M	7.43	1346	S	9.68	1033	S
3.382	2959	M	7.96	1256	VW	10.57	946	VW
3.395	2946	S	8.07	1239	VW	12.19	820	VW
3.414	2929	M	8.17	1224	VW	12.83	779	VW
3.512	2847	S	8.24	1213	VW	13.58	736	VW
3.75	2667	VW	8.54	1171	VW	14.40	694	VW
4.86	2057	W	8.59	1164	VW			
				Ethanol				
2.30	4348	W	3.443	2904	S	7.19	1391	S
2.48	4032	VW	3.46	2890	M	8.05	1242	S
2.593	3856	W	3.98	2513	VW	9.37	1067	VS
2.71	3687	M	4.25	2353	W	11.36	877	S
2.84	3521	VW	4.63	2160	VW	12.49	801	W
2.92	3425	VW	4.74	2110	W	23.4	427	M
3.08	3248	W	5.20	1923	W	26.5	377	VW
3.340	2994	S	5.76	1736	M	28.3	353	VW
3.359	2977	S	6.87	1456	M	*37	267	S
3.42	2924	S						
				n-Propanol				
2.33	4291	W	7.18	1393	S	11.13	898	M
2.71	3687	M	7.84	1276	VW	13.20	758	W
3.358	2978	S	8.21	1218	S	13.75	727	W
3.395	2946	S	9.38	1066	VS	18.0	555	VW
3.415	2929	S	9.55	1047	M	21.6	463	M
3.458	2892	M	9.68	1033	W	23.7	422	VW
4.18	2392	VW	9.87	1013	W	24.6	407	VW
4.87	2053	VW	10.31	971	S	*35	286	S
6.83	1464	M						

* Centers of band beyond region of observations.

those in the region of 3.3 μ for all three alcohols and the 9.5-μ region for *n*-propanol.

Figures 1 and 3 show that there are regions in which the vapor-phase spectra of all three molecules are similar. In methanol, the regions of intense absorption occur near 2.7, 3.4, 7.5, and 9.6 μ. These are produced according to Herzberg [3] by the O–H and C–H stretching, C–H and O–H bending and C–O stretching vibrations, respectively. These recur in the heavier alcohols with little shift. In particular, the OH band at 2.7 μ and the band due to the C–H stretching vibrations at 3.4 μ appear at almost the same position on all three curves.

The region around 3 μ has been studied under the higher resolution provided by a LiF prism. The results are shown in figures 4 and 5. The methanol curve, figure 4, shows the symmetric vibration of the CH_3 group at 2,847 cm^{-1} (3.5 μ), the *P*, *Q*, and *R* branches being well resolved. The other bands in the region of 3.3 and 3.4 μ are considerably overlapped, and it is difficult to determine their centers. In the ethanol and *n*-propanol curves, figure 5, it is more difficult to untangle the C–H vibrations in the 3.4-μ region because there are stretching vibrations that occur in the CH_2 and CH_3 groups that give rise to five fundamentals for ethanol and seven fundamentals for *n*-propanol. Figure 4 also shows the 2.7-μ OH band resolved into *P* and *R* branches.

The 2.7-μ OH bands in ethanol and *n*-propanol were also measured. However, the resolution of the prism instrument was insufficient to separate clearly the *P* and *R* branches of the band. This problem will be pursued further with a grating spectrometer.

When the spectra of the three alcohols are studied in solutions of CCl_4 and CS_2, there are considerable changes in absorption, particularly in the two regions due to the OH band. Figure 6 shows some results from 2 to 15 μ. At the concentration of 1:20 the O—H stretching vibration is shifted to 2.9 μ, a position characteristic of associated ("hydrogen-bonded") OH. At a concentration of 1:4 in CCl_4 the unassociated OH band, which in the vapor occurs at 2.71 μ, is barely observable near 2.74 μ.

At lower concentrations, the 2.74-μ band is clearly resolved. Measurements with a LiF prism are shown in figure 7. The alcohols were diluted with carbon tetrachloride to concentrations 1:40 and 1:400 by volume, and cell thicknesses of 0.5 and 5.0 mm, respectively, were used. Thus the resultant absorption in each cell was due to practically the same relative number of alcohol molecules, and the effect of the concentration upon the position and intensity of the hydroxyl band could be examined under comparable conditions. When the dilution

was one part in forty, the OH band in the 2.74-μ region was present as well as the associated band at 2.97 μ. However, when the concentration was reduced to one part in 400, the 2.97-μ band disappeared, and the OH absorption at 2.74 μ increased in intensity. No significant changes were observed in the bands in the region of 3.4 μ. The degree of association for different concentrations appears to vary somewhat with the particular alcohol. However, this effect has not been studied in detail in the present work. Smith and Creitz [6] have studied the effect of association in 11 alcohols. They have shown that the degree of association depends on the particular alcohol and the amount of dilution. Their work also supports the idea that some of the heavier alcohols have OH bands at 2.76 and 2.86 μ.

In the region of the associated OH band (2.9 μ), there is a weak band in the vapor phase spectrum of methanol (figs. 1, 4). When this region was remeasured using a 5-cm cell with a 9.5-cm gas pressure of methanol, the cell having been filled under vacuum, the 2.9-μ band disappeared. A possible explanation for the presence of this band, attributed to association, is that a thin film of a

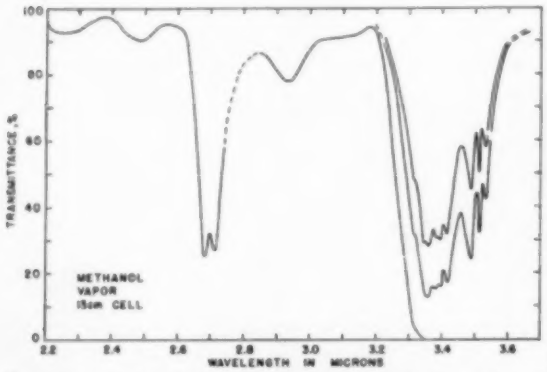

FIGURE 4. *Infrared absorption spectrum in the 3-μ region of methanol in the vapor state.*

The pressure is saturated vapor pressure except for the inserts, which were obtained by removing some of the vapor from the cell. A lithium fluoride prism was used.

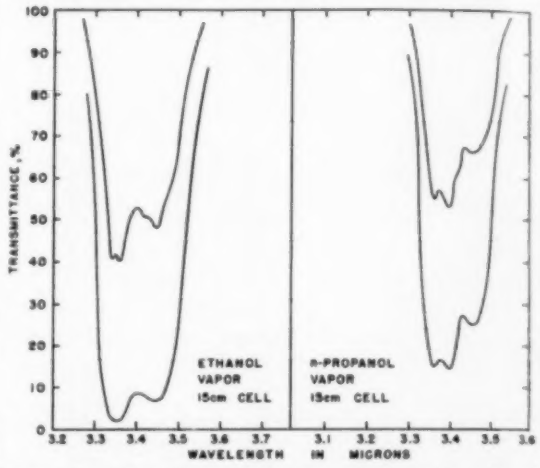

FIGURE 5. *Infrared absorption spectra in the 3.4-μ region of ethanol and n-propanol in the vapor state.*

The pressures are saturated vapor pressures except for the inserts, which were obtained by removing some of the vapor from the cell. A lithium fluoride prism was used.

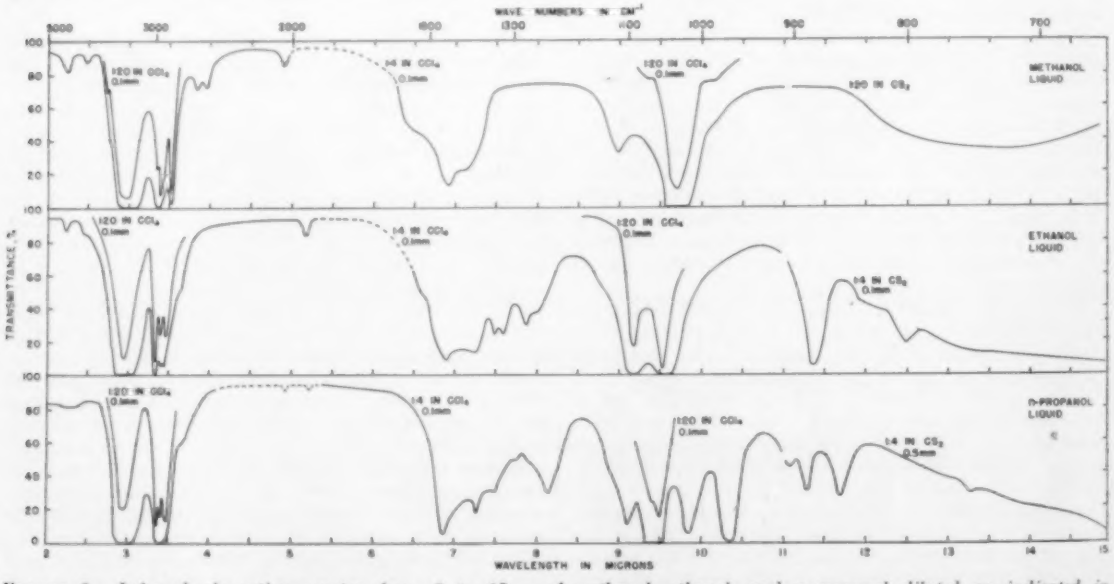

FIGURE 6. *Infrared absorption spectra from 2 to 15 μ of methanol, ethanol, and n-propanol diluted as indicated in carbon tetrachloride and carbon disulphide.*

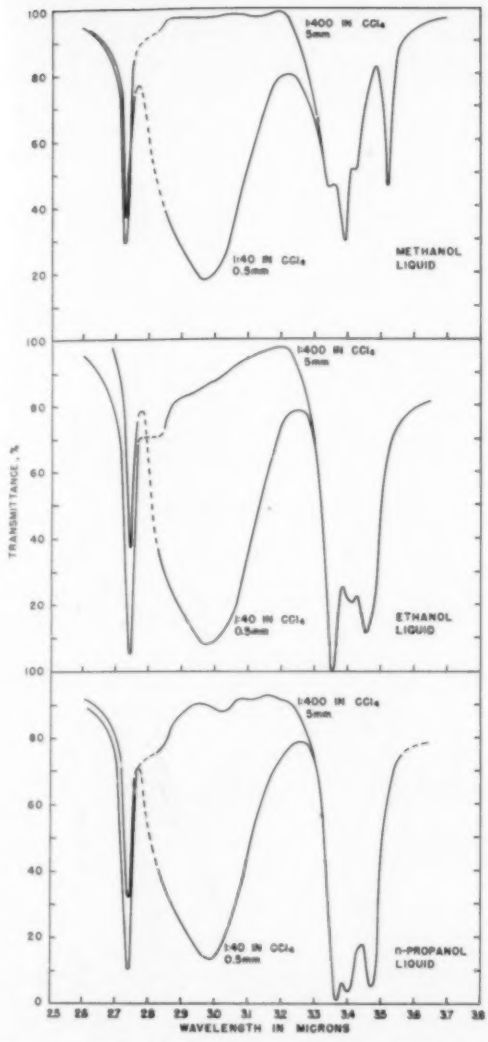

FIGURE 7. *Infrared absorption spectra in the 3-μ region of methanol, ethanol, and n-propanol diluted in carbon tetrachloride.*

A lithium fluoride prism was used.

mixture of water and alcohol was deposited on the windows of the cell, and the band is due to this thin film.

In the bands that are attributed to the C—H vibrations there are only small changes in the positions of the bands when the spectra of the vapors are compared with those of the solutions. However, in the region of O—H bendings from 6.5 to 8.5 μ there is considerable difference. In the vapor state or highly dilute solution of methanol there is appreciable absorption in the 7.43-μ region that has been assigned to the O—H bending frequency. The spectrum of a fairly concentrated solution shows no absorption in this region, but an intense band appears at 6.9 μ with a less intense band at 7.15 μ. This difference could be produced by the effect of the association of the O—H groups on the bending vibration of O—H. In solution and in the pure liquid all three alcohols have considerable absorption from 12.5 to 15 μ. None of the vapors show measurable bands in this region.

The observations of the vapor-solution shifts of the 7.4-μ band confirm in general the assignments in CH_3OH given by Herzberg [3] and listed in table 2. A further general confirmation results from a reasonable explanation of the many weak maxima between 6 to 10 μ. The twisting of the OH with respect to CH_3, (ν_8''), gives rise, in the fundamental, to a broad absorption centered around 40 μ. The first overtone of this band shows a large number of rotational lines in the region from 11.6 to 26.3 μ that have been measured by Borden and Barker [1]. They suggest that the torsional oscillations have become a rotation resulting in the spreading out of the band. Combinations of the O—H twisting with the C—O stretching (ν_4) and the CH_3 rocking vibrations (ν_7) might well give rise to the complicated structure between 6.6 and 9.2 μ. For example, if the potential energy that hinders rotation is sufficiently small, the interaction with these other modes might further reduce it and the result would be nearly free rotation. This would account for the maxima in the 6.6 to 9.2-μ region. For a more definite assignment, high-resolution studies and a detailed calculation of the oscillatory potential and its interaction with the hindered rotation is required.

Some of the fundamentals in ethanol and propanol may now be assigned by comparison with and extension of the methanol assignments. These are also given in table 2. The ethanol spectrum should have nine more fundamentals than methanol. Of these five are of interest here. Three refer to internal vibrations of the CH_2 group. The C—C—O skeletal vibrations will give rise to three bands that consist of one bending and two stretching vibrations. The band at 23.4 μ is assigned to this bending vibration, and the two bands observed at 9.4 and 11.4 μ are related to the C—O and C—C stretching vibrations. The O—H twisting vibration that also exists in methanol occurs in the region of 40 μ, but as its band falls at the limit of transmission of the thallium bromide-iodide prism, its position could not be accurately determined. The two small bands at 26.4 and 28.2 μ may be part of the first harmonic of the longer wavelength band, but only a few small structures that may be a part of this rotation were obserbed in the ethanol spectrum. The spectrum from 12 to 26 μ is considerably different from that observed for methanol, which has many rotational lines in this region.

In the 8-μ region, the ethanol bands are somewhat better defined than those for methanol. There are three fairly intense bands at 6.87, 7.19 and 8.05 μ. These are assigned respectively to the asymmetric C—H bending in CH_2 and CH_3, to the O—H bending,

TABLE 2. *Band assignments for methanol, ethanol, and and n-propanol*

Assignment	Type of vibration	Wave number	Assignment	Type of vibration	Wave number
Methanol					
		cm^{-1}			cm^{-1}
ν_1OH	Stretching	3682	ν_5-CH_3	Bending	1427
ν_3-CH_2	do	2976	ν_6OH	do	1346
ν_7''		Overlapped	ν_{11}''	Rocking	1171
$2\nu_9$''		Do.	ν_7-CH_3	do	1056
ν_2CH		2846	ν_8CO	Stretching	1033
$2\nu_4$		2057	ν_9-OH	Twisting	* 270
ν_9-CH_3		1479 1467			
$\nu_5$$CH_3$		1455			
Ethanol					
ν_1OH	Stretching	3689	ν_9-OH	Bending	1391
ν_3-CH_2, CH_3	do	2994	$\nu_6$$CH_2$	do	1242
			ν_4CO	Stretching	1067
ν_{11}''		Overlapped	ν_{10}CC'	do	877
$2\nu_{12}$''		Do.	$2\nu_{13}$CCO	Bending	801
$2\nu_8$		2110	ν_{13}CCO	do	427
$\nu_7+\nu_8$		1923	ν_{12}-OH	Twisting	* 267
$2\nu_{10}$		1736			
ν_5-CH_3, CH_3	Bending	1456			
***n*-Propanol**					
ν_1OH	Stretching	3689	ν_4CO	Stretching	1066
ν_3-CH_2, CH_3	do	2978	ν_{10}CC'	do	1013
			ν_{16}-CC	do	971
ν_{17}''		Overlapped	$2\nu_{15}$CCCO	Bending	898
$2\nu_{18}$''		Do.	ν_{15}CCCO	do	463
ν_5-CH_2, CH_3	Bending	1464	ν_{14}-OH	Twisting	* 286
ν_9OH	do	1393			
$\nu_6$$CH_2$	do	1218			

* Estimated value.

and to the bending of the CH_2 hydrogens symmetrically about the C—C axis. The same bands appear with very little shift in *n*-propanol, with the 6.83- and 8.21-μ bands showing considerable increased intensity. This is confirmation of their assignment to the CH_2 group since there is one additional such group in the heavier molecule. In both of the higher alcohols there is indubitably some overlapping of the many fundamentals in this region and therefore some uncertainty, but the principal features appear to be as assigned.

The remaining strong absorptions in *n*-propanol must be due to the skeletal vibrations. In the C—C—C—O stretching region there are three strong bands between 9 to 10.5 μ, one of which (9.38 μ) coincides closely with ethanol and is assigned to C—O. The skeletal bending vibration is observed at 21.6 μ. The long-wave absorption, as in ethanol, is assigned to OH torsion.

The author thanks Shea L. Kruegel and Mary A. Lamb for their assistance in this work.

4. References

[1] A. Borden and E. F. Barker, J. Chem. Phys. **6**, 553 (1938).
[2] H. D. Noether, J. Chem. Phys. **10**, 693 (1942).
[3] G. Herzberg, Infrared and Raman spectra of polyatomic molecules, p. 335 (D. Van Nostrand Co., Inc., New York, N. Y., 1945).
[4] E. K. Plyler, J. Opt. Soc. Am. **37**, 746 (1947).
[5] E. K. Plyler, R. Stair, and C. J. Humphreys, J. Research NBS **38**, 211 (1947) RP1769.
[6] F. A. Smith and E. C. Creitz, J. Research NBS **46**, 145 (1951) RP2187.

WASHINGTON, NOVEMBER 13, 1951.

Journal of Research of the National Bureau of Standards Vol. 48, No. 4, April 1952 Research Paper 2315

Pigmentation in Bristle and Horsehair

Sanford B. Newman

Bristles for use in brushes are normally imported in large quantities for domestic consumption. Horsehair is also commonly used in brushes, often blended with bristle in paint brushes. To determine compliance with material specifications and to enforce labeling laws it is necessary to be able to distinguish between the two fibers. The need of a reliable method for identifying the two fibers became more critical after the start of hostilities in Korea, which increased the difficulty of obtaining bristle from Chinese sources.

The use of pigment distribution in bristle and horsehair has been recommended for their differentiation. However, the use of this characteristic has been challenged on the grounds of technical difficulty in the preparation of microscopic specimens and the possibility of variations in pigmentation at different levels in the fiber, in animals from different geographical locations, and in different types of hairs from the same animal.

As little previous attention has been given these points, a series of observations was made that show clearly that pigment distribution in fiber cross sections permits the detection of horsehair in bristle and bristle products. The test is, of course, applicable only to fibers that contain sufficient natural pigment to establish a distribution pattern. In addition, the medullation in the two fibers is sufficiently distinctive to constitute another aid in identification.

1. Introduction

The term "bristle" as used in the brush industry refers to the hair of swine exclusively [1].[1] References to the use of bristles in brushes can be found in the literature as early as the fifteenth century [2], and even today synthetics like nylon and neoceta have only begun to be substituted for bristle in paint and varnish brushes. Despite the large amounts of bristle consumed annually in this country, the greater part is still received from foreign sources, over 7,000,000 lbs. having been imported in 1950 [3]. Swine cannot be maintained profitably in the United States for the length of time necessary to develop long flexible bristles. A plentiful supply of cheap labor would also be required for the initial cleaning, sorting, and packaging if the domestic product were to compete with foreign bristle.

Because of this reliance on foreign supplies, the bristle trade has been subject to the exigencies of twentieth-century history. Before 1918 the Siberian and Russian bristles dominated the trade, but subsequently the Chinese product gained preference, especially in the premium types. The change was due, at least partially, to deterioration in the quality of preparation and dressing of the fiber for market. When the United Nations police action was instituted in Korea in 1950, Chinese bristle was abundant at reasonable prices, but soon after supplies dwindled and prices rose.

The failing supply of bristle was soon reflected in the number of adulterated brushes submitted for test to the Bureau. Brushes containing mixtures of bristle and horsehair, properly marked as to fiber content, are standard items usually available at lower prices than comparable brushes of pure bristle. More and more often it was found that brushes labeled pure bristle contained considerable quantities of horsehair. That this was a phenomenon of widespread occurrence was evidenced by the number of queries on testing procedure that reached the Bureau from other Government agencies, from private testing laboratories, local purchasing organizations, and from individuals.

At the National Bureau of Standards, pigmentation pattern in the cross section of fibers is the chief criterion used in differentiating bristle from horsehair. This test is based on the original observations attributed to E. Weirick by Von Bergen and Krauss [4]. According to Krauss [5], Weirick observed the pigment distribution in fibers treated with a 10-percent sodium hydroxide solution. However, a number of questions were raised concerning the validity of the test by people in the brush and bristle trade and their consulting technical experts. These questions involved sectioning techniques and the possibility of variations in pigmentation at different levels in the fiber, in animals from different geographical locations, and in different types of hair from the same animal. For this reason the Bureau undertook to study these questions to determine the validity of the test method.

2. Materials and Methods

An attempt was made to secure samples of bristle and horsehair from as many representative sources as possible. Commercial bristle and horsehair were obtained from brush manufacturers and bristle suppliers. Other specimens from the files of the microbiological laboratory of the Bureau, mainly obtained from the larger manufacturers of brushes, were included in the study. In addition, a small amount of fiber was secured from animals in the surrounding area. Through the courtesy of the National Museum's Division of Mammals bristle and hair from hides of specimens of the families Suidae, Tayassuidae, and Equidae were made available. Tables 1, 2, and 3, list the horsehair, bristle, and miscellaneous hair samples used in this work.

The Hardy microtome (fig. 1), a device used routinely in textile microscopy, was the means for

[1] Figures in brackets indicate the literature references at the end of this paper.

TABLE 1. *Bristle examined in cross section*

Sample	Source
Black Hankow	Commercial A.
Black Hankow (received 1936)	Commercial B.
Calcutta India	Commercial C.
Equador-South American	Do.
Bristle	Commercial D.
Black Bristle	9-month-old pig, Great Black strain, U. S. Dept. of Agriculture, Beltsville, Md.
Black Shanghai	Commercial A.
Superior Hankow, 5 in. (received 1936).	Commercial E.
Shanghai Black	Commercial A.
Black Bristle	Commercial D.
Mixed Bristle	Brush, commercial D.
Black Shanghai	Commercial A.
Persian	Commercial D.
Sus scrofa attila (Persian wild hog)	Smithsonian Institution Collection U. S. National Museum Specimen 283111.
Sus scrofa moupinensis (Chinese wild hog).	Smithsonian Institution collection U. S. National Museum specimen 172658.
Sus cristatus rhionis (Crested hog)	Smithsonian Institution collection U. S. National Museum specimen 122925.
Sus barbatus (Bearded hog)	Smithsonian Institution collection U. S. National Museum specimen 199838.

TABLE 2. *Horsehair (equus caballus) examined in cross section*

Sample	Source
Horsehair	Commercial 1.
Horsehair (flagged)	Do.
No. 1 stiff quality	NBS collection.
Regular medium quality, black	Do.
Black mixture	Do.
Superior extra-stiff quality, black	Do.
No. 2 stiff quality, black	Do.
Black Australian	Commercial 2.
Horsehair (tail)	12-yr-old mare, USDA, Beltsville, Md.
Horsehair	NBS collection.

TABLE 3. *Miscellaneous hair examined in cross section*

Sample	Source
Hylochoerus meinertzhageni (Suidæ).	Smithsonian Institution collection U. S. National Museum specimen 164627.
Pecari angulatus crassiger (Tayassuidæ).	Smithsonian Institution collection U. S. National Museum specimen 11710.
Equus grevyi (Equidæ)	Smithsonian Institution collection U. S. National Museum specimen 163238.
Equus hemionus (Equidæ)	Smithsonian Institution collection U. S. National Museum specimen 84083.
Equus przewalskii (Equidæ)	Smithsonian Institution collection U. S. National Museum specimen 260018.

sectioning all the samples, which contained 300 or more fibers. Because of the toughness of both bristle and horsehair it was necessary to soften the samples before they were cut. Although several organic plasticizers were tried, both hot and cold, none of them was as effective as a 10- or 15-min immersion in boiling water. After boiling the fibers they were placed in a microtome and sectioned in the usual fashion. The screw was advanced a 25 μ increment for each section, but because the cut is made by hand the actual section thickness would be expected to vary to some extent from this figure. Sections were mounted on slides in Canada balsam.

Single bristles or hairs were oriented in gelatin capsules, as shown in figure 2. The top and bottom of a No. 00 capsule was perforated with a hot needle and the fiber to be sectioned threaded through the two holes. A plug of gelatin or sodium carboxymethylcellulose was formed around the fiber where it passed through the bottom of the capsule in order to prevent leakage of the embedding material. If possible, the fiber was of such length that the cap could be withdrawn from the body of the capsule without unthreading the fiber from the cap.

The body of the capsule was filled with a mixture of monomers (8 parts of *n*-butyl methacrylate and 2 parts of methyl methacrylate) plus 0.5 percent of a catalyst, 2,4-dichlorobenzoyl peroxide. Polymerization was accomplished in an air-circulating oven held at 50° C.

When polymerization was complete the gelatin containers were removed by soaking them in warm water. Mounting of the embedded fiber in the microtome was essentially by the method recommended for the ultramicrotomy of fibers [6], as shown in figure 3. Sections were cut at 10 or 15 μ in the Spencer microtome. The methacrylate matrix was removed with toluol and the sections mounted in Canada balsam.

3. Observations

Typical cross sections of hog bristles (*Sus scrofa*) from various sources are shown in figure 4. Bristle pigment appears concentrated or more dense in the center of the cross section and becomes more dilute as the periphery is approached. Certain fibers in any sample of bristle exhibit cross sections with more or less jagged fractures, usually through the center of the section. It is a common observation that many bristles have hollow centers, and these hollows or fragmentation medulla probably account for most of the gaps noted in the cross sections. Occasionally these openings will practically divide the sections into two halves, and in these cases it is suspected that the sectioning procedure is responsible for, at least, enlarging these fragmentation medullas. In general, the bristle medulla is totally devoid of fibrous material but, more rarely, fragments of the surrounding cortical cells can be found in the opening. Where fragmentation medullas are present, the pigment will appear more concentrated around the edges of the void and will diminish toward the peripheral cuticle.

Central concentration of pigment was found in all bristles, regardless of their geographical origin. Rarely, a radiate variation of the pigmentation pattern can be found. In this, the pigment is limited to bands that in general are thick at the center and narrow toward the border of the section, as shown in figure 5.

The genus *Sus* consists of numerous closely allied and slightly differentiated forms. Transportation by man has further confused the taxonomy. However, it appears that there are at least three groups of wild hogs of more than subspecific rank [7]. Several dozen bristles, representing all these groups, as well as widely separated geographic races of one

of them, were taken from hides in the Smithsonian Institution and were sectioned and examined (see table 1). The pigmentation pattern was found to be the same in all specimens, as noted in commercial bristle from domestic hogs.

Hylochoerus meinertzhageni (African Forest hog) a member of the Suidae, or Pig family, exhibits the normal bristle pigmentation pattern (fig. 6). Cross sections of the hair of the peccary (*Pecari angulatus crusniger*) were examined and found to have a much different and distinctive pattern (fig. 7). The medulla is much more diffuse, and the medullary cell outlines are easily distinguished. *Pecari a. crusniger* is included in the Tayassuidae, a family closely related to the Suidae.

Pigmentation at various levels in a bristle appeared to be subject to some variation in density, but the basic pattern did not change. Sections through the part of the bristle enclosed in the root sheath (fig. 8) showed the same pattern found at other levels in the fiber. When sections were taken through the branching flagged portions of the bristles the pigmentation pattern was more difficult to detect. Cross sections of flags appeared as fragments or segments of the entire bristle section. The opacity of sections through the flagged area is often comparatively high.

Hog wool is the curly, rather fine fiber usually found growing on the belly area of the hide. Hog hair is the name applied to the poorly defined fiber that is intermediate between bristle and wool. Wool is rarely found in brushes, being a waste product destined mainly for upholstery use, but hair is largely blended with the brush bristle. When examined in cross section, however, both wool and hair were found to have the pigmentation found in bristle, as shown in figures 9 and 10.

Mane hair and tail hair of the domestic horse (*Equus caballus*) are widely used in many brushes. The body hair is generally too short for this type of application. Tail hair is thicker in cross section than mane hair, and the Federal Specification [8] arbitrarily defines any sample having an average diameter of not less than 0.0055 in. as tail hair. In cross sections, however, both tail and mane hair revealed the same pigmentation pattern. It differed from bristle in possesing a cellular medulla, with little or no pigment, which occupied the center portion of the hair cross section. The pigment granules were in a ring around this colorless area. The medulla was only roughly circular; fingerlike diffuse projections of pigmented cells into the colorless areas were common, and colorless projections into pigmented areas were often seen. Typical cross sections through samples of horsehair are shown in figure 11.

As in bristle, the sections of horsehair revealed minor variations in density and distribution of pigment granules at different levels, but the basic pattern was constant. In figures 12, 13, and 14 are views of sections cut from different locations on the same hair.

Other members of the horse genus appeared to have essentially the same pigment distribution. Hairs from Grevy's zebra (*Equus grevyi*), the Asiatic wild horse (*E. przewalskii*), and Asiatic wild ass (*E. hemionus*) all show peripheral concentration of pigment granules in cross section (figs. 15, 16, 17).

Pigment was not seen in sections of the cuticle, or scale, structure in either bristle or horse hair. The cuticle of bristle appeared much thicker than that of horsehair and formed a refractive ring around the entire section. The pigmentation did not come quite to the outer edge of the cortex in all fibers, and in cross section such fibers had the superficial appearance of possessing an extremely thick cuticle. However, the true cuticle could be easily distinguished by the difference in its index of refraction.

The dyeing of light-colored, or unpigmented, bristle and horsehair is a common practice in the manufacture of brushes. The presence of dye in the fibers could be easily detected in cross section and presented no obstacle to the determination of pigmentation pattern. Natural pigment was always present in the form of discrete melanin granules. Dye, on the other hand, could always be seen in cross section as a band of amorphous color of varying width. In many cases the band appeared to be localized and discrete, forming a ring concentric with the section outline. In other cases, however, there would be almost complete penetration of dye throughout the section. Sections of dyed horsehair are shown in figure 18.

The artificial flagging of horsehair appears to be a fairly common practice in the brush industry. Flagged horsehair is sometimes found in brushes labeled bristle and, more often, in brushes containing mixtures of horsehair and bristle. Synthetic flags, as would be expected, were found on fibers with little or no taper. All the branches of the flag at the tip of the hair appear to spring from practically one point on the length of the fiber and many branches, often a dozen or more, were found in a flag. At the point where the fiber is broken up into these branches the hair appears to increase in diameter. Natural flags contained fewer branches, and these divided at different levels from the main trunk. Examples of these flags are shown in figure 19.

The outline of the cross sections of both bristle and horsehair ranged from roughly circular to elliptical and included many irregular shapes.

4. Discussion

Microscopic examination of fiber is apparently rarely resorted to in the brush and bristle trade. Great reliance is placed on the so-called "eye and feel test", which some use not only to identify bristle but also to determine its geographic origin. Other individuals using this test are more moderate in their claims. Visual examination and manipulation of the fibers is the basis of this test method.

Several men with 20 or more years of experience in the brush and bristle trade consented to apply the eye and feel test to a brush shown to be adulterated by cross-sectional examination (fig. 20). Many of the samples extracted from the brush, which were

identified by the experts as representing fibers from a specific geographic source, were extremely small, but in almost all cases sectioning revealed the horsehair pigmentation pattern in some of the fibers chosen. In one case two fibers were selected to represent Tientsin bristle, and one of the fibers showed the horsehair pattern. It is difficult to define the criteria used in such a nonmicroscopic test. Flexibility and surface appearance are often mentioned, but it is interesting to note that most errors in judgment are made on the finer and untapered fibers that are in the problem group. Evidently taper, fiber diameter, and probably flagging must be elements in the precision of this test.

The microscopic observations previously described indicate that the centric pigmentation pattern is characteristic of bristle, whereas the concentric pattern is characteristic of horsehair. Centric pigmentation appears not to be restricted to the domestic *Sus scrofa* but is probably common to all of the Suidae. Similarly, the concentric pattern of pigmentation was found in the hair of all members of the genus *Equus* that were studied. In view of this taxonomic distribution, it is hardly conceivable that geographic origin would affect the pattern.

Von Bergen and Krauss [4] found that all bristle fibers have a medullary channel. Although medullated fibers were not uncommon in the samples examined, they were not as numerous as the nonmedullated, and most of the medullas were of the fragmentation type. In unpigmented, or colorless, bristle, however, medullation appears more common.

The sectioning of bristle and horsehair presents no great problems in technique. In sectioning with the Hardy microtome, a fresh single-edge razor blade is used for cutting each section. Drying out of the wet fibers causes a gradual return to their normal toughness, so that sectioning should be performed as expediently as possible. With methacrylic embedding and the Spencer microtome, 6 to 12 fibers can be cut at 10 μ or less if desired.

Bristle and horsehair are too opaque to permit microscopic examination without sectioning. Weirick's method of treating fibers with a 10-percent solution of sodium hydroxide enabled her to detect the pigmentation pattern through the fiber diameter. Treatment with alkali, however, leads to the degradation of the fiber and does not permit critical observation of detail. Moreover, it gives no information on the presence or absence of dye.

Hardy and Hardy [9] have tabulated some trade categories of commercial paint-brush fibers, giving their most notable characteristics. A typical bristle has a definite taper, being thicker at the butt, or root, end and becoming gradually thinner toward the tip. Near the tip end the bristle becomes furcated, often dividing into several branches, to form the flag. Bristles that approximate this description are easily distinguished from horsehair by their gross aspect. Horsehair has no definite taper, though it may vary in diameter over its length, and it has no natural flag. The average diameter of bristle at the base is greater than the average diameter of horsehair [3].

In all groups of bristles, selected at random, however, there are fibers showing little or no taper, a complete lack of flag, or both. Flags may fail to form, be worn off while still on the animal, or be removed in processing. It is these bristles, often making up a considerable part of the whole, which present a problem in fiber identification. These can be definitely identified by their pigment distribution. As picnometer measurements indicate that the density of both horsehair and bristle is approximately 1.29 [10], quantitative data on the amount of each fiber in a mixture can be obtained by merely integrating the cross-sectional areas in photomicrograph.

Cross-sectional examination is, unfortunately, not applicable to white or very slightly pigmented fibers. Where only small amounts of pigment are present it is usually desirable to increase the section thickness to resolve the pigmentation pattern. The amount of light bristle or hair used in brushes, however, is not large. These observations indicate that where applicable the microscopic examination of cross sections is an accurate and rapid means of differentiating bristle and horsehair. Moreover, the techniques involved present no unusual difficulty, and the pigment distribution is a characteristic at the family level and not subject to significant change because of geographic location, type of hair, or location in the hair itself.

The author expresses his appreciation to Charles S. Cox of the Federal Trade Commission, John I. Hardy of the United States Department of Agriculture, and C. O. Handley, Jr. of the Smithsonian Institution for cooperation in the course of this work.

5. References

[1] Federal Trade Commission. Trade practice rules for the paint and varnish brush manufacturing industry (promulgated Jan. 14, 1939).
[2] M. Denison, Bristles and brushes (Dodd Mead and Co., New York, N. Y., 1949).
[3] Bureau of the Census, United States Imports of Merchandise for Consumption. Report No. FT 110 (1950).
[4] W. Von Bergen and W. Krauss, Textile fiber atlas (American Wool Handbook Co., New York, N. Y., 1942).
[5] W. Krauss, personal communication (1951).
[6] S. B. Newman, New technique for cutting very thin sections and its application to the electron microscopy of fibers, ASTM Bul. No. 163: 57–60 (1950).
[7] G. H. H. Tate, Mammals of eastern Asia, p. 310 to 315 (MacMillan Book Co., Inc., New York, N. Y., 1947).
[8] Federal Standard Stock Catalogue Section IV (Part 5), Federal Specification for Hair; Horse, Curled, C–H–111 (1935).
[9] T. M. P. Hardy and J. I. Hardy, Animal fibers used in brushes, U. S. Dept. Agr. Circular 802 (1949).
[10] Unpublished data.

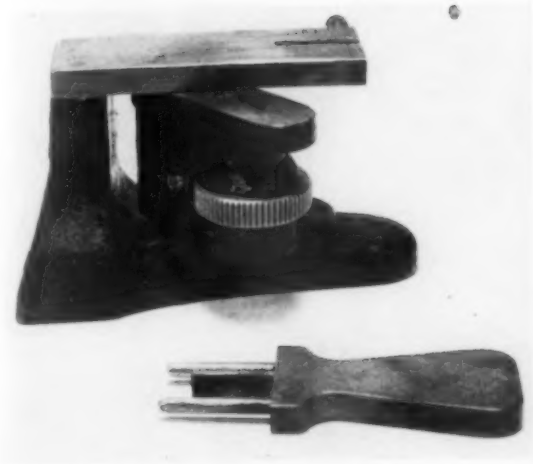

FIGURE 1. *Disassembled Hardy microtome.*

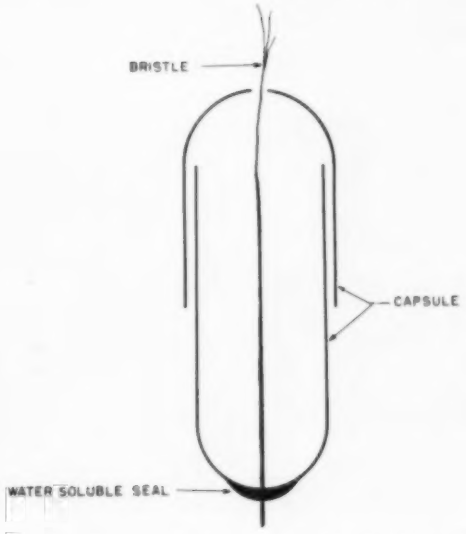

FIGURE 2. *Schematic section of capsule embedding cell for single bristles.*

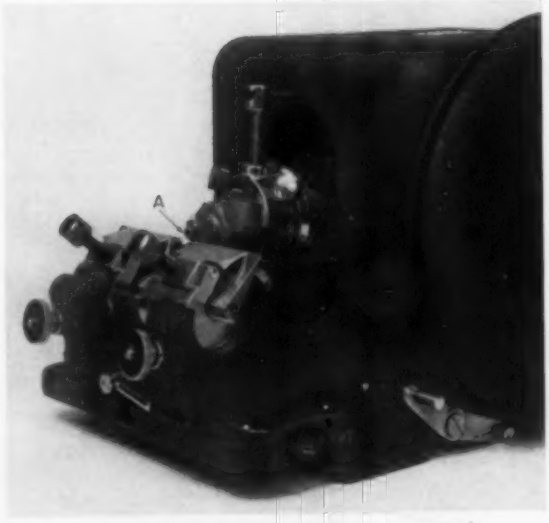

FIGURE 3. *Sectioning single fibers.*

A, Single bristle being sectioned in a rotary microtome.

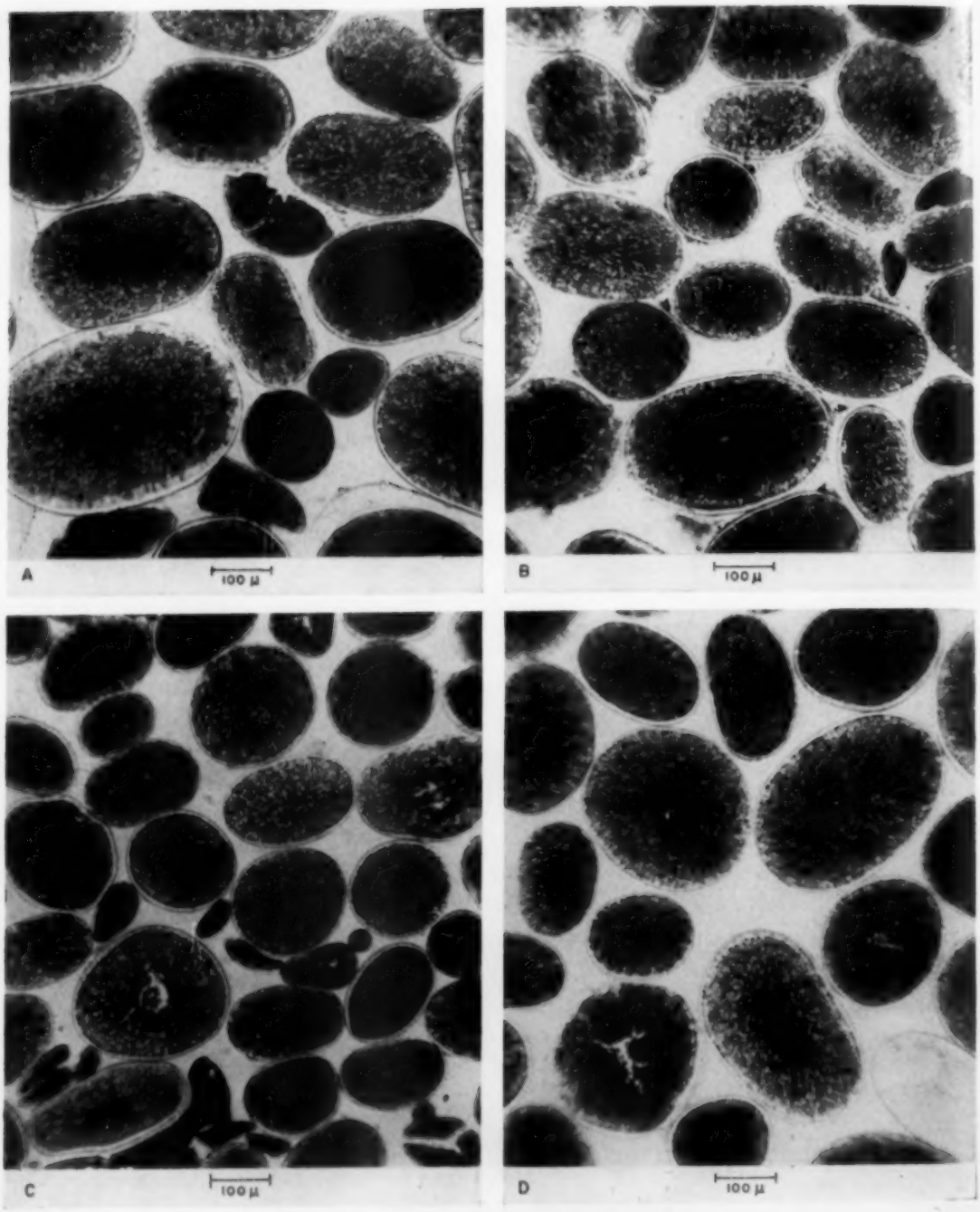

FIGURE 4. *Cross sections of bristle from various sources.*

A, Black Hankow received in 1936 from commercial source B; B, Black Hankow received in 1950 from commercial source A; C, random sample taken from a bristle brush; D, Ecuador, South America.

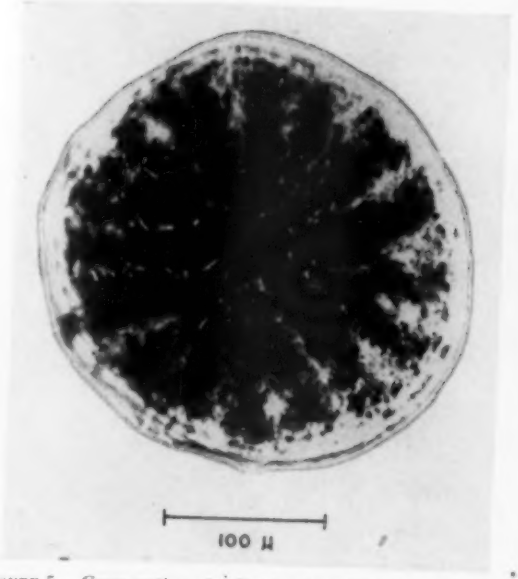

FIGURE 5. *Cross section of a Persian bristle showing radiating bands of pigment.*

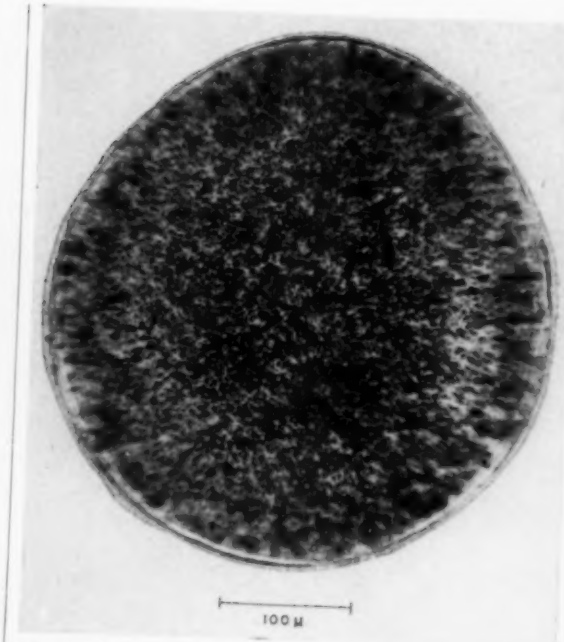

FIGURE 6. *Cross section of a hair from Hylochoerus meinertzhageni (Suidae) showing hog-type distribution of pigment.*
From U. S. National Museum specimen 164627.

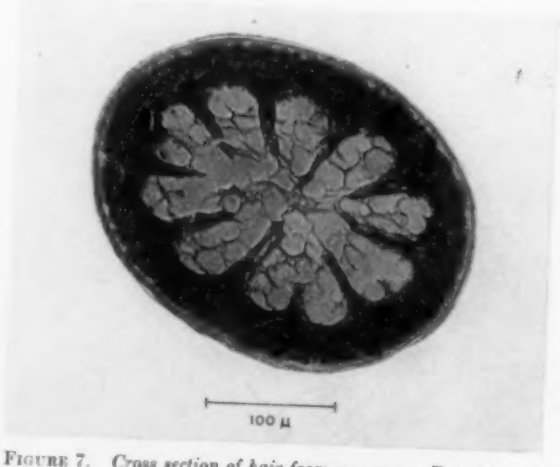

FIGURE 7. *Cross section of hair from a peccary, Pecari angulatus crusniger.*
From U. S National Museum specimen 11710.

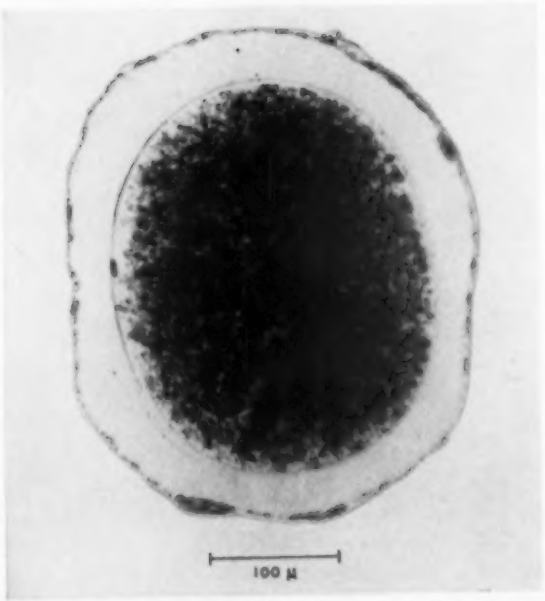

FIGURE 8. *Section through the butt end of a black Hankow bristle showing the root sheath.*

FIGURE 9. *Cross section of bristle wool.*

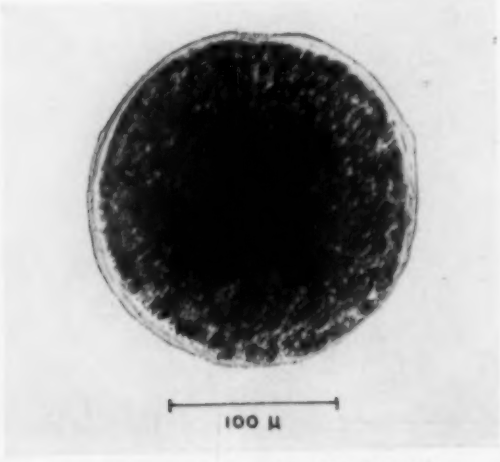

FIGURE 10. *Cross section of bristle hair.*

UNIVERSITY OF MICHIGAN LIBRARIES

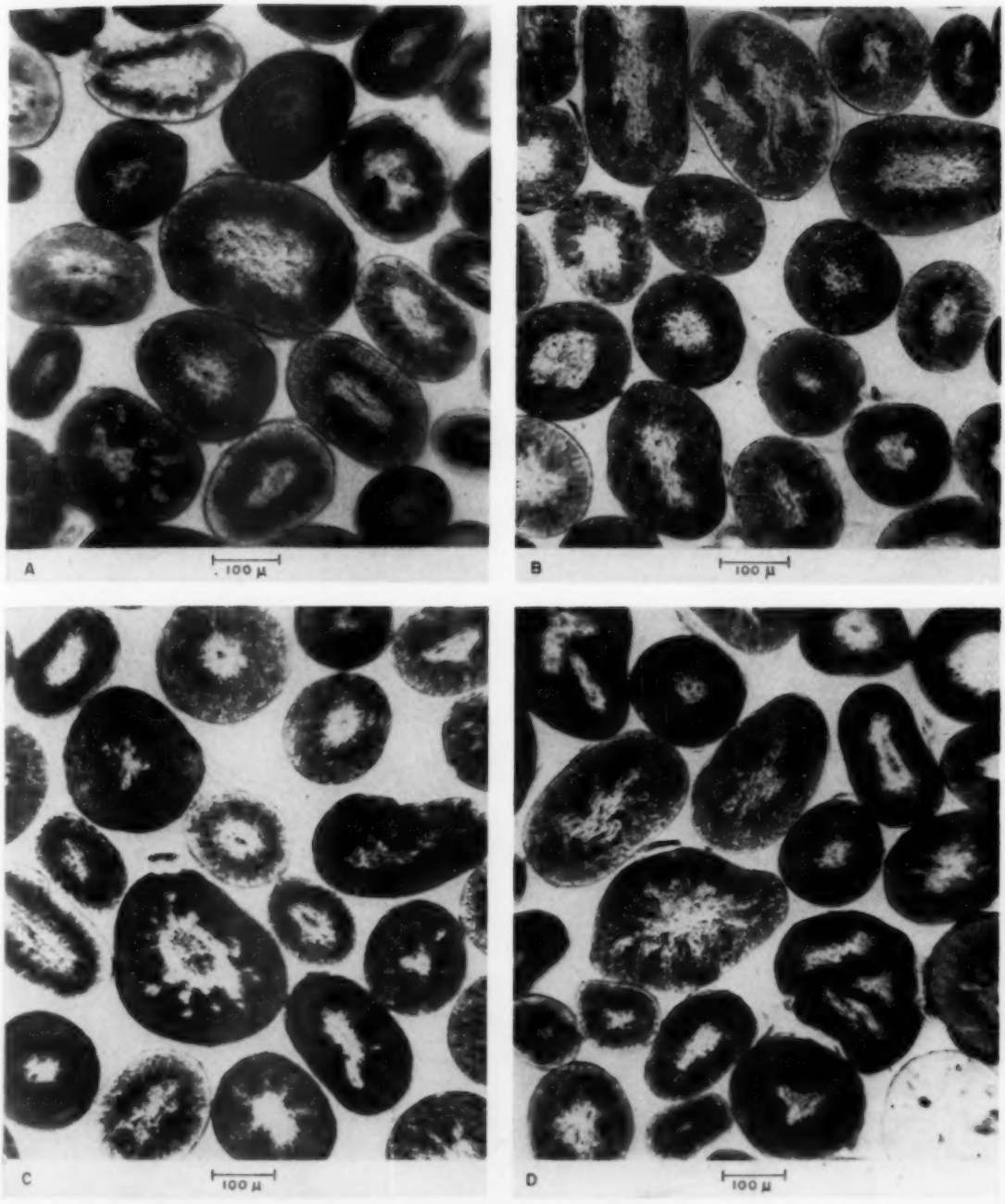

FIGURE 11. *Cross sections of commercial horsehair.*

A, Black Australian; B, regular medium quality black horsehair; C, No. 1 stiff quality black horsehair; D, No. 2 stiff quality black horsehair.

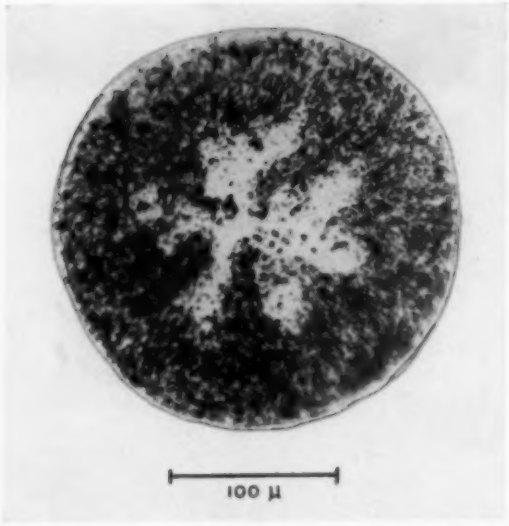

FIGURE 12. *Cross section of a horse tail hair (Equus caballus) near the root end.*

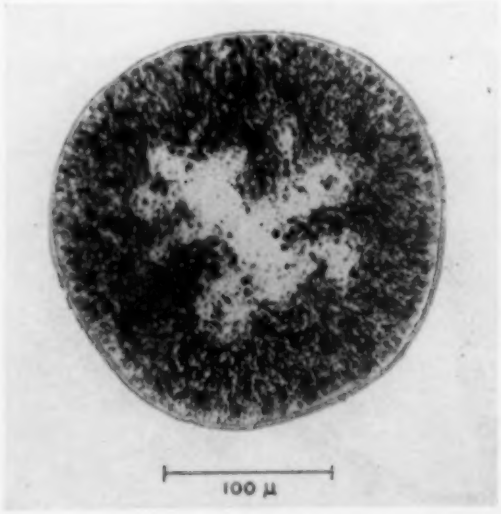

FIGURE 14. *Cross section of the same hair as in figure 12 but from the distal end.*

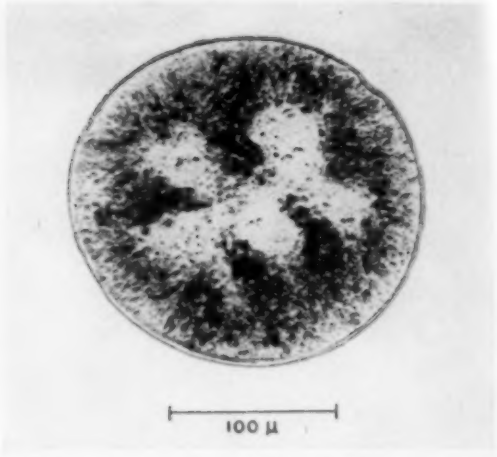

FIGURE 13. *Cross section of the same hair as in figure 12 but from the middle of the length.*

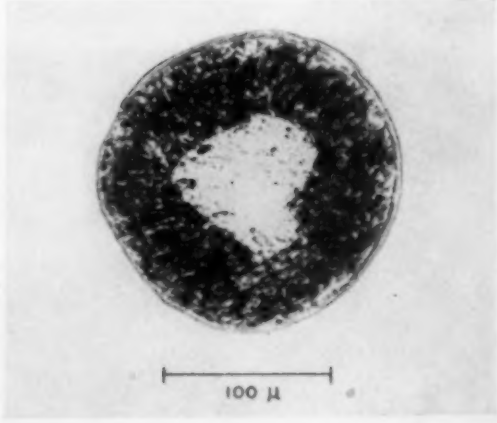

FIGURE 15. *Cross section of a hair from Grevy's Zebra, Equus grevyi.*

From U. S. National Museum specimen 163238.

FIGURE 16. *Cross section of a hair from the wild horse, Equus przewalskii.*

From U. S. National Museum specimen 260018.

UNIVERSITY OF MICHIGAN LIBRARIES

FIGURE 17. *Cross section of a hair from the wild ass, Equus hemionus.*

From U. S. National Museum specimen 84083.

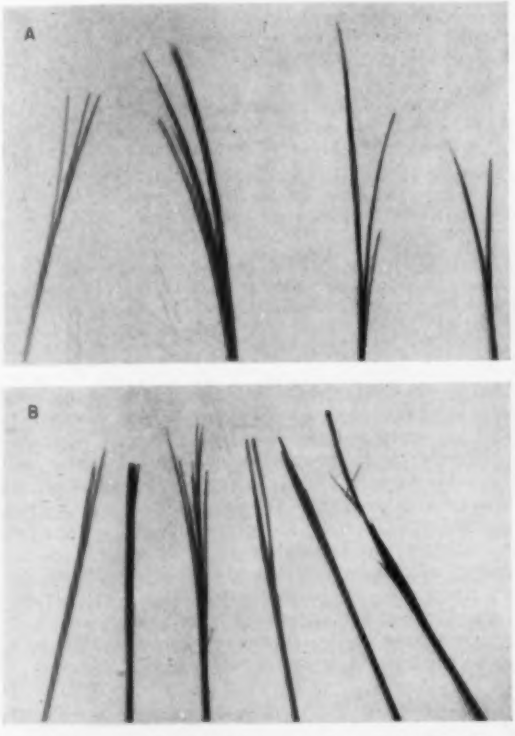

FIGURE 19. *A, Natural bristle flags; B, artificially flagged horsehair.*

Approximately × 6 natural size.

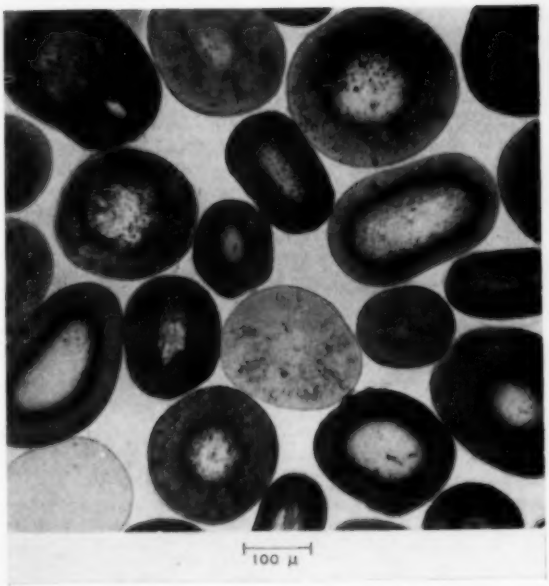

FIGURE 18. *Cross sections of dyed horsehair.*

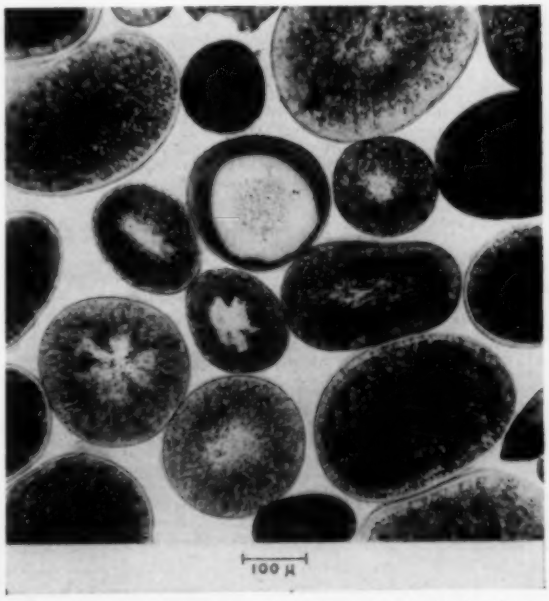

FIGURE 20. *Cross section of fibers from a brush showing horsehair and bristle.*

WASHINGTON, December 28, 1951.

Journal of Research of the National Bureau of Standards Vol. 48, No. 4, April 1952 Research Paper 2316

The System Beryllia-Alumina-Titania: Phase Relations and General Physical Properties of Three-Component Porcelains[1]

S. M. Lang, C. L. Fillmore, and L. H. Maxwell

The data obtained in the investigation of the phase equilibria in the systems beryllia-alumina, beryllia-titania, and alumina-titania suggest that the published equilibrium diagrams of these systems need to be revised: the system BeO-TiO_2 shows no compounds, an eutectic at about 85 weight percent of TiO_2 and 1,670° ±3° C, and an area of TiO_2 solid-solution. The system BeO-Al_2O_3 has three eutectics: (1) at 1,890° ±10° C and about mole ratio 1BeO:4Al_2O_3 (94.2% Al_2O_3); (2) at 1,850° ±10° C and about mole ratio 2BeO:3Al_2O_3 (85.9% Al_2O_3); and (3) at 1,835° ±10° C and about 75 weight percent of Al_2O_3, and two congruently melting compounds, BeO.3Al_2O_3 (92.4% Al_2O_3) at 1,910° ±10° C and chrysoberyl (BeO.-Al_2O_3—80.3% Al_2O_3) at 1,870° ±10° C. The system Al_2O_3-TiO_2 has two eutectics: (1) at 1,705° ±5° C and about 20 weight percent of Al_2O_3; and (2) at 1,840° ±10° C and about mole ratio 5Al_2O_3:4TiO_2 (61.5% Al_2O_3), and a high- and low-temperature form (alpha and beta) of aluminum titanate (Al_2O_3.TiO_2—56.1% Al_2O_3); the alpha form is stable from the alpha-beta inversion temperature of 1,820° ±10° C and melts congruently at 1,860° ±10° C, and the beta form seems to be stable for periods up to 100 hours from room temperature to about 750° C and from about 1,300° C to its inversion temperature. The equilibria for the system BeO-Al_2O_3-TiO_2 was found to contain four invarient points: (1) at 1,572° ±5° C and about mole ratio 2BeO:1Al_2O_3:2TiO_2 (16.1% BeO, 32.7% Al_2O_3, 51.2% TiO_2); (2) at 1,577° ±5° C and about mole ratio 2BeO:1Al_2O_3:4TiO_2 (10.6% BeO, 21.6% Al_2O_3, 67.8% TiO_2); (3) at 1,580° ±5° C and about mole ratio 1BeO:1Al_2O_3:1TiO_2 (12.1% BeO, 49.3% Al_2O_3, 38.6% TiO_2); and (4) probably at about 1,755° ±10° C and about mole ratio 2BeO:5Al_2O_3:2TiO_2 (7.0% BeO, 79.8% Al_2O_3, 22.2% TiO_2). No ternary compounds were found in this system.

The general physical properties of practically impervious porcelains of this system were found to be: maturing range, usually 1,525° to 1,575° C, but with some of the high-alumina-containing bodies maturing between 1,600° and 1,700° C; apparent density, 3.3 to 3.7 g/cm³; shrinkage, 11 to 19 percent; room-temperature compressive strength, 187,000 to 280,000 lb/in.²; room-temperature transverse strength, 13,700 to 25,000 lb/in.²; Young's modulus at room temperature, 42,000,000 to 47,000,000 lb/in.²; transverse strength at 1,800° F (982° C), 10,500 to 17,000 lb/in.²; approximate Young's modulus at 1,800° F, 22,000,000 to 41,000,000 lb/in.²; relative thermal-shock resistance, poor; and the linear thermal expansion of a few selected bodies, in the range 25° to 950° C, usually was regular and ranged from 0.81 to 0.89 percent.

1. Introduction

The choice of the maximum gas or flame temperature in a gas-turbine or jet-propulsion engine is always a compromise between the demands of the designer and the characteristics of the available materials. Ceramic oxide porcelains offer materials of improved strength at temperatures above 1,800° F, as compared to metallic alloys, but the inherently low relative resistance to thermal shock is a serious deterrent to their use. Consequently, the development of pure-oxide porcelains having both high strength and low thermal expansion should prove of considerable interest to design engineers.

Recently, attention has been devoted to the compound aluminum titanate (Al_2O_3.TiO_2) because of its low linear thermal expansion (actually negative over a considerable temperature interval) in the range room temperature to about 1,000° C. This study was undertaken in the hope that the low expansivity of this material could be combined with the high thermal conductivity of beryllium oxide to obtain a refractory porcelain that would exhibit high resistance to thermal shock, high strength at elevated temperatures, low density, and that would be corrosion and erosion resistant.

Although such properties would be particularly applicable to turbine blades for an aircraft engine, it is important to realize that the use of oxide porcelains in future industrial units, such as a gas turbine for marine or land installation, may be of equal and possibly of greater importance. In addition, refractory porcelains are of interest to the manufacturers of spark plugs for automotive and aircraft reciprocating engines, to the refractory industry in general, and to the metallurgical industry.

2. Materials, Equipment, and Procedures

The equipment and procedures used in this study have already been described [1 to 4].[2] In addition, a detailed discussion of the operation of the high-temperature thoria-resistor furnaces was published recently [5].

Materials of the highest obtainable purity were used for compounding the specimens for the deter-

[1] This project was sponsored by the Office of Naval Research under Contract Na ori 2-47, ONR Project NR 032-074.

[2] Figures in brackets indicate the literature references at the end of this paper.

UNIVERSITY OF MICHIGAN LIBRARIES

ination of the phase relations in the various systems: beryllia (BeO)—fluorescent grade of over 99.9-percent purity; alumina (Al_2O_3)—"alpha" polishing powder of nominal 99.9-percent purity supplied by the Linde Air Products Co.; and titania (TiO_2)—spectroscopic grade of over 99.9-percent purity. Commercially available materials of high purity were used in the preparation of test specimens for the determination of physical properties: beryllia—low calcined material of nominal 99.7-percent purity; alumina—ground, washed, and sieved material of 99.5-percent purity, supplied through the courtesy of the Champion Spark Plug Co.; and titania—TAM "Titanox A-MO", calcined at 1,100° C. As prepared for use, the materials were, in all instances, sufficiently finely divided to pass the No. 325 U. S. Standard Sieve.

For the convenience of the reader, the test procedures employed are given briefly. Carbon tetrachloride was used for the absorption determinations, and the results were converted to equivalent water-absorption values. Matured bodies were considered to be those having less than 0.1 percent of equivalent water absorption. Shrinkage values were calculated from micrometer measurements both before and after heating. Apparent density values were obtained by calculations based on the volume as determined by a mercury volumeter and the dry weight of the specimen. The ends of the specimens for the compressive-strength tests were ground parallel, so that the height-to-diameter ratio of the samples was approximately 2. The test pieces were placed between graphite-oil lubricated, cold-rolled steel blocks, and the compressive stress was applied at a rate of about 31,250 (lb/in.^{2})/min by a 75,000-lb hydraulic press. Ten cycles of quenching from a furnace at 1,700° F (931° C) to an air blast at room temperature constituted the thermal-shock test. Values for the transverse moduli of rupture and of elasticity were determined at room temperature, using the loading system of a transverse-strength test furnace [4]. Because of the poor thermal-shock resistance of beryllia-alumina-titania porcelains, comparable room-temperature transverse strengths after thermal shocking could not be determined. Young's modulus at room temperature was determined also by a sonic method [6]. The moduli of rupture and of elasticity at 1,800° F (982° C) were determined by loading the specimens in the transverse-strength test furnace [4] at 2-minute intervals in calculated stress increments of 1,500 lb/in.^{2} When it was noted that the deflection following loading continued after the first minute, it was assumed that permanent deformation, or "plastic flow," had occurred. This deformation could be verified when the test pieces were examined for permanent curvature following rupture. In order to investigate the relative magnitude of the deformation, some of the test bars were subjected to a short-time stress-strain test at 1,800° F. Beginning at 6,000-lb/in.^{2} stress, stress increments of 1,500 lb/in.^{2} were added to the bars at 1-hour intervals, or until rupture occurred, during which time the deflection was measured at regular intervals. Interferometric and dilatometric methods were used for the linear thermal expansion measurements.

The reported phase relations for the four systems investigated during this study were determined not only by interpreting the results obtained mainly from the melting-point and softening-range observations, but also from petrographic and X-ray examinations. The details of the melting-point and softening-range method are given in the publication devoted to the determination of the melting point of alumina [1] and in others [2, 3]. In addition, the three low-melting invariant-point temperatures for the system BeO–Al_2O_3–TiO_2 were redetermined, using a conventional type platinum-wound quenching furnace. The differences observed, using the two methods, are discussed in section 4.1.

The assignment of mole ratios to the various binary and ternary invariant points is not intended to indicate a belief that such invariant points correspond to definite mole ratios; hence, when an invariant point is described, it is said to be located "at about mole ratio . . . ." The experimental work was done on the mole-ratio basis because if there is an unknown compound present, its composition will nearly always correspond to a simple molecular ratio, and, if sufficient simple mole-ratio mixtures are heated, the chances of missing the compound are minimized, regardless of the type of investigational procedure employed.

3. Subordinate Binary Systems

When this investigation was first undertaken, it was assumed that the equilibria of the three subordinate binary systems had been determined adequately. However, when it became necessary, because of inconsistant data, to redetermine the critical mixtures in each of the systems, it was found that the results of the present study did not agree in many respects with those given in the literature.

3.1. The System Beryllia-Titania

The equilibria in this system were described by Wartenburg, et al. [7] as including two congruently melting compounds, $3BeO.TiO_2$ at about 1,800° C and $BeO.TiO_2$ at about 1,720° C. The results of the present investigation (fig. 1) indicate that the system contains no compounds, that a single eutectic exists at about 85 weight percent of TiO_2 and 1,670° ±3° C, and that a narrow region of TiO_2 mixed crystals (an area of solid-solution) extends from just beyond the eutectic to pure titania. Early in the study, seven mixtures, ranging in composition from about 55 to 94 percent of TiO_2, were specially heat-treated for X-ray diffraction examination. Each of the mixtures was heated to about 10 to 15 deg C above the melting point of the mixture as given by Wartenburg, cooled to the reported solidus temperatures, that temperature maintained for about 2 hours, and the mixture then cooled fairly rapidly (about 400 deg C/hr to about 1,000° C).

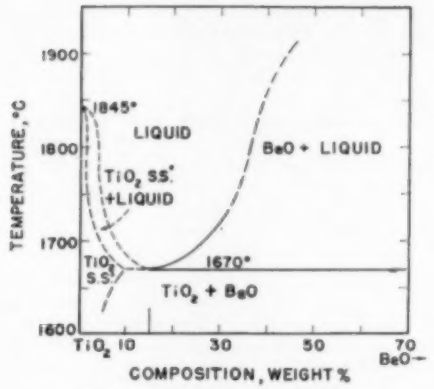

FIGURE 1. *The system beryllia-titania.*
*Solid solution.

X-ray examination revealed that no compounds had been formed and that the specimens consisted entirely of bromellite (BeO) and rutile (TiO_2).

Because the equipment was not available for high-temperature quenching studies, all the mixtures studied had to be cooled relatively slowly from the liquidus temperatures. As a result, neither petrographic nor X-ray examinations could substantiate the existence of the high-temperature solid-solution, and the results are necessarily based upon the observed melting behavior of the mixtures. All the observations of melting behavior of compositions in this system were made on specimens prepared from ground and repressed mixtures that had been calcined at 1,650° C for either 4 or 5 hrs. Table 1 gives the results of the petrographic and X-ray examinations of some of the mixtures studied in the system BeO-TiO_2.

A limited study by the Pennsylvania State College [8] of some of the porcelains in this system indicated that no compounds were formed, and it was suggested that a solid-solution exists at higher temperatures.

3.2. The System Beryllia-Alumina

A considerable amount of work has been done on the system beryllia-alumina. In 1932 Wartenburg and Reusch [9] described this as a simple eutectic system. In 1946 Geller, et al. [2] crystallized and determined the congruent melting point of the compound chrysoberyl ($BeO.Al_2O_3$). They suggested that the chrysoberyl could take at least 2 moles, but not 3 moles, of alumina into solid solution. Recently, Foster and Royal [10] in an investigation of alumina spark-plug bodies found that the compound $BeO.3Al_2O_3$ exists in the system. They did not determine the melting point of that compound, but, through a detailed discussion of previous work on the beryllia-alumina system, they suggested the possible forms for the equilibrium diagram, pending determination of whether the compound $BeO.3Al_2O_3$ melted congruently or incongruently.

Figure 2 shows the equilibrium diagram of the system as redetermined for this study. Three eutectics were located: (1) at 1,890° ±10° C and about mole ratio $1BeO:4Al_2O_3$ (94.2% Al_2O_3); (2) at 1,850° ±10° C and about mole ratio $2BeO:3Al_2O_3$ (85.9% Al_2O_3); and (3) at 1,835° ±10° C and about 75 weight percent of Al_2O_3. The melting point of the recently reported compound $BeO.3Al_2O_3$ (92.4% Al_2O_3) was found to be congruent at 1,910° ±10° C, and that of chrysoberyl ($BeO.Al_2O_3$ —80.3% Al_2O_3) was redetermined at 1,870° ±10° C. An interesting feature of the new compound, as pointed out by Foster and Royal, is that its optical properties are almost identical to those of chrysoberyl, and that the only reliable identification method is by X-ray examination. Table 2 gives the results of the petrographic and X-ray examinations of some of the compositions for this system. More than 95-per-

TABLE 1. *Results of melting-point and softening-range observations and of petrographic and X-ray examinations of some mixtures in the system* BeO-TiO_2

Composition				Maximum temperature	Effect of heating [a] (all temperatures in °C)	Results of petrographic and X-ray examinations [b]	Test
BeO	TiO_2	BeO	TiO_2				
Mole	*Mole*	*wt %*	*wt %*	°C			
4	1	55.61	44.39	1,850	Fusion began at 1,668°, not completed at 1,850°.	Bromellite occurs as 60-μ crystals in a matrix of 40-μ rutile.	779
3	1	48.44	51.56	1,801	Fusion began at 1,672°, not completed at 1,801° (nor at 1,850° for another specimen).	Similar to $4BeO:1TiO_2$, but with somewhat larger interstitial rutile crystals. X-ray: BeO plus TiO_2.	708
2	1	38.51	61.49	1,752	Fusion began at 1,672°, almost completed at 1,752°.	Bromellite is blocky and the rutile is sponge-like with small round and dendritic BeO inclusions. X-ray: BeO plus TiO_2.	742
1	1	23.85	76.15	1,698	Fusion began at 1,668°, completed at 1,698°.	Beryllia occurs as rounded crystals somewhat smaller than the rutile and also as dendritic inclusions in the rutile. X-ray: BeO plus TiO_2.	734
.....	.....	15.00	85.00	1,697	Fusion began at 1,669°, completed at less than 1,697°. Rapid melting at 1,674°.	Large rutile grains with dendritic bromellite inclusions. Single bromellite grains are rare. X-ray: BeO plus TiO_2.	732
1	4	7.26	92.74	1,698	Fusion began at 1,680°, completed at less than 1,686°.	Large (100-μ) rutile and small bromellite. Dendritic and round bromellite inclusions in rutile. X-ray: BeO plus TiO_2.	713
.....	.....	4.00	96.00	1,749	Fusion began at 1,687°, completed at 1,749°.	Similar to $1BeO:4TiO_2$, but with less bromellite.....	792-N

[a] In most cases, the beginning of fusion as indicated is for the test of the specimen described and is usually within 2° C of the average value obtained for three or more determinations of the same mixture. The term "complete fusion" means that the pyramidal specimen had fused sufficiently to flow into a flat button shape and does not necessarily connote that the mixture had completely liquefied.

[b] Specimens examined were not quenched, and the phases observed may not be those in equilibrium at the maximum temperature of heating or at the liquidus.

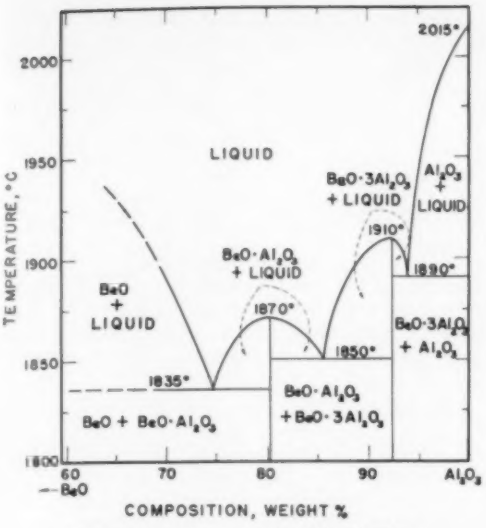

FIGURE 2. *The system beryllia-alumina.*

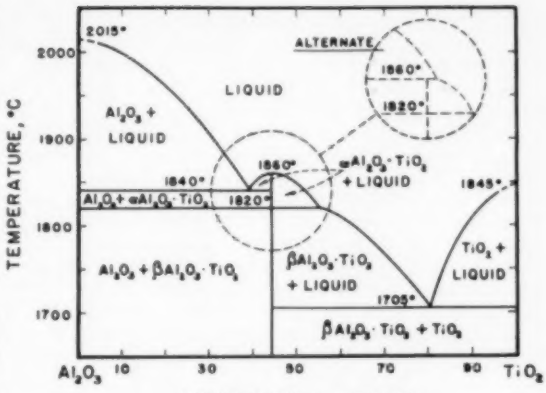

FIGURE 3. *The system alumina-titania.*

cent conversion to the compound chrysoberyl was found when equimolar mixtures of beryllia and alumina were heated at 1,250° C for 4 hrs.

In this system an unidentified phase of high index, $\eta = 1.80$ to 1.81, was found petrographically to be most pronounced, ranging up to an estimated 10 percent by volume, in those mixtures whose compositions ranged from chrysoberyl to alumina. Another unidentified phase, ranging up to an estimated 15 percent by volume, was found by X-ray examination in those mixtures whose compositions ranged from chrysoberyl to beryllia. The phase observed by X-rays was found to have a major *d*-spacings of 3.13, 2.71, and 1.916 ($CuK_{\alpha 1}$). In no instance was it possible to determine the presence of both unidentified phases in the same specimen and there was no indication that both phases were similar in any respect. In addition, it was not possible at any time to identify either phase in the same specimen by both petrographic and X-ray examinations. The amount of contamination in these specimens was shown by spectrographic analyses to be very small, not exceeding 0.05 percent, although previous experience [1] had shown that when alumina was melted in the thoria-resistor furnaces contamination of the melt by the furnace atmosphere resulted.

3.3. The System Alumina-Titania

a. Phase Relations

The reports of both Wartenburg [9] and Bunting [11] on this system indicated a eutectic at about 20 weight percent of alumina and about 1,710° C, a congruently melting compound at about 1,860° C ($Al_2O_3.TiO_2$—as determined by Bunting), and a eutectic at about 62 weight percent of alumina and about 1,850° C. The results of this study, figure 3, are

TABLE 2. *Results of melting-point and softening-range observations and of petrographic and X-ray examinations of some mixtures in the system* $BeO–Al_2O_3$

Composition				Maximum temperature	Effect of heating [a] (all temperatures in °C)	Results of petrographic and X-ray examinations [b]	Test
BeO	Al_2O_3	BeO	Al_2O_3				
Mole	*Mole*	*wt %*	*wt %*	°C			
------	------	4.00	96.00	1,900	Fusion began at 1,895°, not completed at 1,900°.	Corundum occurs as large polyhedral grains as the primary phase, with large matrix grains of $BeO.3Al_2O_3$. X-ray: 10 to 20% Al_2O_3; remainder $BeO.3Al_2O_3$.	871–N
1	4	5.78	94.22	1,899	Fusion began at 1,886°, completed at less than 1,899°. Rapid melting at 1,895°.	$BeO.3Al_2O_3$ appears to be primary phase—100-μ polyhedral grains. Small amount round corundum. X-ray: 5% Al_2O_3, remainder $BeO.3Al_2O_3$.	867–N
1	3	7.56	92.44	1,915	Fusion completed at less than 1,915°....	Practically all $BeO.3Al_2O_3$ as 200-μ plates or flakes. X-ray: All $BeO.3Al_2O_3$.	879
2	3	14.06	85.94	1,865	Fusion began at 1,846°, completed at less than 1865°. Rapid melting at 1,850°.	X-ray: 55% $BeO.3Al_2O_3$, 45% chrysoberyl.	850–N
1	1	19.71	80.29	1,870	Fusion began at 1,843°, rapid melting and completed at 1,868°, completed fusion at 1,870°.	Chrysoberyl appears dirty from less than 1-μ inclusions and occurs as large plates or flakes.	854
------	------	25.00	75.00	1,860	Fusion began at 1,837°, completed at less than 1,860°.	Practically all chrysoberyl. Edges of crystals appear cloudy, with 5-μ intermixed beryllia.	909–N
2	1	32.99	67.01	1,881	Fusion began at less than 1,843°, not completed at 1,881°.	Chrysoberyl appears cloudy, with inclusions of bromellite. X-ray: 75% chrysoberyl and bromellite.	862

[a] In most cases, the beginning of fusion as indicated is for the test of the specimen described and is usually within 5° C of the average value obtained for three or more determinations of the same mixture. The term "complete fusion" means that the pyramidal specimen had fused sufficiently to flow into a flat button shape and does not necessarily connote that the mixture had completely liquefied.

[b] Specimens examined were not quenched, and the phases observed may not be those in equilibrium at the maximum temperature of heating or at the liquidus.

generally in close agreement with the results of those investigations. In addition, however, it was found that there are two forms of aluminum titanate.

Two eutectics were located at 1,705° ±5° C and about 20 weight percent of Al_2O_3 and at 1,840° ±10° C and about mole ratio $5Al_2O_3$:$4TiO_2$ (61.5% Al_2O_3). The beta, or low-temperature, form of aluminum titanate ($Al_2O_3.TiO_2$, 56.1% Al_2O_3) seems to be stable for periods up to about 100 hr in the range from room temperature to about 750° C and from about 1,300° to its inversion temperature at about 1,820° C. The alpha, or high-temperature, form is stable from 1,820° to its melting point at 1,860° ±10° C. It is realized that the equilibria proposed for the low-temperature stability of the beta form of the equimolar compound is not correct, but it was not considered of sufficient interest to devote considerable time and effort to completely investigate the kinetics of the problem. All the observations of melting behavior of compositions in this system were made on specimens prepared from ground and repressed mixtures that had been calcined at either 1,675° or at 1,800° C for 2 hr. Table 3 gives the optical and X-ray properties of the two forms of aluminum titanate, and table 4 gives the results of the petrographic examinations of some of the mixtures of this system.

Because of the very viscous nature of the liquids formed when mixtures of alumina and titania were heated, especially for those containing more than 40 weight percent of alumina, considerable difficulty was experienced in interpreting the melting-point

TABLE 3. *Optical and X-ray properties of alpha and beta aluminum titanate*

Optical properties			X-ray diffraction patterns ($CuK\alpha_1$ radiation)			
	$\alpha Al_2O_3.TiO_2$	$\beta Al_2O_3.TiO_2$	$\alpha Al_2O_3.TiO_2$		$\beta Al_2O_3.TiO_2$	
			d [a]	I	d [b]	I
Refractive indices (±0.01):			4.16	30	4.83	16
N_α	1.89	1.95	3.76	15	4.73	45
N_β	1.91	1.97	3.13	45	3.36	80
N_γ	1.93	1.99	2.836	23	2.657	100
2 V	Nearly 90°	Large	2.718	16	2.366	16
Birefringence	Medium	Medium	2.601	100	2.146	42
Optical sign	Not determined	(−)	2.203	30	2.120	25
Color	Colorless	Blue pleochroism	1.871	36	1.902	75
Form	Plates	Plates and needles	1.820	80	1.797	44
Cleavage	Parallel to N_α	Parallel to N_α	1.718	18	1.786	17
Extinction	Parallel	Parallel	1.634	18	1.689	22
Axial angle	Very large	Very large	1.563	18	1.607	22
			1.542	16	1.578	25
			1.466	21	1.489	25
			.....	.....	1.482	36
			.....	.....	1.251	12

[a] The strip-chart recording shows a total of 31 peaks for $\alpha Al_2O_3.TiO_2$, many of them were very weak (test 512).
[b] The strip-chart recording shows a total of 42 peaks for $\beta Al_2O_3.TiO_2$, many of them were very weak (11-21-49).

TABLE 4. *Results of melting-point and softening-range observations and of petrographic and X-ray examinations of some mixtures in the system* Al_2O_3–TiO_2

Composition				Maximum temperature	Effect of heating [a] (all temperatures in °C)	Results of petrographic and X-ray examinations [b]	Test
Al_2O_3	TiO_2	Al_2O_3	TiO_2				
Mole	*Mole*	*wt %*	*wt %*	°C			
2	1	71.84	28.16	1,880	Fusion began at 1,868°, not complete at 1,880°.	Corundum occurs as blocky crystals (50%). About 10% $\alpha Al_2O_3.TiO_2$ occurs as round or dendritic inclusions in $\beta Al_2O_3.TiO_2$—may be an exsolution texture.	762–N
5	4	61.46	38.54	1,850	Fusion began at 1,836°, very rapid at 1,837°, completed at less than 1,850°.	Practically all $\beta Al_2O_3.TiO_2$, but with a small amount of intermixed corundum and rutile as dendrites.	728
9	8	58.76	41.24	1,858	Fusion began at 1,838°, rapid at 1,840°, completed at less than 1,858°.	Rutile and corundum only. Rutile in form of grains, and dendrites appears interstitial to blocky corundum.	727
1	1	56.06	43.94	1,871	Fusion began at 1,839°, completed at less than 1,870°. Crystallization at 1,818°.	Slowly heated and cooled specimen showed polyhedral grains of $\beta Al_2O_3.TiO_2$ and some corundum.	802
1	1	56.06	43.94	1,839	Fusion began at 1,808°, rapid at 1,830°, not complete at 1,839°.	Rapidly heated and cooled specimen showed varying amounts of α and $\beta Al_2O_3.TiO_2$ in different portions of the specimen. Alpha phase ordinarily 100 by 200 μ, 85% of central portion.	806
4	5	50.57	49.43	1,851	Fusion began at 1,822°, completed at less than 1,851°.	Very large plates of $\beta Al_2O_3.TiO_2$ (400 by 1,000 μ) with droplets of rutile on surfaces.	735–LB
2	3	45.96	54.04	1,859	Fusion began at 1,712°, completed at less than 1,859°. Crystallization at 1,847°.	Large needles of $\beta Al_2O_3.TiO_2$ (150 by 1,000 μ) with interstitial rutile.	751–N
1	5	20.33	79.67	1,710	Rapid and complete fusion at less than 1,710°.	Intermixed rutile and $\beta Al_2O_3.TiO_2$ as eutectic area mosaic.	738–LB

[a] In most cases, the beginning of fusion as indicated is for the test of the specimen described and is usually within 5° C of the average value obtained for three or more determinations of the same mixture. The term "complete fusion" means that the pyramidal specimen had fused sufficiently to flow into a flat button shape and does not necessarily connote that the mixture had completely liquefied.
[b] Specimens examined were not quenched, and the phases observed may not be those in equilibrium at the maximum temperature of heating or at the liquidus.

UNIVERSITY OF MICHIGAN LIBRARIES

softening-range data. The information gathered on the nonstable melting relations indicated another compound (at about 58% of alumina) in the system in addition to aluminum titanate (56.1% of alumina). This new phase was later identified as being the high-temperature form (alpha) of the equimolar compound. The shifting of the maximum melting-point temperature around the 1:1 mixture toward alumina indicated an incongruent melting of aluminum titanate or a solid-solution of alumina in aluminum titanate. Eight mixtures in addition to the 1:1, containing between 50 and 65 weight percent of alumina, were prepared and their melting points and fusion ranges determined, using both conventional and rapidly heated and cooled furnace schedules. The results of these tests indicated (1) the existance of an eutectic at about mole ratio $5Al_2O_3 : 4TiO_2$, (2) the existance of the alpha form of aluminum titanate, and (3) the maximum liquidus temperature for the series of mixtures located very close to the 1:1 composition. Although these results seem to show that the Al_2O_3:TiO_2 melts congruently, the possibilities of incongruent melting and of alumina-aluminum titanate solid-solution cannot be discarded entirely because of the extreme difficulty experienced in determining the high temperatures involved, especially with the viscous nature of the liquids formed at those temperatures.

In order to obtain the two forms of the aluminum titanate, it was necessary to heat the samples very rapidly in the range 600° to 1,500° C (usually not over 1½ hr) and to cool at a rate of at least 800 deg C/hr (actually cooled 400 deg C in the first 5 min). Because of the poor thermal-shock resistance of the thoria muffle in the furnace, only a limited number of tests of this type were practicable. It was only by this means, however, that the alpha form could be partially "frozen" in the samples. Slow cooling permitted complete reversion of the alpha to the beta form in every instance, indicating that the reaction is reversible.

b. The Compound Aluminum Titanate

A communication from the Pennsylvania State College [12] gave the information that the linear thermal expansion of aluminum titanate in the range from room temperature to about 1,000° C was less than that of fused silica. Accordingly, the compound was formed, the linear thermal expansion was measured, and the result was found to agree. However, during a second determination of the expansivity, when the test temperature was raised to 1,500° C, a very marked increase in the expansion rate for the material was found. An additional determination was made using the same specimen and heating it to the same maximum temperature. The high expansion rate was verified. During the correlation of these results, it was noted that the maximum negative expansion value and temperature during heating, the temperature at which the expansion became positive during heating, and the heating and cooling curves were markedly different for each test. Another test sample was prepared, and the expansivity to 1,500° C was determined twice, using this same specimen. The results of these tests are shown in figure 4. A phase change was indicated in all the expansivity determinations for the compound by the change in slope of the heating curve between about 1,100° and 1,300° C, combined with the difference in the heating and cooling curves, and the growth of the specimen after each test. However, no transitions in the range 900° to about 1,350° C were evident by differential thermal analyses.

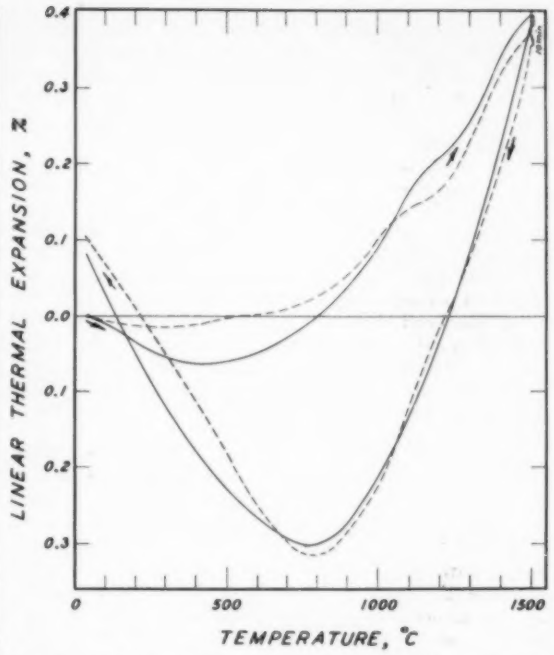

FIGURE 4. *Linear thermal expansion of beta aluminum titanate.*

Test specimen was prepared from equimolar proportions of the oxides, pressed at 9,400 lb/in.², and heated at 1,800° C for 1 hour before testing. 1st test curve ——, 2d test curve – – –.

An investigation of the possible dissociation of the compound was then undertaken. The relative amounts of the formation, decomposition, and reformation products of aluminum titanate were estimated in volume percentages by petrographic examination. Original crystallization was accomplished by heating equimolar mixtures of alumina and titania at temperatures of 1,600°, 1,700°, and 1,800° C for 1 hr.

Three groups of raw materials of varying purities were used. Series A material was made from oxides of the highest purity obtainable (the same as those used for the phase-relation studies), series B material was made from commercially available, high-purity oxides (the same as those used for the determination of physical properties), and series C material was made from commercially available, high-purity alumina and spectroscopic grade titania. For each of the groups complete conver-

sion to the compound resulted from the 1,800° C electric-furnace heat treatment. After the 1,700° C treatment, the B and C mixtures were completely converted, but the purest mixture was 98 percent converted. After the 1,600° C treatment the impure mixtures were 95 to 98 percent converted to the compound, and the A mixture was 90 percent converted. In addition, two trials at low temperature were carried out for the very pure, A, mixture; after 8 hr at 1,350° C, the material contained about 5 percent of aluminum titanate, but after 20 hr at 1,300° C the specimen contained about 10 percent. When heated for 1 hr at 1,700° C in a gas-fired furnace, about 95 percent of the highest purity mixture was converted to the compound. These results indicate that the higher the purity of the original materials, the more difficult is the formation of the compound at temperatures below 1,800° C.

One sample of the A material, which had been heated at 1,800° C in an electric furnace, and one sample of the B material, which had been heated at 1,700 ° C in a gas-fired furnace, were reheated at 1,200° C for 25 hr. The result was that only about 2 percent of the compound remained in the A material, and only about 5 to 8 percent remained in the B material. This indicated that decomposition data would not only be necessary for the phase-equilibrium investigation, but would be equally important to the industrial fabricator using high-purity commercially available materials. Therefore, two bulk samples of series A and series B materials were prepared. Table 5 gives the results of the petrographic examinations of a number of these samples, which had received various heat treatments, for the study of the formation, decomposition, and re-formation characteristics of aluminum titanate.

From these and earlier results it was found: (1) that an area of instability exists for the compound in the temperature range from about 750° to 1,300° C, (2) that, generally, the purer the component oxides used for the formation treatment, the more easily the compound is decomposed, (3) that re-formation from the decomposed state seems to occur more readily for the pure material than for the originally less pure material, (4) that the effect of gas firing as the method of heat treatment increases the formation and re-formation rates, regardless of the purity of the material, and (5) that it appears that two simultaneous processes, formation and decomposition, occur within a mixture of alumina and titania during the lower temperature treatments (about 1,100° to 1,300° C) with decomposition proceeding at a faster rate than formation after a time interval of something less than 25 hr.

A recent report by Hamelin [13] substantiates to a certain extent the upper limit of the aluminum titanate instability region reported in this paper. She found that heating equimolar mixtures of alumina and titania, with and without a 5-percent addition of boric oxide as a mineralizer, at 1,250° C for ½- and 1-hr periods resulted in no combination but that heating the same mixture for 10 min at 1,450° C resulted in complete conversion to the compound.

In addition, limited investigation of the properties of aluminum titanate bodies prepared both from raw and prereacted materials revealed that (a) pure alu-

TABLE 5. *Effects of various heat-treatments on the compound aluminum titanate*

Bulk [a] sample	Formation				Decomposition				Re-formation			
	Code	Temperature	Time	$Al_2O_3.TiO_2$ [b]	Code	Temperature	Time	$Al_2O_3.TiO_2$ [b]	Code	Temperature	Time	$Al_2O_3.TiO_2$ [b]
		°C	hr	%		°C	hr	%		°C	hr	%
A–1	830–P	1,300	20	10								
A–2	828–P	1,350	8	5								
					780–P	800	72	97				
					759–P	900	25	90				
A–3	703–LB	1,700	1	98	758–P	1,000	25	20				
					756–P	1,100	25	10				
					754–P	1,150	25	5				
									815–P	1,500	1	95
									817–P	1,500	4	95
A–4	727–LB	1,800	2	99 to 100	811–P	1,200	25	2	821–P	1,400	4	60
									828–P	1,350	8	25
									830–P	1,300	20	25
A–5	746–LB	1,815	¼	98	839–P	1,250	25	2				
					791–P	700	168	96				
					787–P	700	100	97				
					783–P	700	72	98				
					780–P	800	72	92				
					777–P	800	47	97				
					760–P	850	25	99				
					759–P	900	25	95				
B	52–R	1,700	1	100	758–P	1,000	25	75				
					756–P	1,100	25	5 to 10				
					767–P	1,150	100	0				
					763–P	1,150	66	<1				
					754–P	1,150	25	10				
									815–P	1,500	1	90
									817–P	1,500	4	92
					811–P	1,200	25	5 to 8	821–P	1,400	4	40
									828–P	1,350	8	20
									830–P	1,300	20	25

[a] "All of the "A" series were made from oxides of the highest purity obtainable and were from the same batch. The "B" sample was made from high-purity, commercially available oxides.

[b] Volume percentages of aluminum titanate estimated petrographically.

UNIVERSITY OF MICHIGAN LIBRARIES

inum titanate specimens are extremely friable when formed from the component oxides, (b) shapes have somewhat greater strength when formed from pre-reacted material, (c) the strength at room temperature is poor for either formation procedure when compared to the strengths of normal oxide porcelains, and (d) the linear thermal expansion is very low, but only in the range from room temperature to about 1,000° C.

3.4. Titanium Dioxide

Although it was apparent that titanium dioxide did reduce in the BeO-TiO_2 system, and to a much lesser extent in the Al_2O_3-TiO_2 and BeO-Al_2O_3-TiO_2 systems, the amount of reduction is considered as being in trace quantities because no evidence of reduction could be found by petrographic or X-ray analyses. The discoloration of the samples (to a dark blue-black in extreme cases) is evidence of the reduction of titania, but it is well known that very small amounts of Ti_2O_3 (less than 0.01%) have extremely strong coloring effects. The discoloration was noticed only in those specimens that contained free titania. Otherwise the samples were white or very light tan.

4. The System Beryllia-Alumina-Titania

4.1. Phase Relations

A search of the literature revealed that there are no published reports of a systematic study of the equilibria in the system beryllia-alumina-titania. The results of this investigation are shown in figure 5, in which the indicated equilibria are based on the assumed congruent melting of alpha aluminum titanate (sec. 3.3, a). The limitation of funds did not permit completion of this phase of the investigation.

The report of this project to the Office of Naval Research [14] listed the invariant points of the system as being at (1) 1,575° ±5° C and mole ratio $1BeO:1Al_2O_3:1TiO_2$, (2) 1,579° ±5° C and mole ratio

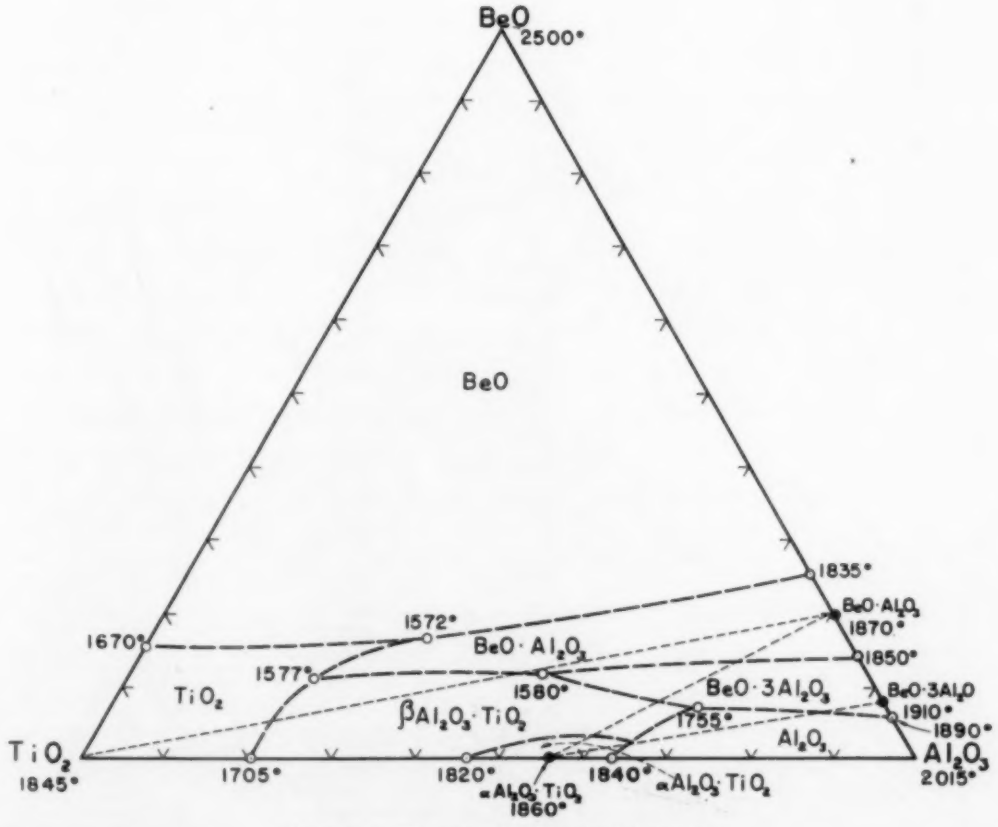

FIGURE 5. *The system beryllia-alumina-titania.*

This figure shows the compatibility triangles, the locations of the primary phase boundaries, and the temperatures (deg. C) of the invariant points. The molecular compositions approximating the invariant point compositions and those of other mixtures studied are shown on figure 7. The temperatures of the three low-melting invariant points within the ternary system were determined from quenching studies, and those of the other invariant points were found from melting-point and softening-range determinations.

$2BeO:1Al_2O_3:2TiO_2$, (3) 1,586° ±5° C and mole ratio $2BeO:1Al_2O_3:4TiO_2$, and (4) probably at about 1,755° ±10° C and about mole ratio $2BeO:5Al_2O_3:2TiO_2$. No ternary compounds or areas of solid solution were positively identified. Results reported to ONR were obtained from melting-point and softening-range studies of compositions prepared from ground and repressed mixtures that had been calcined at about 1,570° C for 1 hr. Table 6 gives the results of petrographic examinations of some of the mixtures studied (see also fig. 6 for the locations of the mixtures on the ternary diagram).

Following the report to ONR and using a conventional type platinum-wound quenching furnace, a limited number of tests for a more accurate determination of the three low-melting invariant point temperatures were made. It was found that at mole ratio $1BeO:1Al_2O_3:1TiO_2$ (12.1% BeO, 49.3% Al_2O_3, 38.6% TiO_2) the solidus temperature was 1,580° ±5°C, at mole ratio $2BeO:1Al_2O_3:2TiO_2$ (16.1% BeO 32.7% Al_2O_3, 51.2% TiO_2) it was 1,572° ±5° C, and at mole ratio $2BeO:1Al_2O_3:4TiO_2$ (10.6% BeO, 21.6% Al_2O_3, 67.8% TiO_2) this temperature was 1,577°±5° C.

TABLE 6. *Results of melting-point and softening-range observations and of petrographic and X-ray examinations of some mixtures in the system* $BeO\text{-}Al_2O_3\text{-}TiO_2$

Composition						Maximum temperature	Effect of heating [a] (all temperatures in ° C)	Results of petrographic and X-ray examinations [b]	Test
BeO	Al_2O_3	TiO_2	BeO	Al_2O_3	TiO_2				
Mole	*Mole*	*Mole*	*wt %*	*wt %*	*wt %*	*° C*			
1	1	1	12.095	49.275	38.63	1,594	Fusion began at 1,575°; complete at less than 1,594°.[c]	Eutectic texture: intermixed blocky, dendritic bromellite (10%) and chrysoberyl or $BeO.3Al_2O_3$ (40%) and round, large rutile crystals (50%). Some rutile appears sponge-like, with unidentified dendritic inclusions. X-ray (808–LB): Rutile and chrysoberyl, possibly some BeO.[c]	887–N
1	1	3	6.83	27.80	65.37	1,614	Fusion began at 1,601°; complete at less than 1,614°.	Dendritic structure of intermixed $\beta Al_2O_3.TiO_2$ chrysoberyl, and rutile. Rutile about 50% by volume.	821–L
1	2	1	8.10	66.02	25.88	1,750	Fusion began at 1,687°; almost complete at 1,750°.	About equal quantities of chrysoberyl or $BeO.3Al_2O_3$ and $\beta Al_2O_3.TiO_2$, both as polyhedral grains, the aluminum titanate being 30 to 150 μ in size.	811–L
1	2	2	6.44	52.45	41.11	1,706	Fusion began at 1,657°; almost complete at 1,706°.	100-μ blocky $\beta Al_2O_3.TiO_2$ (75%) with polyhedral chrysoberyl or $BeO.3Al_2O_3$.	824–LB
1	3	1	6.09	74.46	19.45	1,800	Fusion began at 1,737°; almost complete at 1,800°.	Large plates of chrysoberyl or $BeO.3Al_2O_3$, scales of $\beta Al_2O_3.TiO_2$ on surfaces. About 10% corundum. X-ray (811–L): $BeO.3Al_2O_3$ and $\beta Al_2O_3.TiO_2$.	813–L
2	1	2	16.05	32.70	51.25	1,589	Fusion began at 1,579°; complete at less than 1,589°.[c]	Intermixed, small crystals, bromellite, chrysoberyl and rutile.[c]	822–LB
2	1	4	10.61	21.61	67.77	1,592	Fusion began at 1,588°; complete at less than 1,592°.[c]	Intermixed crystals of rutile (30 μ) and chrysoberyl. Very small, occasional grains of bromellite.[c]	817–L
2	1	6	7.92	16.15	75.93	1,604	Fusion began at 1,589°; complete at less than 1,604°.	Practically all polyhedral rutile filled with inclusions of unidentified material. Occasional chrysoberyl.	926–N
2	1	10	5.26	10.72	84.02	1,700	Fusion began at 1,583°; complete at less than 1,700°.	Same as $2BeO:1Al_2O_3:6TiO_2$ (926–N), except more rutile.	812–LB
3	3	1	16.29	66.37	17.34	1,780	Fusion began at 1,651°; almost complete at 1,780°.	80%, 40-μ, polyhedral chrysoberyl or $BeO.3Al_2O_3$, with small amount free rutile as interstitial material.	931
3	5	1	11.29	76.69	12.02	1,828	Fusion began at 1755°; complete at 1,828°.	Practically all 40 to 100 μ round crystals of chrysoberyl or $BeO.3Al_2O_3$, with small, round inclusions of possibly rutile.	902–N
3	10	1	6.39	86.805	6.805	1,850	Fusion began at 1800°; complete at 1,850°.	Almost all 50-μ polyhedral chrysoberyl or $BeO.3Al_2O_3$, with granular corundum and $\beta Al_2O_3.TiO_2$. X-ray (809–L): $BeO.3Al_2O_3$, with small amounts alpha corundum and $\beta Al_2O_3.TiO_2$.	932–N
3	20	1	3.42	92.94	3.64	1,800	No evidence of fusion at 1,800°.	Large amount of large corundum grains with chrysoberyl or $BeO.3Al_2O_3$ and trace of $\beta Al_2O_3.TiO_2$. X-ray (809–L): $BeO.3Al_2O_3$ and αAl_2O_3.	809–L
4	3	4	13.80	42.15	44.05	1,650	Fusion began at less than 1,591°; complete at less than 1,650°.	Blocky chrysoberyl or $BeO.3Al_2O_3$, with rutile and small amounts of bromellite. X-ray: chrysoberyl, rutile, and trace of bromellite.	804–LB
6	1	10	14.28	9.70	76.02	1,650	Fusion began at 1,592°; complete at 1,650°.	Rutile with interstitial dendritic bromellite and small amount of chrysoberyl or $BeO.3Al_2O_3$. X-ray: Rutile, bromellite, and chrysoberyl.	810–LB
9	1	9	21.53	9.74	68.73	1,646	Fusion began at 1,589°; complete at less than 1,646°.	Blocky bromellite, with blocky and dendritic rutile, some of the rutile being dendritic inclusions.	886
15	10	1	25.45	69.13	5.42	1,830	Fusion began at 1,778°; complete at 1,830°.	Chrysoberyl or $BeO.3Al_2O_3$, with mixed interstitial, dendritic bromellite, and rutile.	934
15	15	1	18.91	76.06	4.03	1,840	Fusion began at 1,803°; complete at 1,840°.	Large chrysoberyl or $BeO.3Al_2O_3$ prisms, with unidentified dark interstitial film. X-ray (809–L): Chrysoberyl.	935–N

[a] In most cases, the beginning of fusion as indicated is for the test of the specimen described and is usually within 3° C of the average value obtained for three or more determinations of the same mixture. The term "complete fusion" means that the pyramidal specimen had fused sufficiently to flow into a flat button shape and does not necessarily connote that the mixture had completely liquefied.

[b] Specimens examined were not quenched, and the phases observed may not be those in equilibrium at the maximum temperature of heating or at the liquidus.

[c] Results of quenching studies: 1:1:1—solidus temperature=1,580° ±5° C, primary phase chrysoberyl; 2:1:2—solidus temperature=1,572° ±5° C, primary phase chrysoberyl; and 2:1:4—solidus temperature=1,577° ±5° C, primary phase rutile.

UNIVERSITY OF MICHIGAN LIBRARIES

In addition to obtaining information on the differences in results that can be expected between the two methods of determining liquidus and solidus temperatures, identification of the primary phases was more readily established when the specimens could be quenched rather cooled relatively slowly as in the oxide-resistor furnaces. It was found also that the 1:1:1 and the 2:1:2 mixtures were located within the chrysoberyl primary phase region, and that the 2:1:4 mixture was located within the rutile field. The linear thermal expansion measurements (see sections 4.2 and 4.3) gave another indication that the 1:1:1 mixture should be located within the chrysoberyl field. It is believed, however, that the true invariant point compositions are located within about 2 weight percent of the compositions of the mole ratios used to describe the invariant points.

4.2. Ceramic Bodies

Tables 7, 8, and 9 give the maturing data, the strength-test values, and the results of the stress-strain studies of various porcelains whose compositions represent that area of the triaxial diagram (fig. 6) in which bodies could be formed with an equivalent water absorption of less than 0.1 percent. Figure 7 shows the stress-strain relations of those bodies selected for transverse-strength testing at 1,800°F. The only porcelain that showed no plastic deformation during the testing had the molecular composition $1BeO:1Al_2O_3:1TiO_2$. Figure 8 shows the effect of ½, 1, and 4 mole additions of beryllium oxide on the linear thermal expansion of the composition $1Al_2O_3:1TiO_2$.

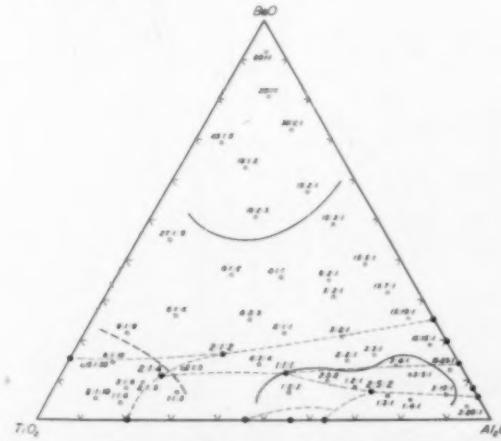

FIGURE 6. *Porcelains of the system beryllia-alumina-titania.*

This figure shows the location of the area in the triaxial diagram (the central portion) in which practically impervious porcelains may be made. Those compositions between the upper heavy line and the BeO-apex, and between the lower heavy line and the Al_2O_3-TiO_2 boundary, could not be matured (less than 0.1% equivalent water absorption). The mixtures shown between the heavy dashed line and TiO_2 were not used for physical property testing. The compositions of the mixtures are indicated on the figure in molar ratios but are placed graphically according to weight percentages.

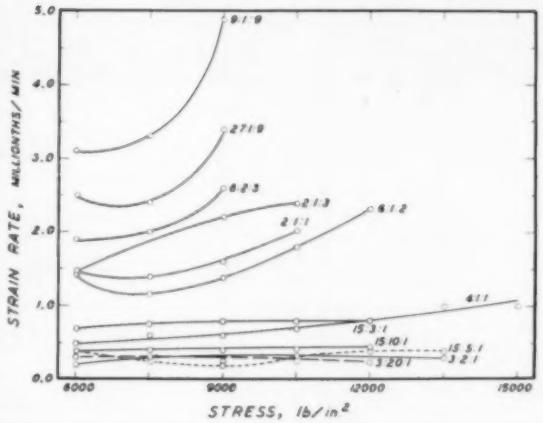

FIGURE 7. *Short-time stress-strain relations of some beryllia-alumina-titania porcelains.*

Shown are the strain rates at 1,800°F (982°C) of some beryllia-alumina-titania porcelains when maintained for 60 minutes at each of the stresses indicated. Rupture occurred during the next highest stress. (See values in table 9).

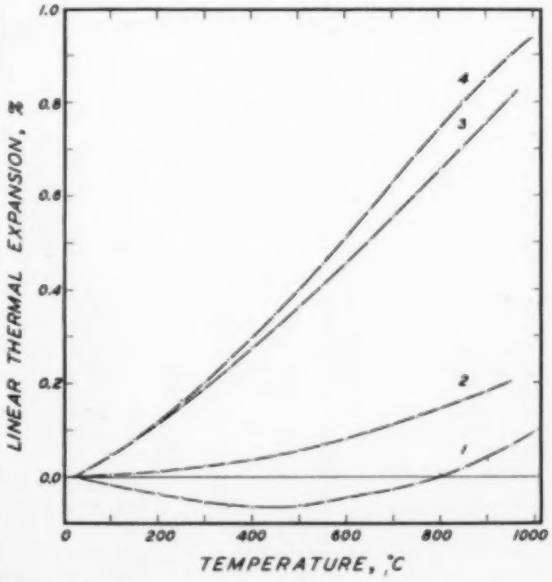

FIGURE 8. *Linear thermal expansion of porcelains on the aluminum titanate-beryllia join.*

These curves show the effect of ½, 1, and 4 mole additions of beryllia on the expansion of the aluminum titanate composition. The expansions of mole compositions $2BeO:1Al_2O_3:3TiO_2$, $6BeO:1Al_2O_3:2TiO_2$, and $3BeO:2Al_2O_3:1TiO_2$ are similar to that of $1BeO:1Al_2O_3:1TiO_2$. Curve 1, Al_2O_3:TiO_2; curve 2, $1BeO:2Al_2O_3:2TiO_2$; curve 3, $1BeO:1Al_2O_3:1TiO_2$; curve 4, $4BeO:1Al_2O_3:1TiO_2$.

UNIVERSITY OF MICHIGAN LIBRARIES

TABLE 7. *Maturing-range studies and compressive-strength results of some* BeO-Al_2O_3-TiO_2 *porcelains* [a]

Molecular and weight-percentage compositions						Results of maturing-range studies						Properties of compressive-strength specimens [b]						
								Properties at maturity										
BeO	Al_2O_3	TiO_2	BeO	Al_2O_3	TiO_2	Maturing range	Test	Temperature	Shrinkage	Absorption	Apparent [c] density (±0.01)	Test	Temperature	Shrinkage	Absorption	Apparent [c] density (±0.01)	Height/diameter ratio [d]	Strength at room temperature [e] (±5,000 lb/in.²)
Mole	*Mole*	*Mole*	*wt %*	*wt %*	*wt %*	°C		°C	*%*	*%*	*g/cm³*		°C	*%*	*%*	*g/cm³*		*lb/in.²*
1	1	1	12.095	49.275	38.63	1,575	679–L	1,575	15.82	0.02	3.67	695–LB	1,575	15.68	0.01	3.66	2.09	[f] 234×10³
2	1	1	21.58	43.96	34.46	1,525 to 1,575	732–L	1,550	14.97	.00	3.62	766–LB	1,550	16.72	.01	3.59	2.19	[f] 187
2	1	2	16.05	32.70	51.25	1,500 to 1,575	.....	1,525 to 1,550	16.32	.00	3.64	769–L	1,525	16.95	.02	3.66	2.13	226
2	1	3	12.775	26.025	61.20	1,525 to 1,575	665–L	1,550	17.44	.01	3.73	693–LB	1,550	17.60	.00	3.76	2.14	[f] 237
2	2	1	14.99	61.075	23.935	1,575 to 1,600	730–L	1,575	13.06	.01	3.59	.....	.....	.....	.....	.....	.....	.....
3	2	1	20.92	56.815	22.265	1,575	679–L	1,575	15.18	.00	3.52	697–LB	1,575	15.87	.01	3.57	2.09	281
3	3	1	16.29	66.37	17.34	1,575	751–LB	1,575	12.42	.01	3.53	772–LB	1,575	13.56	.01	3.50	2.10	[f] 245
3	20	1	3.42	92.94	3.64	1,675 to 1,750	758–LB	1,725	11.46	.02	3.64	776–LB	1,725	12.34	.01	3.64	1.98	[g] 240
4	1	1	35.50	36.16	28.34	1,550 to 1,575	679–L	1,575	16.93	.01	3.43	715–L	1,575	16.59	.01	3.36	2.01	[f] 263
4	3	4	13.80	42.15	44.05	1,525 to 1,575	732–L	1,550	14.97	.01	3.73	768–LB	1,525	15.78	.03	3.63	2.12	[g] 209
.....	.....	.....	.....	.....	.....	.....	.....	.....	.....	.....	.....	.....	.....	.....	.....	.....	.....	.....
5	2	1	30.60	49.86	19.54	1,525 to 1,575	788–L	1,550	14.81	.00	.....	.....	.....	.....	.....	.....	.....	.....
6	1	2	36.45	24.75	38.80	1,550 to 1,575	665–L	1,550	17.60	.06	3.41	699–LB	1,550	17.91	.00	3.45	2.02	277
6	1	4	26.26	17.83	55.91	1,525 to 1,575	698–LB	1,525	18.23	.00	3.52	770–LB	1,525	18.18	.01	3.57	2.19	[f] 216
6	2	1	34.60	46.99	18.41	1,525 to 1,575	788–L	1,550	14.65	.00	.....	.....	.....	.....	.....	.....	.....	.....
6	2	3	25.285	34.34	40.375	1,525 to 1,575	691–L	1,550	16.80	.01	3.59	771–L	1,550	16.97	.02	3.56	2.12	[f] 247
.....	.....	.....	.....	.....	.....	.....	.....	.....	.....	.....	.....	.....	.....	.....	.....	.....	.....	.....
9	1	9	21.53	9.74	68.73	1,525 to 1,550	665–L	1,550	18.71	.01	3.62	701–LB	1,550	18.86	.00	3.62	1.97	247
15	3	1	49.315	40.185	10.50	1,550 to 1,575	763–LB	1,550	16.40	.01	3.27	767–L	1,550	17.13	.02	3.26	2.12	239
15	5	1	38.895	52.825	8.28	1,575 to 1,600	679–L	1,575	15.82	.01	3.34	710–LB	1,575	15.58	.00	3.35	1.91	276
15	7	1	32.11	61.05	6.84	1,525 to 1,575	763–LB	1,550	14.00	.01	3.41	775–L	1,550	15.27	.05	3.39	2.08	[g] 237
15	10	1	25.45	69.13	5.42	1,550 to 1,600	751–LB	1,575	12.73	.01	3.44	764–LB	1,575	14.58	.00	3.47	2.07	[f] 247
.....	.....	.....	.....	.....	.....	.....	.....	.....	.....	.....	.....	.....	.....	.....	.....	.....	.....	.....
15	15	1	18.91	77.06	4.03	1,600	758–LB	1,600	11.14	.01	3.39	778–LB	1,625	12.03	.01	3.37	2.08	[f] 236
15	25	1	12.50	84.84	2.66	1,625 to 1,675	762–LB	1,650	10.99	.01	3.49	.....	.....	.....	.....	.....	.....	.....
27	1	9	45.14	6.81	48.05	1,550	691–L	1,550	18.86	.01	3.32	773–L	1,550	18.28	.00	3.32	2.18	[f] 206

[a] Values obtained for specimens matured in a thoria-resistor (electric) furnace for 1 hr at the temperatures specified.

[b] Unless otherwise indicated, the values given are the averages for three test specimens.

[c] Values calculated from the volume obtained from a mercury volumeter and the dry weight of the specimens.

[d] Specimens were about 1 in. high by ½ in. in diameter.

[e] Compression testing was done at a constant stress rate of 31,250 (lb/in.²)/ min and using cold-rolled-steel blocks for platen protection.

[f] Value given is for two specimens (three were broken, but one had splintered, and that lower value was discarded).

[g] Value given is for one specimen (three were broken, but two had splintered, and those lower values were discarded).

TABLE 8. *Flexural strength, elasticity, and thermal-shock resistance of some* BeO-Al_2O_3-TiO_2 *porcelains* [a]

(None of the test bars survived 10 cycles of test for thermal-shock resistance (from a furnace at 1,700° F (931° C) to an air blast at room temperature)

Mole[b] composition			Maturing data [c]				Strength in bending (flexure) at [d]—				
							Room temperature			1800° F (982° C)	
								Young's modulus (±3×10⁶ lb./in.²)			
BeO	Al_2O_3	TiO_2	Test	Temperature	Absorption	Apparent density (±.003)	Transverse strength (±2,000 lb/in.²)	Static [f] method	Sonic [g] method	Transverse strength (±2,000 lb/in.²)	Young's [e] modulus (±3×10⁶ lb/in.²) (static)
				°C	%	g/cm³	lb/in.²	lb/in.²	lb/in.²	lb/in.²	lb/in.²
1	1	1	76–R	1,575	0.02	3.62	16.4×10³	41.8×10⁶	42.5×10⁶	17.1×10³	35.5×10⁶
2	1	1	77–R	1,550	1.15	3.46	16.8	40.0	41.7	12.2	30.5
2	1	3	55–R	1,550	0.01	3.72	20.8	.....	.....	13.1	30.0
3	2	1	56–R	1,575	ca .15	3.45	20.5	.....	.....	13.5	35.1
3	20	1	78–R	1,525	.09	3.58	[b] 13.8	[b] 48.1	[b] 42.6	[b] 11.9	[b] 39.0
4	1	1	76–R	1,575	.00	3.43	20.1	45.4	46.8	16.1	35.8
6	1	2	55–R	1,550	.01	3.44	25.3	.....	.....	14.6	29.4
6	2	3	77–R	1,550	.02	3.53	21.8	42.1	44.2	10.8	27.7
9	1	9	55–R	1,550	.01	3.64	21.7	.....	.....	11.0	22.5
15	3	1	77–R	1,550	1.7	3.19	19.7	43.2	43.5	14.0	34.8
15	5	1	56–R	1,575	0.02	3.35	24.1	.....	.....	16.0	41.0
15	10	1	76–R	1,575	ca .4	3.36	17.5	43.3	44.1	13.5	36.3
27	1	9	77–R	1,550	ca .6	3.33	20.8	41.0	41.4	11.9	28.0

[a] Values obtained for specimens matured in a gas-fired furnace for 1 hr at the temperatures specified.
[b] The weight compositions of these molar ratio mixtures are given in table 7.
[c] Absorption and apparent density values are the averages for five test bars.
[d] Two test bars, about 5½ by ¾ by ¼ in., of each composition were broken at room temperature, two were thermally shocked, and three were broken for the transverse strength, elasticity, and stress-strain tests at 1,800° F.
[e] Except for body 1:1:1, the modulus of elasticity values (Young's modulus) are considered as only relative because they were calculated from the curve of the deformation versus load at the lowest part of the curve where the plastic flow was a minimum.
[f] The static Young's modulus at room temperature was determined for only one bar specimen of the compositions indicated.
[g] The sonic Young's modulus at room temperature was determined for the two bars of the composition indicated, which were later used for the thermal shock test.
[h] Bars of this composition were tested in bending with a span of about 3½ in. as compared to the normal 4.9- or 5.0-in. span.

TABLE 9. *Short-time (1 hour) stress-strain tests and interval strain rates of some* BeO-Al_2O_3-TiO_2 *porcelains*

[All rates of strain are (in./in.)/min.]

Mole [a] composition			Strain rates at 1,800° F (982° C) [b] and—							Interval strain rates at 1,800° F and—									
										6,000 lb/in.² stress for—					12,000-lb/in.² stress for—				
BeO	Al_2O_3	TiO_2	6,000-lb./in.² stress	7,500-lb./in.² stress	9,000-lb/in.² stress	10,500-lb/in.² stress	12,000-lb/in.² stress	13,500-lb/in.² stress	15,000-lb/in.² stress	0 to 5 min	0 to 10 min	0 to 20 min	0 to 30 min	0 to 60 min	0 to 5 min	0 to 10 min	0 to 20 min	0 to 30 min	0 to 60 min
2	1	1	1.5	1.4	1.6	2.1	(3.5)	.....	.....	3.7	2.9	2.3	1.9	1.5	4.7	4.2	3.5	.....	.....
2	1	3	1.6	.....	2.2	2.4	(3.3)	.....	.....	3.4	3.0	2.3	2.0	1.6	4.5	4.0	3.3	.....	.....
3	2	1	0.2	0.4	0.2	0.3	0.2	0.3	(0.8)	0.6	0.6	0.5	0.5	0.2	0.0	0.0	0.0	0.1	0.2
3	20	1	.3	.3	.2	.2	.2	.....	.....	.7	.6	.5	.4	.3	.4	.2	.3	.2	.2
4	1	1	.7	.6	.6	.7	.8	1.0	1.0	1.7	1.6	1.3	1.1	.7	1.8	1.6	1.4	1.2	.8
6	1	2	1.4	1.3	.....	1.8	2.3	(5.1)	.....	4.0	3.2	2.4	2.0	1.4	3.4	3.2	2.9	2.7	2.3
6	2	3	1.9	2.0	2.6	(4.2)	.....	.....	.....	4.1	3.6	2.9	2.6	1.9	.....	.....	.....	.....	.....
9	1	9	3.1	3.3	4.9	.....	.....	.....	.....	7.2	6.0	4.7	4.0	3.1	.....	.....	.....	.....	.....
15	3	1	0.7	0.6	0.8	0.7	0.8	(0.9)	.....	1.5	1.6	1.2	1.0	0.7	1.4	1.3	1.1	1.0	0.8
15	5	1	.4	.3	.2	.4	.4	.4	.....	2.0	1.6	1.0	0.7	.4	0.7	0.6	0.6	0.5	.4
15	10	1	.3	.4	.4	.4	.4	(1.0)	.....	0.8	0.7	0.6	.5	.3	.6	.6	.5	.5	.4
27	1	9	2.5	2.4	3.4	(5.3)	.....	.....	.....	5.0	4.5	3.7	3.0	2.5	.....	.....	.....	.....	.....

[a] The weight percentages of these molecular compositions, the maturing temperatures, and the properties of the matured porcelains are given in table 7.
[b] Beginning at 6,000-lb/in.² stress, each stress was maintained for 1 hr, or until rupture occurred. The values in parenthesis indicate that the specimen had broken after the stress was applied but before the hourly period had elapsed.

4.3 Discussion

Although the limited information available did not permit statistical analysis of the strength-test data, certain trends were indicated.

a. Room-Temperature Strength Tests

Fairly good agreement was noted for the values of compressive and transverse strength of the bodies (see tables 7 and 8). Those porcelains having the highest compressive strengths also showed the highest transverse strengths, and similarly, the lowest compressive strength bodies showed the lowest transverse strengths.

b. Room-Temperature-Elasticity Tests

Young's modulus of elasticity at room temperature (table 8) was determined by both sonic and static methods, using bar specimens with a span of 5 in. Unfortunately, the sonic apparatus was not used before the bars had been broken transversely, and it is, therefore, impossible to compare the values obtained by the two methods for the same test specimen. However, it was found that the values obtained by the sonic method were consistently only between 1 and 3 percent higher than those obtained by the static method for different specimens of any given composition. Such agreement is considered as being good. When bars of one composition were tested, for which a 3-in. span was used, the agreement was poor.

c. Transverse Strength at Room Temperature Versus Transverse Strength at Elevated Temperature (1,800° F)

The transverse strengths at 1,800° F were ordinarily about 50 percent lower than the values for specimens of the same body composition tested at room temperature (table 8). Those having the highest strengths at room temperature (with one exception) had only medium or low strength at 1,800° F, but those with the lowest strengths at room temperature also had the lowest strengths at 1,800° F.

d. Elasticity at Room Temperature Versus Elasticity at Elevated Temperature (1,800° F)

Young's modulus values from data obtained at 1,800° F were ordinarily 25 to 40 percent lower than the values for specimens of the same body tested at room temperature (table 8). Poor agreement was noted for the relative elasticity values at the two test temperatures. This may have been caused, in part, by the fact that the 1,800° F test values were calculated from the lowest part of the deformation-load diagrams where the "plastic flow" was relatively small; the deformation of any one bar was not a linear function of the loading of the bar, except for those specimens of mole composition $1BeO:1Al_2O_3:1TiO_2$.

e. Stress-Strain Relations Versus Strength and Elasticity at Elevated Temperatures (1,800° F)

Except for the bodies of mole composition $9BeO:1Al_2O_3:9TiO_2$, the strain rates for the beryllia-alumina-titania porcelains at 1,800° F and 12,000 lb/in.^{2} stress (tables 8 and 9) were only about 10 to 25 percent of the values for beryllia porcelains in the system beryllia-alumina-zirconia [4]. It was possible to compare the stress-strain and strength values of the beryllia-alumina-titania porcelains only at stresses between 6,000 and 9,000 lb/in.^{2}. In this stress range, it was noted that there was good agreement between the strain rates and the transverse strength, that is, those bodies showing very little or no strain ordinarily had the highest transverse strengths, and those with the highest strain rates had the lowest transverse strengths. A similar agreement was noted for the strain-rate–modulus-of-elasticity relations.

When the strain rates of the short-time stress-strain tests at 1,800° F were high (above 1.9 (in./in.)/min at 6,000-lb/in.^{2} stress and above 2.6 (in./in.)/min at 9,000-lb/in.^{2} stress) the relatively slow loading rate, (1,500 lb/in.^{2})/hr of the stress-strain test resulted in transverse-strength values as much as 35 percent lower than those obtained with the more rapid loading, (1,500 lb/in.^{2})/2 min, of the regular transverse strength test. The strength values obtained for specimens that had strain rates lower than those indicated were within 3 to 4 percent of each other, regardless of the loading method used. A 5-percent deviation is considered as good agreement.

f. General Discussion of the Porcelains Developed

It is believed that three of the body compositions developed in this investigation ($15BeO:5Al_2O_3:1TiO_2$, $6BeO:1Al_2O_3:2TiO_2$, and $3BeO:2Al_2O_3:1TiO_2$) may find use in high-temperature applications where strength, but not thermal-shock resistance, is of prime importance. The properties determined for these three bodies are compared in table 10 to the range of properties determined for all of the beryllia-alumina-titania porcelains developed.

The high compressive-strength value for the 3:2:1 composition was totally unexpected because the normal crystallization of chrysoberyl would suggest considerably lower strength. This and the 15:5:1 body had the lowest strain rates determined for these porcelains. Of particular interest to those concerned with strength at high temperatures would be the 1:1:1 body; no loss in transverse strength (about 17,000 lb/in.^{2}) was observed at 1,800° F when compared with the value determined at room temperature. However, the 1:1:1 body had a high elasticity—43 million lb/in.^{2} at room temperature and 36 million lb/in.^{2} at 1,800° F.

The expansion characteristics of the three highest strength bodies, $15BeO:5Al_2O_3:1TiO_2$, $6BeO:1Al_2O_3:2TiO_2$, and $3BeO:2Al_2O_3:1TiO_2$, are very similar to that shown by curve 3 of figure 8. It is possible to

UNIVERSITY OF MICHIGAN LIBRARIES

TABLE 10. *Summary and comparison of the physical properties of some beryllia-alumina-titania porcelains*

Composition (mole ratio) BeO:Al_2O_3:TiO_2	Maturing range	Properties at maturity				Room-temperature strength			1,832° F (982° C) strength			Strain rates at—	
		Temperature	Shrinkage	Absorption	Apparent density	Compressive	Transverse	Young's modulus	Transverse	Young's modulus (approximate)	Thermal-shock resistance	6,990 lb./in.² stress	9,980 lb./in.² stress
	°C	°C	%	%	g/cm³	lb./in.²	lb./in.²	lb./in.²	lb./in.²	lb./in.²		(in./in.)/min	(in./in.)/min
All porcelains	1,500 to 1,675	1,525 to 1,650	11.0 to 18.7	0.00 to 0.06	3.27 to 3.73	187 to 281×10³	13.8 to 25.3×10³	40.0 to 48.1×10⁶	10.8 to 17.1×10³	22.5 to 41.0×10⁶	Poor	0.2 to 3.1×10⁻⁴	0.1 to 4.9×10⁻⁴
18:5:1	1,675 to 1,699	1,575	15.8	.01	3.34	276	24.1		16.0	41.0	do	0.4	0.1
6:1:2	1,500 to 1,575	1,560	17.6	.06	3.41	277	25.3		14.6	39.4	do	1.4	ca. 1.5
3:2:1	1,575 to 1,675	1,575	15.2	.00	3.52	281	20.5		13.5	35.1	do	0.2	0.2
1:1:1	1,575 to 1,675	1,575	15.8	.02	3.67	234	16.4	41.8	17.1	35.5	do	No plastic flow	No plastic flow

correlate the expansions of the porcelains reported with the expansions of the primary phases for the fields in which these compositions are located.

From the phase relations existing in the system beryllia-alumina-titania (figs. 5 and 6), it can be seen why an aluminum titanate-beryllia porcelain of outstanding thermal-shock resistance cannot be developed. A study of the diagram shows that an addition of beryllia to aluminum titanante, and at the expense of the aluminum titanate, forms chrysoberyl, which is noted for its high expansivity, very coarse crystallization, and rather low strength. A similar examination shows also that no free beryllia, for thermal-conductivity benefits, could be available until more than about 20 weight percent of beryllia had been added, and that before that percentage had been reached no low-expansivity aluminum titanate can be formed.

5. Summary

The system beryllia-titania contains no compounds, a single eutectic exists at about 85 weight percent of TiO_2 and 1,670° ±3° C, and a narrow region of mixed crystals (an area of solid solution), as indicated by the melting behavior of various mixtures, extends from just beyond the eutectic to the melting point of pure titania.

Three eutectics in the system beryllia-alumina were found to be at: (1) 1,890° ±10° C and about mole ratio $1BeO:4Al_2O_3$, (2) 1,850° ±10° C and about mole ratio $2BeO:3Al_2O_3$, and (3) 1,835°±10° C and about 75 weight percent of alumina. The melting point of the recently reported compound $BeO.3Al_2O_3$ was found to be congruent at 1,910° ±10° C, and that of chrysoberyl ($BeO.Al_2O_3$) was redetermined at 1,870° ±10° C.

In the system alumina-titania, it is probable that the compound $Al_2O_3.TiO_2$ possesses two forms. The alpha, or high-temperature, form is stable from the alpha-beta inversion temperature of 1,820° ±10° C to its congruent melting point of 1,860° ±10° C. The beta, or low-temperature, form seems to be stable for periods up to 100 hr from room temperature to about 750° C and from about 1,300° C to its inversion temperature. One eutectic at 1,705° ±5° C and about 20 weight percent of alumina and one at 1,840° ±10° C and about mole ratio $5Al_2O_3.4TiO_2$ were found in the system. There is some doubt as to whether the alpha aluminum titanate melts congruently or incongruently, but the majority of the data indicate that the melting is congruent.

Although aluminum titanate exhibits low linear thermal expansion, only friable, very low-strength bodies can be made by using the pure component oxides with no other additions. When such a body is used at temperatures between about 750° and 1,300° C, a gradual increase in the expansivity can be expected, which can be traced to the decomposition of the aluminum titanate into its constituent oxides.

Three invariant points are indicated in the system beryllia-alumina-titania: (1) 1,572° ±5° C and about mole ratio $2BeO:1Al_2O_3:2TiO_2$, (2) 1,577°

$\pm 5°$ C and about mole ratio $2BeO:1Al_2O_3:4TiO_2$, and (3) 1,580° $\pm 5°$ C and about mole ratio $1BeO:1Al_2O_3:1TiO_2$. It is probable that another invariant point is located at about 1,755° $\pm 10°$ C and about mole ratio $2BeO:5Al_2O_3:2TiO_2$. These invariant points were located in that area of the triaxial diagram representing mixtures containing less than 18 weight percent of beryllia.

Early in the development of the beryllia-alumina-titania refractory porcelains and after the investigation of the phase relations existing in the ternary system, it was evident that any attempt to combine the high thermal conductivity of beryllia with the low expansivity of the compound aluminum titanate could not be successful. However, a number of relatively high-strength high-temperature porcelains were developed. They may be of use in applications where thermal-shock resistance is not of prime importance. The range of values for the general physical properties of practically impervious porcelains of this system were found to be: maturing range, usually 1,525° to 1,575° C, but with some of the high-alumina-containing bodies maturing between 1,600° and 1,700° C; apparent density, 3.3 to 3.7 g/cm^3; shrinkage, 11 to 19 percent; room-temperature compressive strength, 187,000 to 280,000 lb/in.^{2}; room-temperature transverse strength, 13,700 to 25,000 lb/in.^{2}; Young's modulus at room temperature, 42,000,000 to 47,000,000 lb/in.^{2}; transverse strength at 1,800° F (982°), 10,500 to 17,000 lb/in.^{2}; approximate Young's modulus at 1,800° F, 22,000,000 to 41,000,000 lb/in.^{2}; relative thermal-shock resistance, poor; and, the linear thermal expansion of a few selected bodies, in the range 25° to 950° C, usually was regular and ranged from 0.81 to 0.89 percent.

The authors acknowledge the assistance of Howard E. Swanson and Barbara Sullivan in the preparation and interpretation of the X-ray powder diffraction patterns and for the differential thermal analyses.

6. References

[1] R. F. Geller and P. J. Yavorsky, J. Research NBS 34, 395 (1945) RP1649.
[2] R. F. Geller, P. J. Yavorsky, B. L. Steierman, and A. S. Creamer, J. Research NBS **36,** 277 (1946) RP1703.
[3] S. M. Lang, L. H. Maxwell, and R. F. Geller, J. Research NBS **43,** 429 (1949) RP2034.
[4] S. M. Lang, L. H. Maxwell, and M. D. Burdick, J. Research NBS **45,** 366 (1950) RP2147.
[5] S. M. Lang and R. F. Geller, J. Am. Ceram. Soc. 34, 193 (1951).
[6] F. B. Hornibrook, Am. Soc. Testing Materials Bul. No. 101, p. 5 (Dec. 1939); and Gerald Pickett, Am. Soc. Testing Materials Proc. **45** (1945).
[7] H. von Wartenburg, H. J. Reusch, and E. Saran, Z. anorg. allgem. Chem. **230,** 257 (1937).
[8] E. C. Henry, Pennsylvania State College, Quarterly Progress Report, Memorandum Report No. 19 (Feb. 15, 1949).
[9] H. von Wartenburg and H. J. Reusch, Z. anorg. allgem. Chem. **207,** 1 (1932).
[10] W. R. Foster and H. F. Royal, J. Am. Ceram. Soc. **32,** 26 (1949).
[11] E. N. Bunting, BS J. Research **11,** 725 (1933) RP619.
[12] Private communication from F. Hummell, Pennsylvania State College, State College, Pa. (1949).
[13] M. Hamelin, Bul. Ceram. Soc. (France) **11,** 14 (1951).
[14] The system beryllia-alumina-titania: Phase relations and general physical properties of three-component porcelains, S. M. Lang, C. L. Fillmore, and L. H. Maxwell, Final Report to Office of Naval Research, ONR Project NR 032-074, Contract NA ori 2-47, Code N-423 (March 30, 1951). Not available for general distribution.

Washington, November 23, 1951.

UNIVERSITY OF MICHIGAN LIBRARIES

Journal of Research of the National Bureau of Standards Vol. 48, No. 4, April 1952 Research Paper 2317

Effect of Temperature on the Tensile Properties of High-Purity Nickel

William D. Jenkins and Thomas G. Digges

Tension tests were made at temperatures ranging from −320° to 1,500° F on high-purity nickel in the annealed condition. Exceptions to the usual trend exhibited by metals of decreasing strength and increasing ductility with increasing test temperature were observed and discussed. Strain aging occurred in specimens tested in the temperature range of about 80° to 300° F, but recrystallization and recovery predominated in specimens fractured at 1,200° and 1,500° F.

1. Introduction

The tests described in this paper are a part of a comprehensive investigation to evaluate the rheological behavior, tensile and creep properties of high-purity nickel, high-purity copper, and alloys of these two metals. The relatively low range in temperature at which creep may occur in these metals, the unlimited solid solubility of the two metals in each other, the availability of commercial metals of very high-purity, and the wide industrial applications of both the metals and alloys make this binary system an attractive one for use in this study.

The results of creep tests at 110°, 250°, and 300° F on high-purity (OFHC) copper and of short-time tensile tests at temperatures ranging from −320° to +212° F on the copper, nickel, and copper-nickel alloys initially as annealed were presented in previous publications.[1, 2, 3] Additional short-time tensile tests were made at temperatures ranging from room to 1,500° F on the same lot of annealed high-purity nickel,[4] and the results of the present and previous tests on the nickel are contained in the present paper.

2. Material and Test Procedures

The specimens used in making the tension tests were prepared from two bars from the same heat containing 99.85 percent of Ni, 0.009 percent of Cu, 0.04 percent of Fe, 0.03 percent of Mn, 0.11 percent of Si, 0.007 percent of C, 0.002 percent of S, 0.002 percent of O, 0.001 percent of N, and 0.002 percent of H as determined by chemical, spectrochemical, and vacuum fusion analyses. The bars were hot-worked to 1 1/16-in. diameter and subsequently annealed during manufacture for an average grain diameter of 0.045 mm.

In one series of tensile tests made at temperatures ranging from room temperature to 1,500° F, the specimens were 6½ in. long, with a reduced section of 0.505-in. diameter for a 2-in. gage length. The shoulder fillets were of ¼ in. radius, and the ends were machined with ¾ in.×10 threads. The reduced section of each specimen was finished by grinding and then polishing in the axial direction, using No. 400 Aloxite metallographic polishing paper. Each specimen was heated in an electric furnace to the desired temperature (above room) and held at temperature for a minimum of 3 hours before being tested. The specimen was maintained within ±3° F of the desired temperature, and the gradient over the gage length did not exceed 5° F during the period of testing. The specimens were tested in a hydraulic type machine (15,000-lb range) with the specimen and holders occupying about 3 ft between two self-alining grips. The movement of the head of the machine during the testing was recorded by means of a stress-strain recorder of the Templin type. The loading was controlled to produce a rate of extension of about 1 percent per minute; a rate of the same order of magnitude as that used in the previous series of tests. All the specimens used in the above series of tests were prepared from the same bar, but this was not the same bar as that used for the specimens tested at subzero temperatures.

The preparation of the specimens and the testing procedure used in other series of tests made at temperatures ranging from −320° to +212° F are described in detail in a previous report (see footnote[3]). Essentially, the specimens were 0.505 in. in diameter, with a 2-in. gage length, and they were fully immersed during the testing in tension at a controlled rate of loading to produce a contraction of approximately 1-percent reduction of area per minute. The change in minimum diameter of the specimen during the testing was measured by a special reduction of area gage; for the tests made at room temperature no liquid bath was used, and the diameter measurements were made with a micrometer. All the tensile specimens used in this series were prepared from the same bar.

One specimen was tested in tension at each selected temperature, except that two specimens (one of each series) were tested at room temperature and two at 212° F.

Rockwell B hardness (100-kg load, 1/8-in.-diameter ball) tests were made at room temperature on the

[1] W. D. Jenkins and T. G. Digges, Creep of high-purity copper, J. Research NBS 45, 153 (1950) RP2121.
[2] W. D. Jenkins and T. G. Digges, Creep of annealed and cold-drawn high-purity copper, J. Research NBS 47, 272 (1951) RP2254.
[3] G. W. Geil and N. L. Carwile, Tensile properties of copper, nickel and some copper-nickel alloys at low temperatures, NBS symposium on mechanical properties of metals at low temperatures, NBS Circular 520 (1952).
[4] The high-purity nickel was prepared specially for the National Bureau of Standards by the International Nickel Co. through the cooperation of W. A. Mudge.

specimens prepared from the annealed bars and on the tensile specimens after fracturing at temperatures ranging from 88° to 1,500° F. Two flats, 180° apart, were prepared parallel to the longitudinal axis of the fractured specimens, and the Rockwell readings were made at various points along the center line of these flats; the specimens were about 0.2 in. thick. The diameters of the specimen at the points of indentation were accurately determined to correlate the degree of plastic deformation with the hardness values.

The usual procedures were followed in preparing specimens by mechanical methods for metallography and in carrying out the metallographic examination.

3. Results and Discussion

3.1. Stress-Strain Curves

The stress-strain record obtained in testing specimens in tension at temperatures ranging from 88° to 1,500° F is given in figure 1. No definite yield point (drop of beam) is evident in any of these curves; furthermore, no yield point was observed in any of the specimens tested at subzero temperatures. Although a comparison of the relative height and width of these curves indicates the effects of temperature on the stress and ductility, respectively, of the initially annealed high-purity nickel, the influence of temperature on these properties is more clearly shown by the results summarized in figures 2 to 10.

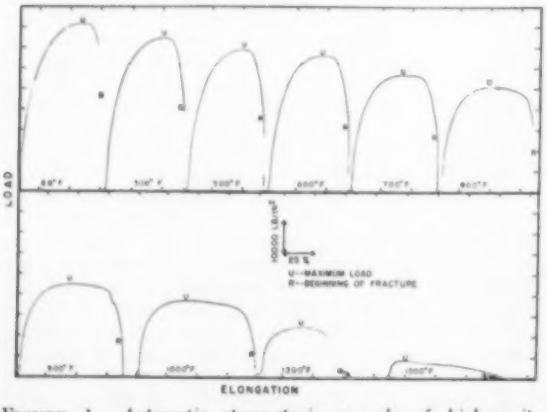

FIGURE 1. *Automatic stress-strain records of high-purity nickel specimens tested in tension at different temperatures.*

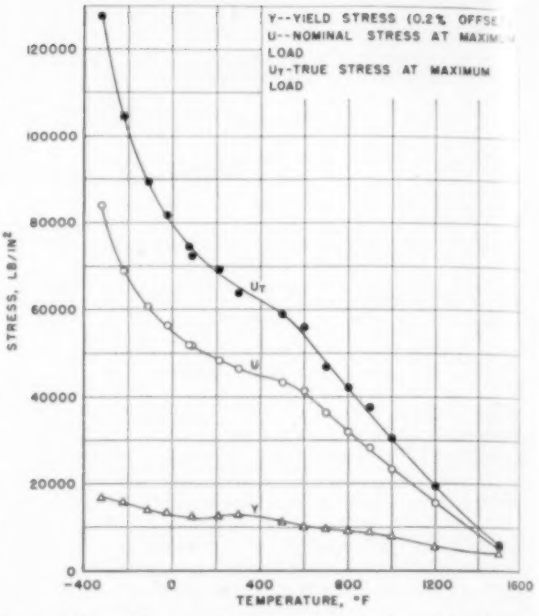

FIGURE 2. *Influence of temperature on the yield strength, tensile strength, and true stress at maximum load of high-purity nickel.*

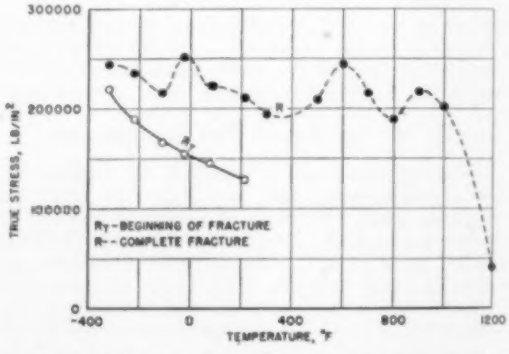

FIGURE 3. *Influence of temperature on the true stresses at the beginning and at complete fracture of high-purity nickel specimens tested in tension.*

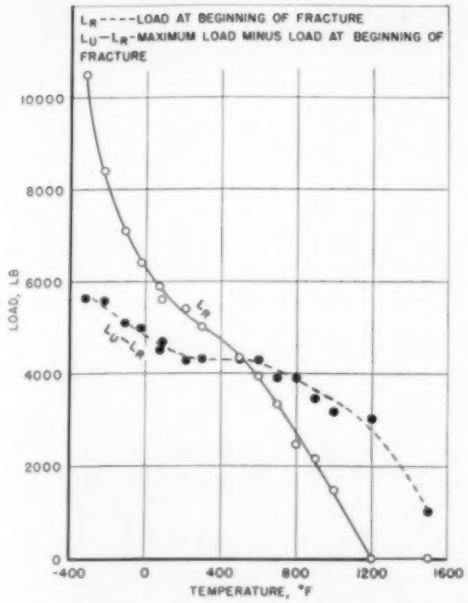

FIGURE 4. *Effect of temperature on the loads at fracture and loads corresponding to the difference between the maximum load and the load at fracture.*

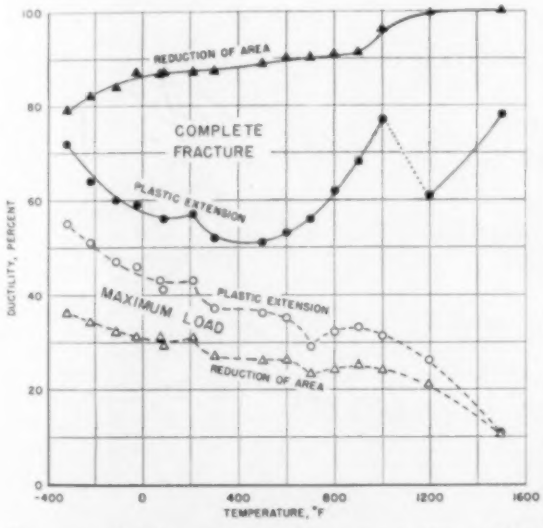

FIGURE 5. *Relation of temperature to the ductility of high-purity nickel specimens fractured in tension.*

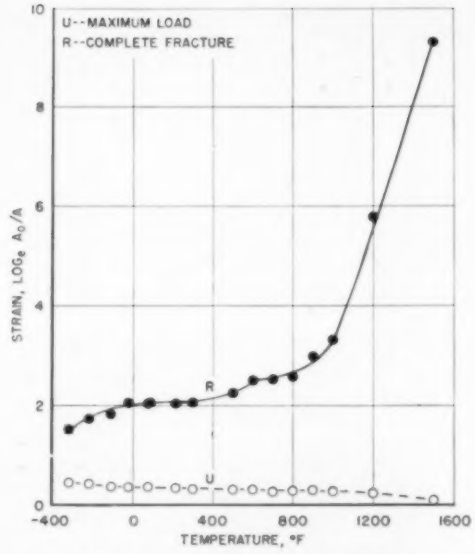

FIGURE 6. *Effect of temperature on the true strain at maximum load and at fracture of high-purity nickel specimens tested in tension.*

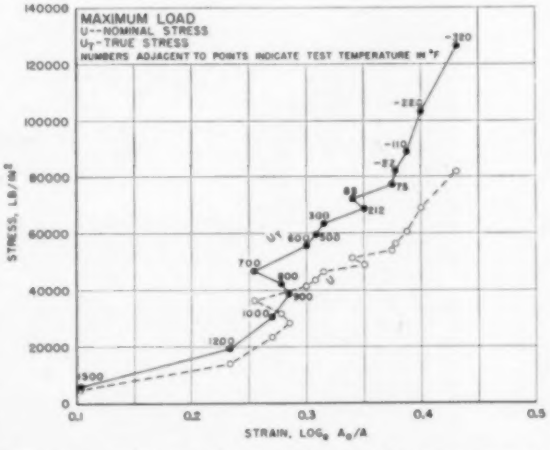

FIGURE 7. *Relation of the nominal and of the true stresses at maximum load to true strain of high-purity nickel specimens fractured in tension at different temperatures.*

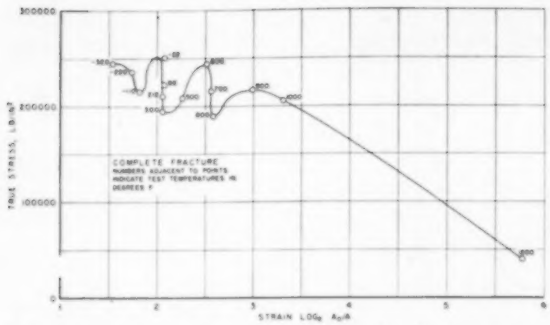

FIGURE 8. *Relation of true stress at complete fracture to true strain of high-purity nickel specimens tested in tension at different temperatures.*

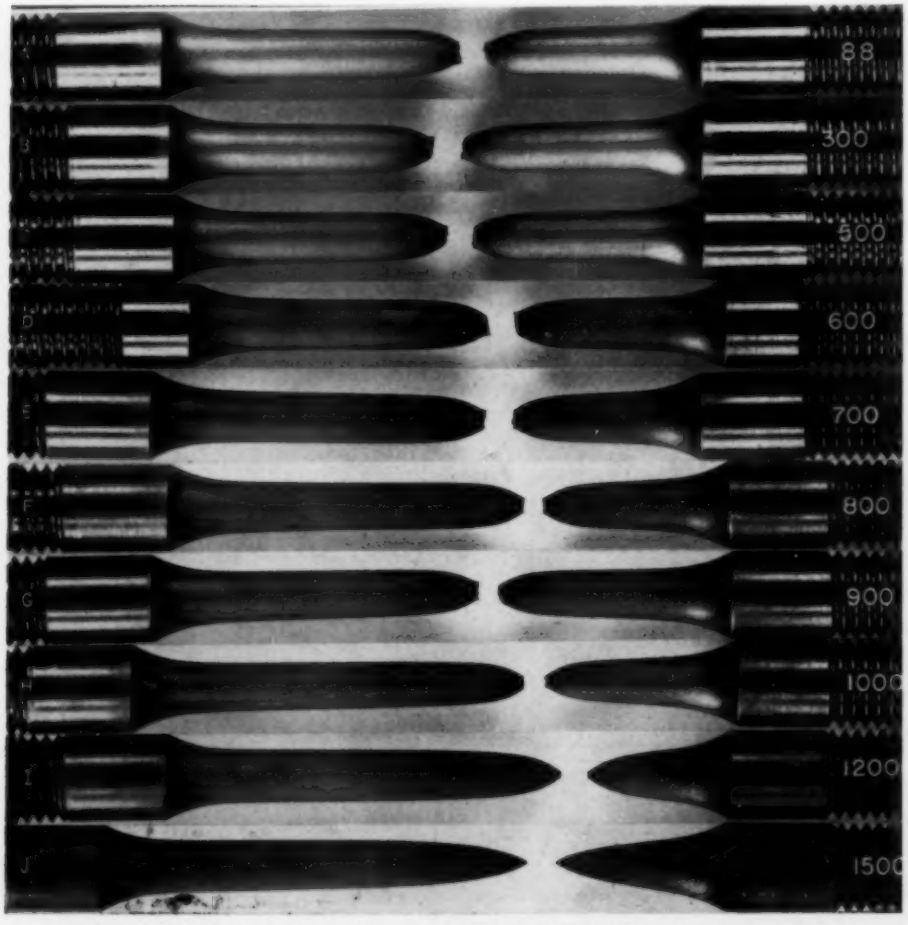

FIGURE 9. *High-purity nickel specimens fractured in tension at different temperatures.* × .75.
A, 88° F; B, 300° F; C, 500° F; D, 600° F; E, 700° F; F, 800° F; G, 900° F; H, 1,000° F; I, 1,200° F; J, 1,500° F.

UNIVERSITY OF MICHIGAN LIBRARIES

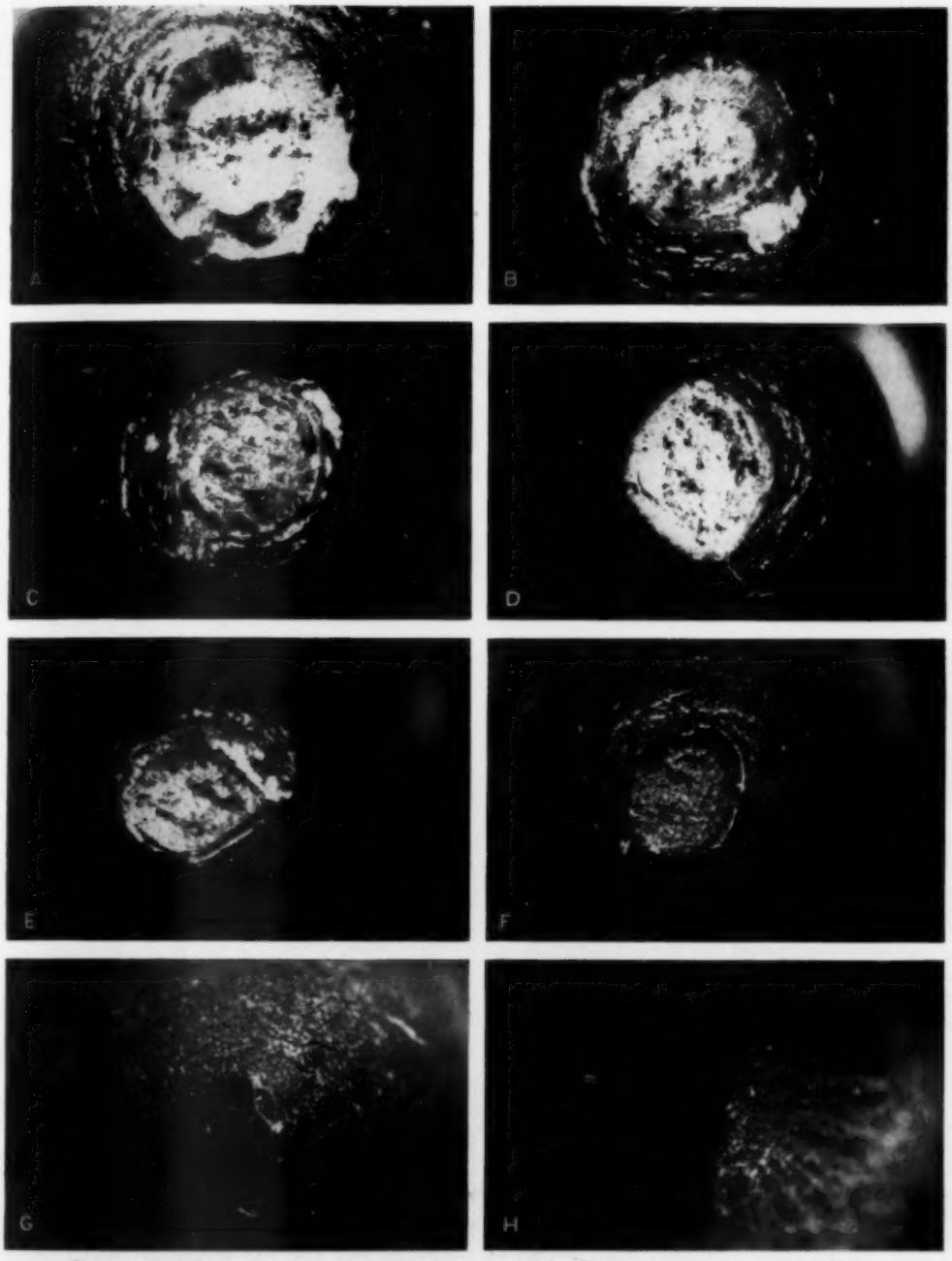

FIGURE 10. *Fractured cross sections of high-purity nickel specimens tested in tension at different temperatures.* × 7.

A, 88°F; B, 600° F; C, 700° F; D, 800° F; E, 900° F; F, 1,000° F; G, 1,200° F; H, 1,500° F.

3.2. Effect of Temperature on Strength

Both the true stress [5] and the nominal stress [6] at maximum load (tensile strength) decreased rapidly as the temperature was increased from −320° F to room and less rapidly with further increase in temperature to about 500° F (fig. 2); thereafter, both curves (U_T and U) again showed a rapid decrease as the temperature of testing was increased up to 1,500° F. The general trend for the yield strength (curve Y) to decrease with an increase in test temperature was reversed when the temperature was within the range of about 80° to 300° F. As the temperature was increased from 80° to about 300° F, the yield strength-temperature curve sloped upward before again descending with a further increase in temperature. As is to be expected, all three of the curves representing strength-temperature relations approached a common value at the highest test temperature of 1,500° F.

Reversals are also evident in the slope of the curve of the true stress at complete fracture versus temperature (fig. 3, curve R). However, the fracture values were within the range of about 250,000 to 190,000 psi for test temperatures from −320° to +1,000° F. There was a considerable drop in the strength at complete fracture when the test temperature was increased from 1,000° to 1,200° F.

The evidence indicates that fracture commenced at or near the longitudinal axis of each specimen (see footnote 1) and then progressed outward to the surface accompanied by appreciable "necking". Due to the "rim effect" the stress at complete fracture, therefore, is considerably higher than the corresponding stress at start of fracture. The rim effect and degree of necking varied with the test temperature (see photographs of fractured specimens given in figs. 9 and 10). The true stress at the beginning of fracture was determined only for temperatures ranging from −320° to +212° F. The results (fig. 3, curve R_T) show that the strength decreased continuously with an increase in temperature.

The load on the specimen at the beginning of fracture decreased continuously as the temperature increased (fig. 4, curve L_R). It is of interest to note that the load approached zero in value for the specimens tested at 1,200° and 1,500° F. This means that each of these two specimens necked down to nearly a point before fracturing (figs. 9, *I* and *J*; fig. 10, *G* and *H*). An indication of this tendency to neck, and the accompanying work-hardening and recovery characteristic for the region of plastic deformation extending from that corresponding to the maximum load to the beginning of fracture as affected by temperature is given by the course of the curve $L_U - L_R$ in figure 4. Except for the nearly horizontal position of this curve for temperatures within the range from about 212° to 600° F, the loads decreased continuously as the temperature increased.

[5] The value for true stress is based upon the current cross-sectional area of the specimen.

[6] The value for nominal stress is based upon the original cross-sectional area of the specimen.

3.3. Effect of Temperature on Ductility

The general trend was for both the plastic extension and reduction of area at maximum load to decrease with increase in temperature (fig. 5). However, definite breaks in the downward trend are evident in the curves as the temperature of testing was increased from about 80° to 212° F and from about 600° to 700° F. In the former range the ductility increased with increase in temperature, whereas in the latter this effect was reversed.

The plastic extension at complete fracture-temperature curve also showed a decided break in its downward slope as the temperature increased from 80° to 212° F. The extension attained the minimum value at about 500° F. Thereafter, the extension increased with test temperature up to about 1,000° F, dropped markedly as the temperature was increased to 1,200° F, and then again increased with the temperature. The course of the curve of reduction of area at fracture versus temperature shows that the reduction of area increased relatively rapidly as the temperature increased from about −320° to 80° F and from 900° to 1,200° F. At test temperatures between these two ranges, the reduction of area increased only slightly with an increase in temperature. The reduction of area at 1,200° and 1,500° F attained a value of nearly 100 percent. A noteworthy feature is the high ductility in tension of nickel at test temperatures ranging from −320° F (liquid nitrogen) to +1,500° F. The high ductility at low temperatures is characteristic of face-centered cubic metals, such as nickel and copper.

The curve of true strain [7] at maximum load versus temperature (U, fig. 6) shows a continuous slightly downward course as the test temperature is increased from −320° to +1,500° F. The curve, R, representing the relation between true strain at complete fracture and test temperature indicates deviation from the steady upward trend occurring at temperatures of about 0° to 300° F and 500° to 700° F; the conditions are similar to those already described for plastic extension and reduction of area-temperature curves of figure 5.

3.4. Relation of Strength to True Strain

The relation between both the nominal stress and true stress at maximum load and the true strain as affected by temperature is shown by the curves U and U_T, respectively, in figure 7. The two curves are somewhat similar in shape, and discontinuities are evident for values of strains within the ranges of about 0.25 to 0.3 and 0.32 to 0.37. Irregularities are also observed in the course of the curve of true stress at fracture versus true strain (fig. 8). The form of this curve is affected by the variations in the degree of necking and the rim formation accompanying deformation from beginning to complete fracture (figs. 9 and 10) of the specimens tested at the different

[7] True strain is defined as the natural logarithm of the ratio of the initial cross-sectional area (A_0) of the specimen to its current cross-sectional area (A).

UNIVERSITY OF MICHIGAN LIBRARIES

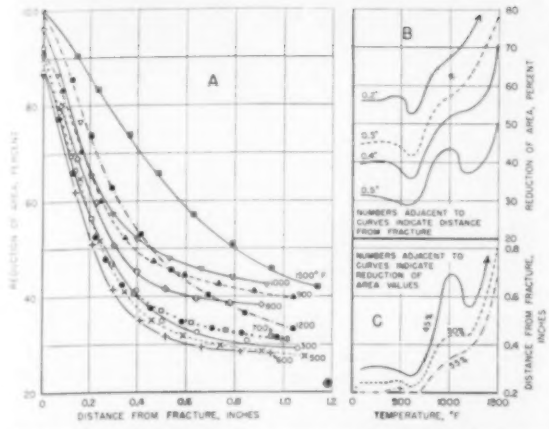

FIGURE 11. *Effect of test temperature on the necking characteristic of high-purity nickel specimens fractured in tension.*

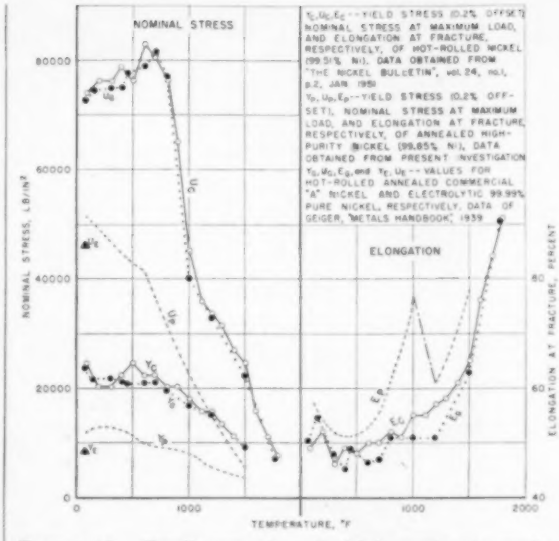

FIGURE 12. *Tensile properties of nickel, varying in purity, as affected by temperature.*

test temperatures. In the plastic deformation range from maximum load to complete fracture, all the specimens contracted locally, but the contour of the neck varied with the temperature (fig. 11). In certain specimens (600° F), the necking was confined principally to the region of complete fracture, whereas other specimens (1,500° F) contracted more uniformly throughout the entire gage length.

An indication of the reproducibility of the strength and ductility values at room temperature and at +212° F for the two bars processed alike from the same heat is given by the results summarized in table 1. Although the two series of tests were made at different times, by different operators, and the specimens were prepared from different bars (*B* and *C*), the respective values for strength and ductility agreed closely.

Some of the irregularities observed in the temperature-tensile-properties curves can be partly attributed to metallurgical changes in the nickel. Strain aging occurred in the specimens tested in the temperature range of about 80° to 300° F and attained a maximum in the upper part of this range. The temperature and degree of strain aging are affected by the strain rate and by the purity of the nickel (fig. 12). A change in the magnetic properties of high-purity nickel (Curie point) occurs at a temperature of about 665° F.[8] The present results also show certain distinct and abnormal changes in some tensile properties of specimens tested in the temperature range of about 500° to 700° F. This range is appreciably below that of recrystallization, and an examination of the microstructure of specimens fractured at 1,000° F or below showed no evidence of recovery (fig. 13, *A*, *B*, *C*, and *D*); the hardness test made on the specimen after fracturing at 1,000° F indicated that some recovery (softening) occurred at this temperature (fig. 14). However, recrystallization was evident in the specimen tested at 1,200° F (fig. 13, *E*), and recrystallization and some grain growth occurred in the specimen fractured at 1,500° F (fig. 13, *F*). Some twins are evident in the recrystallized structure of the specimen tested at 1,500° F.

[8] E. M. Wise, Properties of nickel and nickel alloys, Metals Handbook, p. 1046 (1948).

TABLE 1. *Tensile properties at room temperature and 212° F of the two bars of high-purity nickel used*

Bar designation	Temperature of test	Yield strength [a]	Tensile strength	Maximum load			Fracture				
							Beginning		Complete		
				True stress	Extension	Reduction of area	True stress	Reduction of area	True stress	Extension	Reduction of area
	°F	1,000 lb/in.²	1,000 lb/in.²	1,000 lb/in.²	%	%	1,000 lb/in.²	%	1,000 lb/in.²	%	%
B	75	12.5	52.7	76.7	45	31	145.5	79	278.6	56	89
C	88	12.5	51.6	72.3	41	29	145.3	80	222.8	56	87
B	212	12.5	48.4	69.2	43	31	128.1	79	210.6	57	87
C	212	12.0	48.3	68.5	42	30	130.0	79	224.2	57	88

[a] 0.2 % offset.

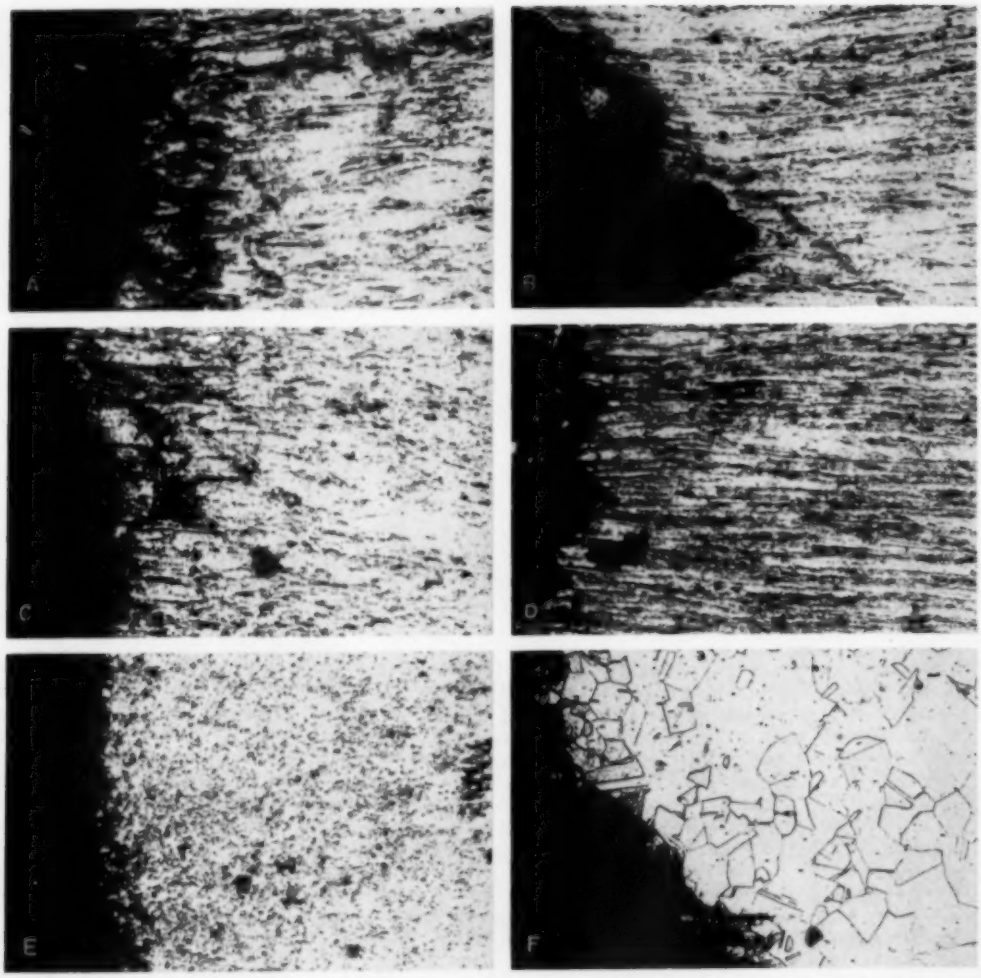

FIGURE 13. *Structure at fracture of high-purity nickel specimens tested in tension at different temperatures*

Longitudinal section near axis of specimens. (Etched with 6 parts nitric (concentrated), 4 parts glacial acetic acids). × 100. A, 88° F; B, 600° F; C, 800° F; D, 1,000° F; E, 1,200° F; F, 1,500° F.

3.5. Relation of Plastic Deformation to Hardness

The effect of plastic deformation and recovery at different temperatures on hardness at room temperature of the fractured specimens is given by the results plotted in figures 14 and 15. The general trend was for the hardness at room temperature to decrease slightly with increase in distance from the fracture (decrease in reduction of area) for each specimen fractured in the range of 88° to 1,000° F. The hardness measurements indicate that the work-hardening and recovery characteristics were quite similar for specimens tested in the range from 88° to 700° F, and the degrees of recovery increased (hardness decreased) with increase in test temperature from 800° to 1,000° F. Appreciable recovery occurred in the specimens tested at 1,200° and 1,500° F. This is to be expected, because, as previously pointed out, both temperatures are sufficiently high for recrystallization of the plastically deformed metal. The lower hardness values for the specimen tested at 1,500° F can be attributed to the higher degree of recovery and increase in grain size. The hardness of the specimen fractured at 1,500° F decreased with an increase in plastic deformation or with decrease in distance from the fracture end. Furthermore, the hardness, measured at room temperature, of the specimen fractured at 1,200° F did not materially change over the gage length corresponding to a range in reduction of area from 35 to 75 percent

UNIVERSITY OF MICHIGAN LIBRARIES

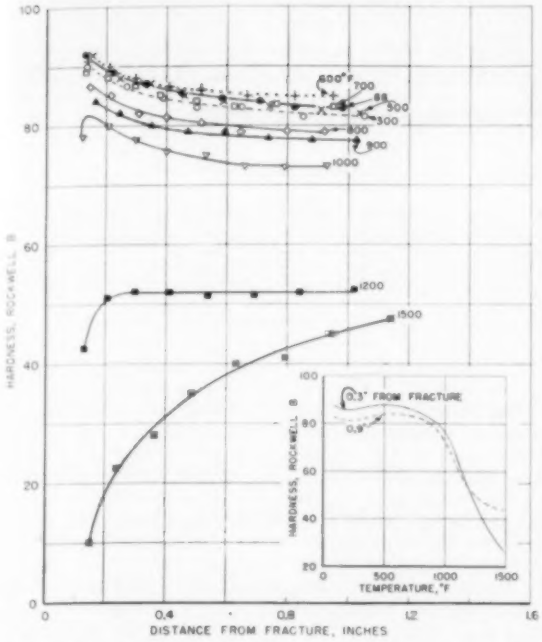

FIGURE 14. *Relation of hardness at room temperature to distance from fracture of high-purity nickel specimens tested in tension at different temperatures.*

Hardness of the annealed nickel before testing in tension was Rockwell B 32.

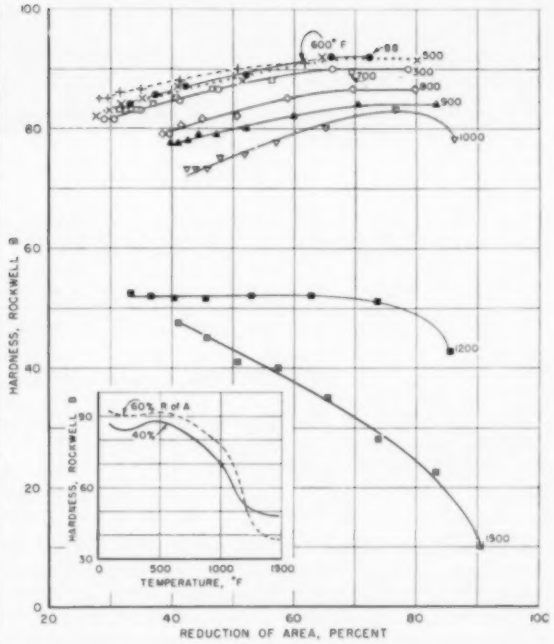

FIGURE 15. *Effect of deforming high-purity nickel in tension at different temperatures on the hardness at room temperature.*

Hardness of the annealed nickel before testing in tension was Rockwell B 32.

(1.0 to 0.2 in., respectively, from fracture end). The hardness of this plastically deformed specimen (Rockwell B 52), however, was appreciably higher than that of the annealed nickel (Rockwell B 32). Hardness induced by plastic deformation was even evident in a part of the recrystallized specimen that was deformed at 1,500° F. However, above 65-percent reduction of area its hardness was either equivalent to or below that of the originally annealed nickel.

4. Summary

Tensile tests were made at temperatures ranging from −320° to +1,500° F on specimens containing 99.85 percent of nickel in the annealed condition. The results are summarized in the figures given in the report.

The general trends were for the yield and tensile strengths and the ductility at maximum load to decrease, and the reduction of area (at complete fracture) to increase with an increase in test temperature. The elongation at complete fracture attained a minimum at about 500° F. However, irregularities were observed in the usual trends of some of the tensile properties-temperature relations at test temperatures in the ranges of about 80° to 300° F and 500° to 700° F. The evidence indicated that strain aging occurred in the range 80° to 300° F and that recrystallization and recovery predominated in specimens fractured at 1,200° or 1,500° F.

The authors gratefully acknowledge the assistance of C. R. Johnson and J. H. Darr in making the tension tests at elevated temperatures and of G. W. Geil and N. L. Carwile in making the tests at sub-zero temperatures.

WASHINGTON, February 5, 1952.

Journal of Research of the National Bureau of Standards Vol. 48, No. 4, April 1952 Research Paper 2

Thiophosphation of 2-Methyl-2-Nitro-1-Propanol and the Preparation of Monothiophosphoric Acid

J. V. Karabinos, R. A. Paulson, and W. H. Smith

The thiophosphation of a nitroalcohol was studied in ether and in pyridine solution. When 2-methyl-2-nitro-1-propanol was refluxed with phosphorus pentasulfide in ether, the corresponding dithiophosphate was formed. In pyridine solution, however, a pyridine salt of the secondary dithiophosphate was formed. A pyridine salt of metatrithiophosphoric acid was also isolated from the latter reaction, and this salt was hydrolyzed to pyridinium monothiophosphate. Monothiophosphoric acid monohydrate itself was obtained, for the first time, by application of ion-exchange and lyophilizing techniques to its pyridine salt.

1. Introduction

The reaction of phosphorus pentasulfide with organic hydroxy compounds reportedly [1 to 4][1] yields secondary dithiophosphates (I).

$$(RO)_2P(S)SH. \qquad (I)$$

An extension of this reaction to a nitroalcohol is described. When 2-methyl-2-nitro-1-propanol was refluxed with phosphorus pentasulfide in ethyl ether, a product melting at 104° C was obtained that gave elemental analyses and a molecular-weight value corresponding to O,O′-bis(2-methyl-2-nitro-propyl-) dithiophosphate (II).

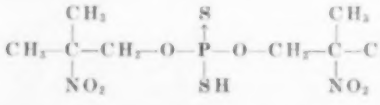

(II)

Phosphorus pentasulfide in pyridine solution has been recently reported [5] to give thiation of certain pyridones. In a study of the action of phosphorus pentasulfide on 2-methyl-2-nitro-1-propanol in pyridine solution at the Bureau, a yellow, extremely hygroscopic substance crystallized directly from the pyridine solution; this substance gave elemental analyses corresponding to $C_{10}H_{11}N_2PS_3$ (III). Upon standing exposed to the atmosphere, substance III took up moisture with considerable foaming and evolution of hydrogen sulfide and, in a relatively short time, a colorless solution was obtained, from which white cube-like crystals appeared. After purification, the latter substance (IV) gave analyses corresponding to $C_5H_8O_5NSP$. Substance IV liberated pyridine under alkaline conditions, and hydrogen sulfide with dilute acids. A positive sulfhydryl test was given by III, although not by IV. Substances III and IV are probably pyridinium salts, the former a salt of pyridine with metatrithiosphoric acid, HPS_3, a thioanalog of metaphosphoric acid, and the latter a pyridine salt of monothiophosphoric acid, H_3PSO_3. This latter acid, a monothio analog of phosphoric acid, could arise from HPS_3 by hydrolysis, with the liberation of hydrogen sulfide.

$$HPS_3 + 3H_2O \rightarrow H_3PSO_3 + 2H_2S.$$

The formulas for the pyridinium salts III and IV may be represented as follows:

$$(C_5H_5N)_2{\cdot}HPS_3. \quad (III). \qquad C_5H_5N{\cdot}H_3PSO_3. \quad (IV)$$

It is possible that substance III, rather than phosphorus pentasulfide, acts as the thiating agent in pyridine solution [5].

From the mother liquors obtained by the reaction of phosphorus pentasulfide with the nitroalcohol in pyridine solution, still another crystalline substance was obtained; this substance melted at 103° to 104° C and gave analyses corresponding to the formula $C_{13}H_{22}O_6N_2S_2P$ (V). As pyridine was obtained upon the addition of alkali to V and hydrogen sulfide was liberated in acidic solution, V was suspected of being a pyridinium salt of O,O′-bis(2-methyl-2-nitro-propyl-)dithiophosphoric acid.

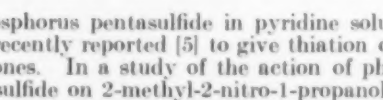

(V)

This was confirmed by the isolation of the secondary dithiophosphate (II) from the eluate upon removal of pyridine with a cation exchange resin.

The over-all equations for the action of phosphorus pentasulfide on 2-methyl-2-nitro-1-propanol in pyridine solution may be expressed as follows:

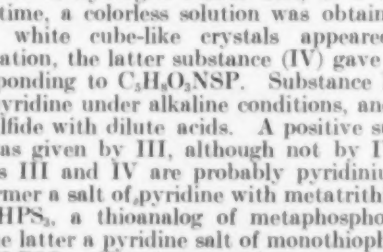

$(C_5H_5N)_2{\cdot}HPS_3$.

In a similar manner monothiophosphoric acid, H_3PSO_3, was isolated from its pyridinium salt (IV) by removal of the pyridine with the cation exchange resin, Amberlite IR-100-H, followed by lyophilization

[1] Figures in brackets indicate the literature references at the end of this paper.

UNIVERSITY OF MICHIGAN LIBRARIES

freeze-drying") of the eluate. The sirupy product gave sulfur and phosphorus analyses and a neutralization equivalent corresponding to a monohydrate, which was relatively stable at −20° C, although it decomposed slowly at room temperature, as reported in the early literature [6].

2. Experimental Details

2.1. Reaction of 2-Methyl-2-Nitro-1-Propanol with Phosphorus Pentasulfide in Ethyl Ether

O,O′-Bis(2-methyl-2-nitro-propyl-)Dithiophosphate (II)

To 30 g of 2-methyl-2-nitro-1-propanol dissolved in 150 ml of ethyl ether was added 30 g of phosphorus pentasulfide, and the mixture was maintained at reflux for 16 hrs. The white, fluffy needles that had formed in good yield were collected by filtration and dried in a vacuum desiccator. After several recrystallizations from ether, a product with a constant melting point of 103.8° to 104° C was obtained. The substance, unlike the original nitroalcohol, was insoluble in water, and purification could also be effected by aqueous extraction.

Analysis: Calculated for $C_8H_{17}O_6N_2S_2P$: C, 28.91; H, 5.16; S, 19.29; P, 9.32; Molecular Weight, 332. *Found:* C, 29.01; H, 5.10; S, 19.70; P, 9.26; molecular Weight (Rast), 322.

2.2. Reaction of 2-Methyl-2-Nitro-1-Propanol with Phosphorus Pentasulfide in Pyridine

a. Pyridine Salt of Metatrithiophosphoric Acid

Phosphorus pentasulfide (25 g) was dissolved in 150 ml of pyridine containing 12 g of 2-methyl-2-nitro-1-propanol, and the mixture was refluxed for 1½ hrs. Upon cooling the solution, yellow prisms began crystallizing; the process was allowed to continue overnight. The crystalline product was collected by filtration, washed with ethyl ether, and dried in a vacuum desiccator for several days. The weight of product (29 g) corresponded to a theoretical yield of 90 percent. The substance was stable in a desiccator but decomposed rapidly when exposed to atmospheric moisture. It gave a positive sulfhydryl test with nitroprusside reagent and melted in the neighborhood of 90° to 100° C, although the melting point was not at all well defined because of foaming and the hygroscopic character of the substance.

Analysis: Calculated for $C_{10}H_{11}N_2PS_3$: C, 41.94; H, 3.87; P, 10.82; S, 33.59. *Found:* C, 41.95; H, 3.71; P, 10.80; S, 33.70.

b. Pyridine Salt of O,O′-Bis (2-Methyl-2-Nitro-Propyl-) Dithiophosphate (V)

The mother liquor from which the pyridine salt of Metatrithiophosphoric acid (III) was obtained was poured into 500 ml of water, and a small amount of precipitated sulfur was removed by filtration. The clear solution was then concentrated to a crystalline residue in a current of dry air, and the crystals were extracted with a small amount of water, collected by filtration, and dried. The crude pyridine salt of O,O′-bis(2-methyl-2-nitro-propyl-) dithiophosphate (V) weighing 15 g was purified for analyses by recrystallization from dioxane-ether (1:1) and finally from ethanol-ether (1:1); mp, 103° to 104° C.

Analysis: Calculated for $C_{13}H_{22}O_6N_3S_2P$: C, 37.95; H, 5.39; S, 15.58; P, 7.53. *Found:* C, 38.25; H, 5.40; S, 15.98; P, 7.55.

c. Isolation of O,O′-Bis (2-Methyl-2-Nitro-Propyl-) Dithiophosphate (II) From Its Pyridine Salt (V)

Five milliliters of an aqueous solution containing 0.5 g of the pyridine salt (V) was passed through a column (1.0 by 10 cm) of Amberlite IR–100–H, analytical grade, and a sufficient volume of distilled water was then passed through the column to elute the dithiophosphate. The eluate was concentrated in a current of dry air to a high yield of crystalline residue, which was purified by recrystallization from ethyl ether. The product melted sharply at 104° C and showed no melting-point depression upon admixture with the O,O′-bis(2-methyl-2-nitro-propyl-)dithiophosphate prepared in ether solution.

d. Hydrolysis of Pyridinium Metatrithiophosphate (III). Pyridine Salt of Monothiophosphoric Acid (IV)

Although hydrolysis of III could be effected by atmospheric moisture, 4.2 g of pyridinium metatrithiophosphate was dissolved in 3 ml of water. Vigorous evolution of gas occurred, and the odor of hydrogen sulfide was pronounced. After the solution had stood for 1 hr, the excess moisture was removed in a current of dry air, and the resultant sirup began to crystallize. Crystallization was hastened by addition of small amounts of ethanol. The cube-like crystals were collected by filtration and dried in vacuo. The product weighed 2 g, corresponding to 71 percent of the theoretical yield. The product was recrystallized from 95-percent ethanol for analysis. It did not give a sulfhydryl test, although it liberated pyridine on treatment with dilute alkali and hydrogen sulfide upon the addition of dilute acids. The purified pyridinium monothiophosphate melted at 116° C, with evolution of gas.

Analysis: Calculated for $C_5H_8O_3NPS$: C, 31.92; H, 4.17; P, 16.04; S, 16.60. *Found:* C, 31.95; H, 4.43; P, 15.92; S, 16.89.

2.3. Preparation of Monothiophosphoric Acid Monohydrate

A solution containing 1 g of pyridinium monothiophosphate in 3 ml of water was passed through a column (1.4 by 40 cm) of cation exchange resin, Amberlite IR–100–H, analytical grade, and a sufficient volume of distilled water was added to elute the free acid. The acidic portion of the effluent was collected in a flask, surrounded by an ice bath, and the cooled filtrate was lyophilized. A theoretical yield of thick, sirupy acid was obtained.

Although the acid was hygroscopic and had an odor resembling hydrogen sulfide, it was quite stable at −20° C, as indicated by the analysis corresponding to monothiophosphoric acid monohydrate.

Analysis: Calculated for $H_3PSO_3 \cdot H_2O$: S, 24.27; P, 23.46; N. E., 132. *Found:* S, 24.26; P, 22.93; N. E., 130, 129.

Monothiophosphoric acid monohydrate gave a sulfur analysis of 24.26 percent after standing at −20° C for 1 week and 24.23 percent after 2 weeks. However, when a sample was allowed to stand at 30° in a glass-stoppered vial, in a desiccator, the sulfur value decreased to 11.54 percent after 1 week, and the phosphorus value increased to 25.54 percent. These analyses, in addition to the pronounced odor of hydrogen sulfide, indicated that the acid was decomposing to phosphoric acid monohydrate and hydrogen sulfide, as reported in the early literature [6].

3. References

[1] P. S. Pischumuka, J. Russ. Phys. Chem. Soc. **44**, 1906 (1912); **56,** 11 (1925).
[2] I. Cambi, Chimica e industria (Italy) **26,** 97 (1944).
[3] L. Malatesta and R. Pizzotti, Chimica e industria (Milan) **27,** 6 (1945).
[4] G. M. Kosalapoff, Organophosphorus compounds, p. 236, 256 (John Wiley & Sons, Inc., New York, N. Y., 1950).
[5] E. Klingsberg and D. Papa, J. Am. Chem. Soc. **73,** 4988 (1951).
[6] C. A. Wurtz, Ann. chim. phys. **20,** 473 (1847); Compt. rend. **24,** 288 (1847).

WASHINGTON, January 2, 1952.

UNIVERSITY OF MICHIGAN LIBRARIES

...rnal of Research of the National Bureau of Standards Vol. 48, No. 4, April 1952 Research Paper 2319

Surface Changes in an Original and Activated Bentonite[1]

Juan de Dios Lopez-Gonzalez[2] and Victor R. Deitz

The physical adsorption of nitrogen was used to study a bentonite activated by a treatment with hydrochloric acid. The Brunauer-Emmett-Teller equation, the Hüttig equation, and a so-called "summation" equation were used in the calculation of the surface areas available to nitrogen. The changes in surface area at different temperatures have been related to the quantity of adsorbed water and the amount of constitutional hydroxyl groups. The surface area is a measure of only the external boundary (nonswelling surface) of the bentonite, and this is increased significantly by the activation process. The ratio of surface areas (activated to original) is about four. A maximum in the surface area was found to exist when all of the adsorbed water was eliminated. However, the surface area decreased with the removal of water formed by decomposition of the constitutional hydroxyl groups. Chemical analyses, dehydration curves, thermal differential analyses, X-ray patterns, and electron micrographs were employed to characterize the materials.

1. Introduction

Bentonite [1][3] is generally defined as a rock that contains 75 percent or more of the crystalline clay-like minerals montmorillonite or beidellite [2 to 7]. The proportions of impurities in samples from many locations have been studied by Ross and Hendricks [4]. The minerals of this group show a wide variability in chemical composition, but there is very little change in the crystalline structure as shown by Werry, Ross, and Kerr [9], Gruner [10], Marshall [11], Holzner [12], Kelley and Jenny [13], etc. The unique behavior of bentonite is evident from the number of specific properties that have been related to its crystal structure [6, 8, 9].

Acid treatments of bentonites significantly change some of the specific properties of interest in industrial processes. If the acid is at relatively low concentration (about 0.1 to 0.01 *N*), the exchangeable cations are replaced by hydrogen ions. If the acid concentration is increased, there is a partial chemical solution of the crystal structure. The extent of the dissolving action depends upon the concentration and nature of the acid, temperature, reaction time, and the ratio of the two reactants.

The decolorizing action and the efficiency of many clay-cracking catalysts, which generally have very specific properties, increase in general with the amount of hydrogen ions present on the surface [14]. Recent studies [15] have shown that the catalytic action of silica-alumina gels can also be related to the hydrogen ions present on the surface. Small amounts of basic compounds (calcium, potassium, nitrogen, etc.) have a poisoning influence on the cracking activity of catalysts. Mills, Boedeker, and Oblad [16] assume that the "active hydrogen ions" are eliminated from the catalyst during cracking, and as a result the cracking activity is decreased.

Water contained in bentonites also plays a very important role in their adsorbent properties in nonaqueous media. This water, generally determined by loss of weight after heat treatments, is in part adsorbed water and in part due to the decomposition of the constitutional hydroxyl groups [18, 19]. Both forms, when retained in the bentonite, play an important role in the surface activity. For example, the amount of the dye, Red Sudan B, adsorbed by bentonites from benzene solutions was shown by Castro and Gonzalez [17] to change notably with moisture content.

In view of the aforementioned adsorption properties of bentonite, it was considered of interest to measure the changes in surface area brought about by a treatment with hydrochloric acid and to ascertain the influence of the residual water on the total surface. The acid treatment of the bentonite is first described. The original material and the product formed were characterized briefly by chemical and physical-chemical methods in current use. The data for the adsorption of nitrogen at liquid-nitrogen temperature are then presented and these results correlated with surface area and the probable structure of the acid-treated bentonite.

2. Acid Activation of the Bentonite Sample

2.1. Preparation

A commercial sample of bentonite[4] was passed through a U. S. No. 140 sieve in order to eliminate particles greater than about 0.1 mm in diameter. Five hundred grams of this bentonite were refluxed with 5 liters of hydrochloric acid (10% by weight) for 2 hours. The acid-treated bentonite was washed with distilled water until the wash water was free from chloride ions, and the final product was dried for about 40 hours at 105° C and kept in a desiccator. It has been previously shown [17] that a bentonite treated by this method had the highest adsorptive capacity for the dye Red Sudan B when the concentration of the acid used for activation was about 10 percent by weight. At the lower or higher acid concentrations, a product of less adsorptive capacity was formed.

[1] This investigation was sponsored as a joint research project undertaken by the Bone Char Research Project, Inc. and the National Bureau of Standards.
[2] Guest worker holding a fellowship of the Consejo Superior de Investigaciones Cientificas, Spain.
[3] Figures in brackets indicate the literature references at the end of this paper.
[4] Identified as a southern bentonite (Panther Creek, Miss.).

2.2. Chemical Composition

The chemical composition [5] of the bentonite was determined before and after the acid treatment. The components removed were determined in the filtrate after acid treatment. The results, given in table 1, show that a large part of the aluminum, iron, and magnesium in the original crystal structure was removed. All calcium ions were removed, as was to be expected, because it is a readily exchangeable cation. The silica originally combined with the cations removed was practically insoluble in the hydrochloric acid solution and remained in the residual material. It is known that the crystalline forms of silica are not appreciably soluble under treatment with sodium carbonate [20]. Therefore, the noncrystalline silica was determined as follows: 1 g of the residual material was treated with 100 ml of water containing 5 g of sodium carbonate and boiled for 5 minutes; the filtrate was analyzed for silica.

TABLE 1. *Chemical analysis of bentonite*

[Sample dried at 110° C]

Components	Original bentonite	Activated material [a]	Original components removed by activation [g]
	Percent by weight	*Percent by weight*	*Percent*
SiO_2	[b] 0.84 [c] 59.64	[b] 30.1 [c] 47.7	[d] 0.1
Al_2O_3	21.35	12.7	54.5
Fe_2O_3	6.49	3.5	58.9
MgO	3.01	0.6	83.5
CaO	0.90	.0	100.0
Ignition loss	6.99	5.2	.....
Total	99.22	99.8	.....
Adsorbed water [e]	2.79	2.4	.....
Water from constitutional OH groups	[f] 4.20	[f] 2.8	.....

[a] Loss in weight on activation, 21%.
[b] Amounts of "noncrystalline" silica.
[c] Corresponding amounts of silica in the silicate structure of the bentonite plus a small part which was detected by the X-ray diffraction patterns to be quartz.
[d] Silica found in the solution after the acid treatment.
[e] Defined as the water realized in heating the sample at 350° C to constant weight.
[f] Found from dehydration curves (fig. 1) and from ignition losses.

The amount of "noncrystalline" silica, that is, silica soluble in a boiling 5-percent solution of sodium carbonate, was very small (0.84%) in the original bentonite but was large (30.1%) in the acid-treated material. Apparently, by removing the aluminum, iron, and magnesium, the original silicate is converted into some amorphous form of silica. Table 1 shows that the ignition loss is smaller in the acid-treated material. The latter will henceforth be designated as the "activated material".

2.3. Dehydration Curves

The curves in figure 1 were obtained by the method of Kelley, et al. [19, 21]. The loss in weight of the sample on heating was attributed to the loss of moisture. Both graphs were characterized by a definite change in curvature, beginning at about 300°C. Above 550°C the amount of water removed changed only slightly with increase of temperature. The similarity in the shapes of the two curves indicates that the activated material has a structure similar to that of unactivated bentonite. The breaks in the curves at 300°C correspond to a water loss of approximately 4.2 percent and 2.8 percent in the original and activated samples, respectively. These figures were calculated with respect to the final weight of the sample after heating to 850°C. According to many other investigators, these values correspond to the water formed in the decomposition of hydroxyl groups in the bentonite. Therefore, the activated product on this basis would contain only two-thirds of the constitutional hydroxyl groups contained in the original bentonite.

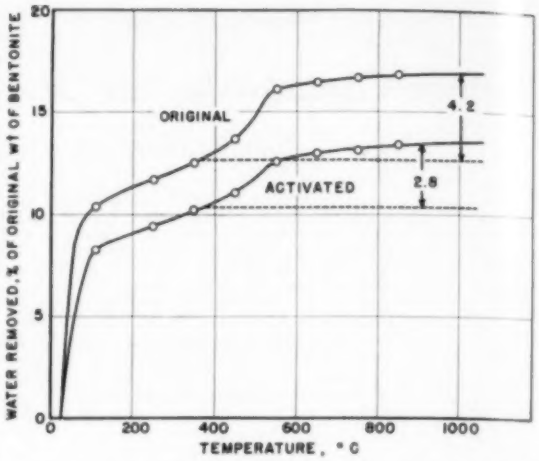

FIGURE 1. *Dehydration curves for the original and activated bentonites.*

2.4. Differential Thermal Analysis

Figure 2 shows differential thermal analyses for the original and activated samples.[6] These results represent the rate of heating a sample as compared with a sample of indifferent material recorded as a function of the temperatures at which differences in the rates of heating occur [22]. Two principal minima were observed, one near 200° and the other near 700° C. The depths of the minima are smaller in the activated bentonite. Apparently, the adsorbed water is retained more weakly in the activated material than in the original bentonite. The slight minimum at 690° C for the activated material indicates the removal of a large part of constitutional hydroxyl groups as a result of the acid activation process.

[5] The authors are indebted to R. B. Rudy and H. I. Feinsten of the Bureau for some of the chemical analyses.

[6] The authors are indebted to E. S. Newman of the Bureau for the experimental results.

UNIVERSITY OF MICHIGAN LIBRARIES

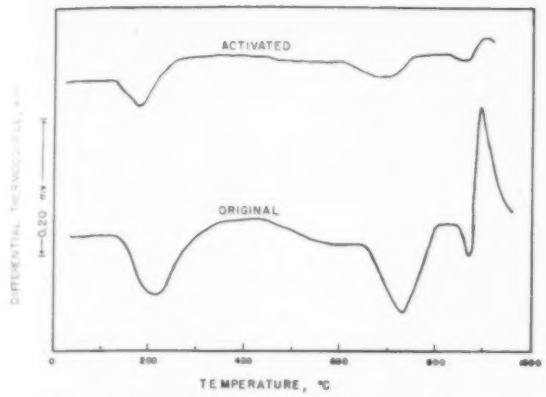

FIGURE 2. *Differential thermal analysis curves of the original and activated bentonite.*

2.5. X-Ray Diffraction

X-ray diffraction patterns [7] were taken of the original bentonite after it was heated at 350° C and of the acid-activated material after it was heated at 250° C. These are given in figure 3. The X-ray diffraction patterns of the resulting material showed a great intensity for the (*hk*0) reflections when compared with the (00*l*) reflections. This indicates that the bentonite heated to 350° had a poor crystallographic development in the direction of the *c*-axis.

In the activated material, heated only at 250° C, a total destruction of the basal reflections was observed. This could indicate a total destruction of the montmorillonitic structure by the acid treatment. Previous work [33] has shown that a heat treatment of bentonite at 250° C produces only minor changes in structure when compared with that produced by the acid treatment. However, the persistence of the (*hk*0) reflections in the activated bentonite indicates that the planar arrangement

[7] The authors are indebted to the Constitution and Microstructure Section of the Bureau for the X-ray patterns and the electron micrographs.

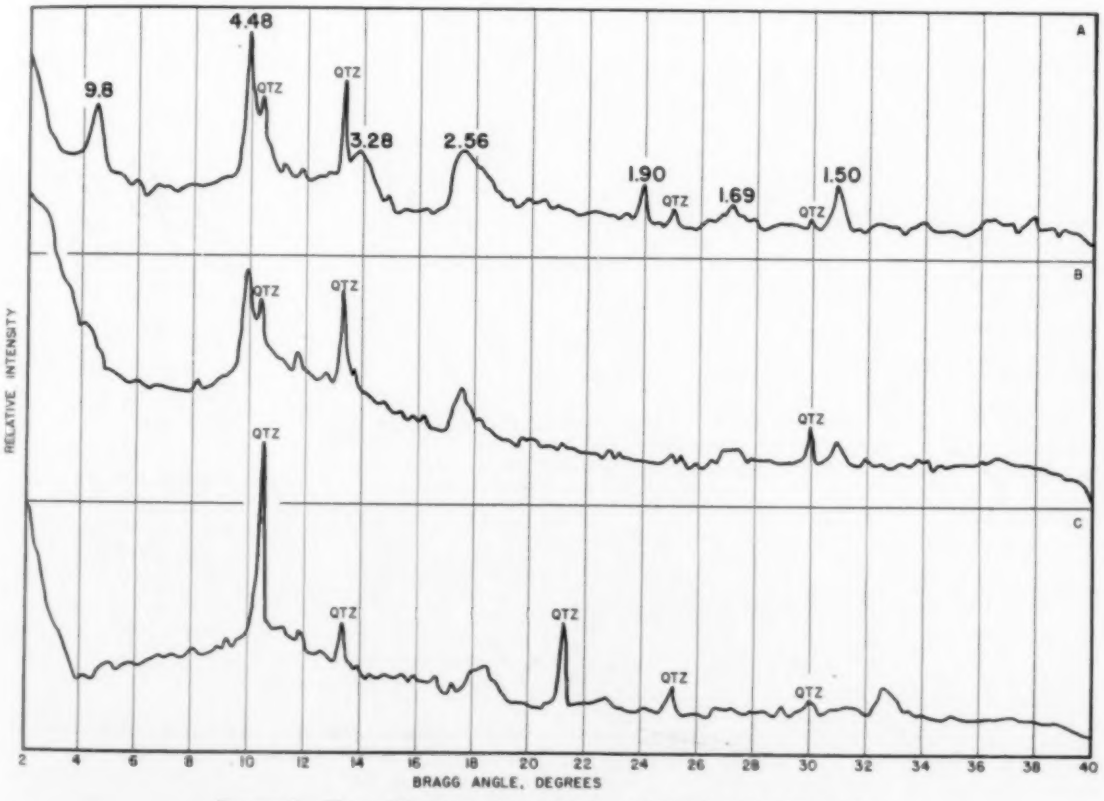

FIGURE 3. *X-ray diffraction patterns for the original and activated bentonite.*

The maxima denoted by qtz designate reflections similar to those observed in the X-ray structure of quartz. A, original after heating at 350° C; B, activated material after heating at 250° C; C, heated to 850° C.

with respect to c axis is poor, and the destruction of relatively few layers in each crystal is enough to show an apparent total disorder with respect to basal reflections. This disorder can be attributed to the presence of the residual non-crystalline silica between the layers of the montmorillonite.

X-ray diffraction patterns showed that the structure of both original bentonite and activated material changed completely when heated at 850° C.

2.6 Electron-microscope pictures

Samples of the original bentonite and activated material were prepared for electron micrographs with butyl alcohol as a dispersing agent, after practically complete removal of the adsorbed water. The micrographs do not show differences between the two samples, either in particle shape or in size. This indicates that the noncrystalline silica, formed by the action of hydrochloric acid, remains between the residual layers of the bentonite where it cannot be detected.

3. Adsorption of Nitrogen and the Calculation of V_m

3.1. Data

The adsorption isotherms of nitrogen at −195° C were determined with a conventional B. E. T. apparatus [23]. The temperature of the liquid nitrogen was ascertained by means of a nitrogen vapor pressure thermometer. The results for the original bentonite are given in table 2 and those for the activated bentonite in table 3. Samples were evacuated before the adsorption measurements for periods of 18 hours at each of the following temperatures: 110°, 250°, 350°, and 450° C. Other samples contained in porcelain dishes were heated at 550°, 650°, 750°, and 850° C in an electric furnace. These were transferred to the adsorption apparatus and evacuated for 18 hours at 450° C before the adsorption measurements. Desorption measurements were also made in a number of cases.

In order to adsorb nitrogen in the presence of large amounts of water in the bentonite, fresh samples were exposed to water vapor, placed in the adsorption bulb, and then evacuated at either −78° or +25° C for a period of 45 minutes. The samples were then cooled to −195° C for the nitrogen adsorption measurements. A portion of the wet sample was analysed for moisture content.

Typical adsorption isotherms are given in figure 4. These correspond to the type II isotherms of Brunauer's classification [23]. In all cases the activated bentonite (curves 1′, 2′, 3′, 4′) adsorbed more nitrogen than the original (curves 1, 2, 3, 4) after comparable evacuation temperatures. The desorption experiments indicated that hysteresis phenomena were rather small with the original bentonite but were greater in the activated material, in agreement with its greater content of particle voids. The volume of gas adsorbed at a given pressure increased with the temperature of evacuation of the samples up to a maximum and then decreased. For example, curve 1′ of figure 4 was obtained after an initial evacuation at 25° C, curve 2′ after evacuation at 110° C, curve 3′ after evacuation upon treatment at 650° C, and curve 4′ after evacuation upon treatment at 750° C.

TABLE 2. *Adsorption of nitrogen at −195° C.*

Original bentonite

p	V	p	V
Evacuation at −78 C for 45 min		Evacuation after 550° C for 18 hr	
56.9	0.48	43.8	17.4
114.7	.48	119.2	20.6
196.5	.49	172.7	22.3
260.6	.48	233.3	24.1
679.9	.88		
748.7	2.29		
762.3	3.67		
768.2	5.51		
773.6	6.86		
Evacuation at 25° C for 45 min		Evacuation after 650° C for 18 hr	
44.6	5.6	33.1	14.0
69.1	6.2	170.7	18.7
112.7	6.9	229.0	20.4
171.7	7.9	288.8	22.2
264.2	9.4	348.6	24.3
452.9	13.4	506.9	31.1
570.2	17.7	643.2	42.5
713.6	36.5	692.8	52.3
737.3	46.3	713.7	60.9
748.6	59.9	626.4	*46.3
295.5	*9.9	342.6	*24.2
73.8	*6.1	132.8	*17.6
24.9	*5.0	59.5	*15.3
Evacuation at 110° C for 18 hr		Evacuation after 750° C for 18 hr	
6.3	4.7	12.5	2.9
23.4	18.2	74.6	6.0
184.9	25.1	130.8	6.9
327.1	30.2	190.9	7.7
478.4	36.5	273.7	9.0
642.0	46.3	442.5	12.6
372.0	*33.8	566.5	16.7
185.0	*25.3	678.6	26.6
69.4	*21.4	712.2	34.8
		731.3	40.6
		710.1	*37.4
		657.9	*28.3
		499.2	*16.5
		233.4	*7.1
		74.9	*4.7
		35.2	*3.9
Evacuation at 250° C for 18 hr			
mm Hg	ml/g		
42.1	19.0		
178.0	23.7		
222.1	25.0		
271.6	26.5		
Evacuation at 350° C for 18 hr		Evacuation after 850° C for 18 hr	
mm Hg	ml/g	102.9	0.10
85.2	22.8	152.0	.11
177.5	25.7	216.8	.11
210.8	26.8	382.9	.11
253.3	28.2	534.1	.14
		740.0	.35
		766.2	1.10
		767.8	2.27
		729.4	*.39
Evacuation at 450° C for 18 hr			
49.9	20.2		
84.4	22.0		
135.3	23.7		
217.0	26.2		

*Desorption points.

TABLE 3. *Adsorption nitrogen at −195° C.*

Activated bentonite

p	V	p	V
Evacuation at −78° C		Evacuation at 450° C	
16.8	2.2	57.6	63.7
69.4	3.3	114.7	73.4
135.8	4.0	198.4	85.8
188.7	4.4	237.8	89.6
248.3	4.9		
413.0	6.6		
638.9	12.5		
704.7	12.2	Evacuation after 550° C	
733.6	20.5		
752.2	23.6		
763.4	26.3		
711.0	*20.2	6.4	27.5
646.2	*16.4	88.0	60.3
520.3	*10.1	173.9	72.2
296.5	*5.3	233.6	80.2
132.3	*3.9		
Evacuation at 25° C		Evacuation after 650° C	
38.6	19.3	3.2	18.1
73.6	23.3	20.9	41.6
128.8	27.7	119.6	59.1
206.1	33.0	185.1	67.5
280.5	38.6	281.2	80.3
373.5	47.6	408.0	102.4
480.3	61.9	520.1	131.6
568.7	84.3	589.4	153.9
639.9	111.9	625.5	173.0
678.6	130.0	649.8	190.7
700.3	142.5	612.3	*178.5
720.1	154.7	502.5	*139.5
452.0	*75.1	391.2	*104.5
		278.0	*80.0
		169.6	*65.6
		101.4	*56.6
Evacuation at 110° C			
7.3	10.1	Evacuation after 750° C	
8.8	37.1		
82.5	69.8		
243.2	94.5		
397.2	123.2	19.6	33.3
510.3	155.3	161.5	53.4
357.9	*119.3	210.6	58.8
235.3	*93.1	247.2	63.2
116.1	*76.6	292.4	69.1
		415.2	89.0
		515.9	113.0
Evacuation at 250° C		575.3	133.9
		616.9	151.5
		646.1	166.5
mm Hg	ml/g	528.0	*128.1
10.2	37.1	428.7	*98.7
104.0	76.4	330.3	*74.6
167.2	86.1	212.8	*58.9
212.4	93.0		
Evacuation at 350° C		Evacuation after 850° C	
mm Hg	ml/g	65.7	17.4
34.7	61.1	119.2	20.2
162.8	83.5	165.7	22.3
215.6	91.4	249.2	26.0
265.5	99.2		

*Desorption points.

UNIVERSITY OF MICHIGAN LIBRARIES

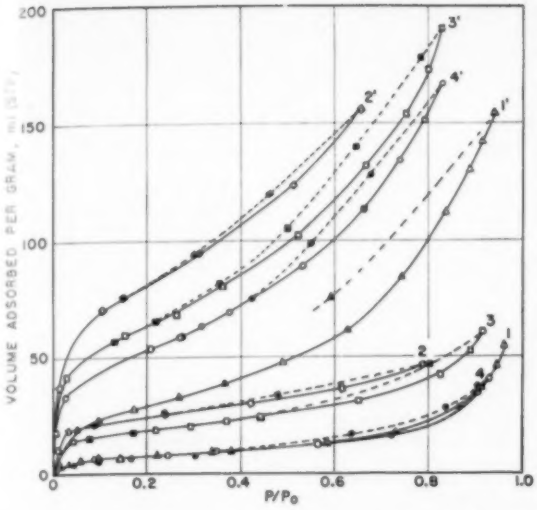

FIGURE 4. *Adsorption isotherms of nitrogen at − 195° C on the original and activated bentonite, after evacuation at different temperatures: numbers 1, 2, 3, and 4 correspond to the original bentonite evacuated at 25°, 110°, 650°, and 750° C, respectively; numbers 1′, 2′, 3′, and 4′ correspond to the activated bentonite evacuated at 25°, 110°, 650°, and 750° C, respectively.*

3.2. Determination of V_m

In current theories of physical adsorption, V_m is defined as the volume of adsorbed gas, calculated at standard temperature and pressure (STP), which covers the available surface with a single layer of molecules. The value of V_m has been determined by using a number of different equations for adsorption isotherms at 78° K.

The free-surface isotherm for multimolecular adsorption derived by Brunauer, Emmett, and Teller [24] may be written according to eq 1:

$$\frac{p}{V(p_0-p)}=\frac{1}{cV_m}+\left(\frac{c-1}{cV_m}\right)\frac{p}{p_0}, \qquad (1)$$

where p is the pressure in equilibrium with the adsorbent, p_0 the pressure in equilibrium with liquid nitrogen, V the volume of gas adsorbed, and c is a constant related to the heat of adsorption. According to this equation a plot of $p/[V(p_0-p)]$ as a function of p/p_0 should be a straight line. Actually, the required linearity was observed only for values of p/p_0 less than about 0.5 for the majority of isotherms. As an example, data are plotted in figure 5 for the case in which both samples of bentonite were evacuated at a temperature of 25° C preliminary to the measurements.

The isotherm proposed by Hüttig [25, 26] may be written

$$\frac{p}{Vp_0}\left[1+\frac{p}{p_0}\right]=\frac{1}{cV_m}+\left(\frac{1}{V_m}\right)\frac{p}{p_0}. \qquad (2)$$

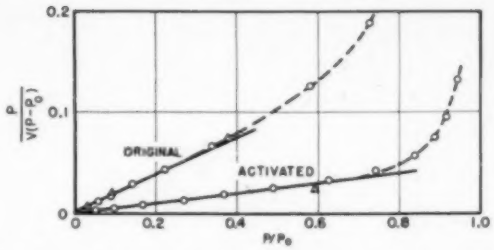

FIGURE 5. *Brunauer-Emmett-Teller linear plot for nitrogen adsorbed on the original and activated bentonite evacuated at 25° C, in accordance with eq 1.*

o, Adsorption; △, desorption.

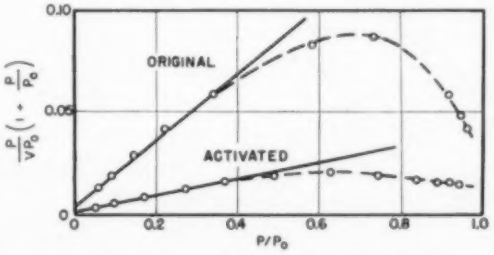

FIGURE 6. *Hüttig linear plot for adsorbed nitrogen on the original and activated bentonite evacuated at 25° C, in accordance with eq 2.*

A straight line should be obtained when the left side of eq 2 is plotted as a function of p/p_0. When this equation was applied to the data for bentonite, the deviation from linearity was observed for values of p/p_0 greater than about 0.4. A typical plot of these data is shown in figure 6. In general, the data do not conform to the Hüttig equation as well as they do to the B. E. T. equation.

A simple relationship was observed that yielded a linear plot for values of p/p_0 as high as 0.8. This relation is obtained by adding eq 1 and 2 to give eq 3:

$$\frac{p}{2Vp_0}\left[\frac{p_0}{p_0-p}+\frac{p_0+p}{p_0}\right]=\frac{1}{cV_m}+\left(\frac{c-1/2}{cV_m}\right)\left[\frac{p}{p_0}\right]. \qquad (3)$$

In this case a straight line is to be expected on plotting the left side of eq 3 as a function of p/p_0. A typical plot is given in figure 7. A straight line was obtained up to a value of p/p_0 of 0.8.

It should be noted that the improved equation does not contain any constants other than those in the original B. E. T. theory. The fact that the straight-line relationship holds over a greater range of pressure is an advantage for the determination of the value of V_m. The fact that the adsorption data yields a straight line over a greater pressure range when plotted according to eq 3 is a necessary but not sufficient criterion for the correctness of the equation.

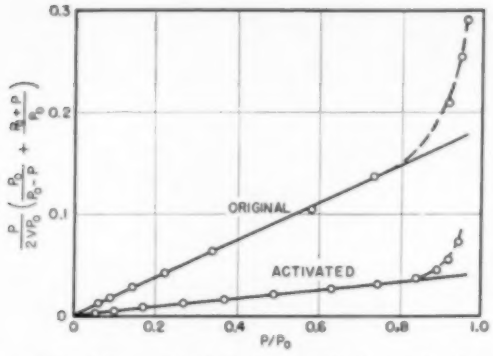

FIGURE 7. *Linear plot of the "summation" equation for adsorbed nitrogen on the original and activated bentonite evacuated at 25° C, in accordance with eq 3.*

There are other important requirements for a theory of multimolecular adsorption, but these will not be discussed in this paper.[8]

4. Variation of V_m with Water Content of Bentonites

Table 4 lists the values of V_m when calculated according to eq. 1, 2, and 3 and the corresponding surface areas. It can be seen that the results according to eq 3 [the "summation" equation] are always between those derived form the B. E. T. and Hüttig equations. The question arises as to which value gives the best approximation. For the purposes of a surface area determination it may be noted that average deviation of the B.E.T. value from that of the summation equation is usually less than 10 percent.

TABLE 4. *Values of V_m and surface areas of original and activated bentonite calculated by B. E. T., Hüttig, and the proposed summation (Σ) equation.*

Evacuation Temp.	V_m			m^2/g [a]		
	B.E.T.	Hüttig	Σ	B.E.T.	Hüttig	Σ
Original bentonite						
°C						
−78	0.35	0.37	0.36	1.5	1.6	1.6
25	6.3	7.0	6.6	27.7	30.6	28.7
110	19.2	20.9	19.3	83.8	91.3	84.5
250	17.8	20.0	18.7	77.8	87.4	81.8
350	19.1	21.4	20.1	83.5	93.5	87.9
450	20.0	21.0	20.5	87.3	91.9	89.5
550	17.5	18.8	17.9	76.4	82.3	78.1
650	14.6	17.6	15.2	63.6	76.6	66.5
750	6.81	6.8	6.4	26.5	29.7	27.9
850	0.051	0.052	0.051	0.22	0.23	0.22
Activated bentonite						
−78	3.5	3.7	3.7	15	16	16
25	24.8	28.7	27.4	108	125	120
110	65.7	72.4	68.7	287	317	300
250	70.4	75.8	72.8	308	329	318
350	67.2	74.7	71.0	294	327	310
450	65.8	72.9	69.1	288	319	302
550	57.0	61.6	59.5	249	269	260
650	52.1	61.3	57.1	228	268	250
750	43.9	57.1	45.3	192	250	198
850	18.1	20.3	19.3	79	89	85

[a] The surface area values are referred to samples dried at 110° C and the cross-sectional area of the adsorbed nitrogen molecule at of 16.1 A^2.

[8] The theory of Hüttig for multimolecular adsorption, recently discussed by Ross [26], Ferguson and Barret [27], and by Hüttig himself [28] has been critized Hill [29]. He has shown that Hüttig's equation cannot be obtained from the B. E. T. Model without violation of statistical thermodynamical principles. Hill points out that the B. E. T. Model results in too low a free energy relative to the liquid state, and that Hüttig's treatment leads to a free energy that is too high [30].

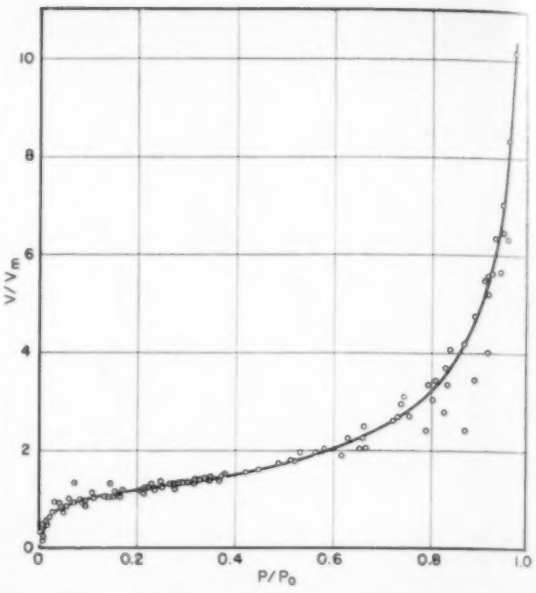

FIGURE 8. *Adsorption isotherms of nitrogen at −195° C on the original and activated bentonite evacuated at 10 different temperatures, reduced to unit surface.*

In figure 8 is presented a plot of V/V_m for all the data as a function of p/p_0. The close superposition of the data is striking and demonstrates that the volumes adsorbed are directly proportional to the surface area.

4.1. Areas After Preliminary Temperature Treatment

The temperature at which the initial evacuation of the sample was made has considerable influence on the resulting surface area. This is shown graphically in figure 9. In the case of the original bentonite, the surface area changed little when the tempera-

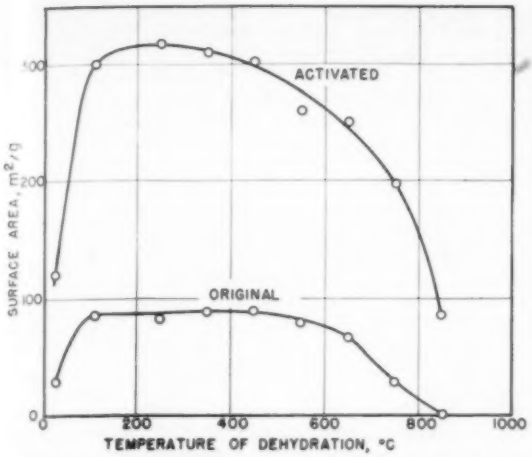

FIGURE 9. *Surface area of the original bentonite and activated material as a function of the temperature of evacuation.*

ture of evacuation was between 100° and 500° C. When higher temperatures were employed, the surface area declined steadily and reached a very small value at 850° C. In contrast, the acid-treated bentonite attained a maximum surface area of almost four times the original area after heating at 250° to 350° C. The maximum for the activated sample was sensitive to temperature, and the area began to fall off appreciably at higher temperatures in the range where there was little change in the area of the original bentonite.

4.2. Areas After Preliminary Water Addition

The relations between the surface areas and the residual moisture retained by the bentonites were studied. Samples containing large quantities of moisture were obtained by exposure to water vapor in a closed container. Samples containing less moisture than that in the initial sample (dried to constant weight at 110° C) were prepared by a heat treatment at the elevated temperatures previously mentioned.

It has been noted that the adsorbed water in bentonite [21] may be considered to be expelled completely at about 350° C without any significant decomposition of the constitutional hydroxyl groups. Therefore, when the moisture content was referred to the constant weight of the samples at 350° C, it was possible to compare changes in surface area with the quantity of adsorbed water, and with the extent of the decomposition of the constitutional hydroxyl groups. The results are plotted in figure 10. The surface area of the original bentonite decreased continuously with increase of adsorbed water from a maximum of 89 to 1.6 m^2/g; the latter value is for a sample containing 30.6 percent of moisture (see curve A). Furthermore, the surface area decreased with loss of the water derived from the decomposition of the constitutional hydroxyl

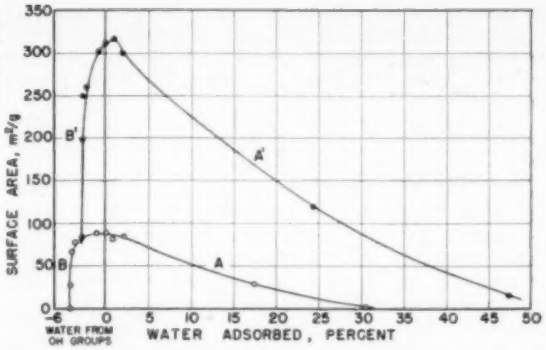

FIGURE 10. *Surface area of the original bentonite and activated material as a function of the amount of adsorbed water and constitutional hydroxyl groups.*

A and B are for original samples of bentonite and A′ and B′ for activated material.

groups to a minimum value of 0.22 m^2/g (see curve B) realized after heating the sample at 850° C.

Similar behavior was found for the activated material. The surface area decreased from a maximum of 320 to 16 m^2/g at a moisture content of 47.4 percent (see curve A′). When the activated material was heated (to constant weight), there was a progressive loss in surface area, the area decreasing to 85 m^2/g after heating to 850° C (see curve B′).

5. Discussion and Concluding Remarks

The acid treatment of the bentonite employed destroys a large part of its crystal structure by removing aluminum, magnesium, and iron. The chemical analyses, dehydration curves, differential thermal analyses, X-ray diffraction patterns, and electron microscope picture indicate that the acid-treated bentonite contains a part of the original montmorillonitic structure.

After removal of aluminum, magnesium, and iron from the crystal structure, a residue of silica remains in the activated product. From the X-ray patterns and electron microscope picture, it seems most probable that this noncrystalline silica remains chiefly between the residue crystal layers and pro-produces a crystalline disorder with respect to the *c* crystallographic axis.

From the intensity of the (*hk*0) reflections in the activated product, after heat treatment at 250°, it should be possible to estimate the amount of bentonite (after 350° C treatment) destroyed by the acid treatment, but the error in doing so is about 25 percent, due to several factors that will not be discussed in this paper. It is important to observe that the absorption of X-rays by the noncrystalline silica formed in the acid treatment results in diminished intensities of the reflections, and as a result could be interpreted as too low a percentage of residual montmorillonitic structure in the activated product. By comparison of the above-mentioned

reflections, and taking also into consideration the chemical analyses, dehydration curves, and differential thermal analyses, it can be estimated that the residual montmorillonitic structure in the activated material is of the order of 50 to 70 percent.

The surface area available to nitrogen at −195° C of the original dried bentonite (85 to 90 m^2/g) is only the external surface (nonswelling surface). This corresponds favorably with the theoretical value given by Dyal and Hendricks [31]. This value corresponds to only 10 percent of the total surface when dispersed into structural single layers, and it has been given by these authors and by Vivaldi [32] as about 880 m^2/g. Therefore, nitrogen cannot be adsorbed to an appreciable extent between the swelling layers of the original bentonite containing moisture.

The surface area of the activated material after elimination of the adsorbed water at 250° to 350° C is about 320 m^2/g. This value is smaller than the total theoretical value of 880 m^2/g for the montmorillonite dispersed into structural single layers. Apparently, the acid destroys part of the layers and creates an open structure, which, in the dried material, is available to nitrogen to a larger extent than in the original bentonite.

The previous and the following considerations make it possible to suggest a simplified view of the reaction between the acid and the smallest particle of material having the properties of the bentonite. The crystalline particles of montmorillonite are composed of aggregates about 10 single structural layers. Let us assume that a particle of the final activated product contains about 60 percent by weight of the bentonite, the acid attack having destroyed four out of ten layers (see fig. 11). In the residual structure, the crystal fragments *A*, *B*, and *C* do not necessarily have to be oriented parallel. The silica, produced during the acid attack, is insoluble and is retained in the residue, which now contains sufficiently large particle voids to permit the entrance of nitrogen into the spaces *a* and *b*. Figure 11 shows that the area of the acid-treated material is three times that of the bentonite, approximately 250 m^2/g. Taking into account the loss in weight (20%) as a result of acid treatment, the surface area per gram of the residue is 320 m^2/g. This compares favorably with that found experimentally (315 to 320 m^2/g).

In practice, the process of acid attack is probably much more complicated. The destruction of the crystal layers must take place according to some random distribution. The proposed simplified model can also account for the observed desorption isotherms. The hysteresis observed for the activated material is attributed to the formation of the small particle voids such as *a* and *b* in figure 11. Hysteresis was not appreciable in the original bentonite.

The decrease in surface area with increase of adsorbed water can be explained by an aggregation of the individual particles. This process would explain the decrease in surface area of the bentonite from 85 m^2/g with no adsorbed water to 1.6 m^2/g with about 31 percent of water. The same effect is shown in the activated material, where the surface area decreases from 320 m^2/g with no adsorbed water to 16 m^2/g with about 47 percent of adsorbed water. The larger amount of adsorbed water in the activated material can be anticipated in view of its "open" structure.

The maxima in surface areas were observed when all the adsorbed water was removed, that is, at 250° to 350° C. In the original bentonite, most of the external surface was lost between 650° and 750° C after the majority of the constitutional hydroxyl groups had been driven off. In the acid-treated bentonite the surface area decreased appreciably at a temperature where the original bentonite showed little change. This behavior suggests that the more irregular structure of the activated material is less stable.

It appears possible to select a temperture in the heat treatment of a sample at which only adsorbed water is removed. This fact is very important, especially where acid-treated bentonite is to be used in applications that require the maximum in surface area. The heat treatment preliminary to use can be confined to temperatures where only adsorbed water is removed. These facts further emphasize the importance of temperature control when bentonite is heated in adsorbing and catalytic processes.

The authors acknowledge the helpful suggestions of W. V. Loebenstein, F. G. Carpenter, and H. P. Freeman of this Bureau and S. B. Hendricks and J. M. Vivaldi of the Bureau of Plant Industry, U. S. Department of Agriculture.

6. References

[1] C. S. Ross and E. V. Shannon, J. Am. Ceram. Soc. **9**, 77 (1926).
[2] C. W. Davis and H. C. Vacher, Bureau of Mines Tech. Paper 438 (1928).

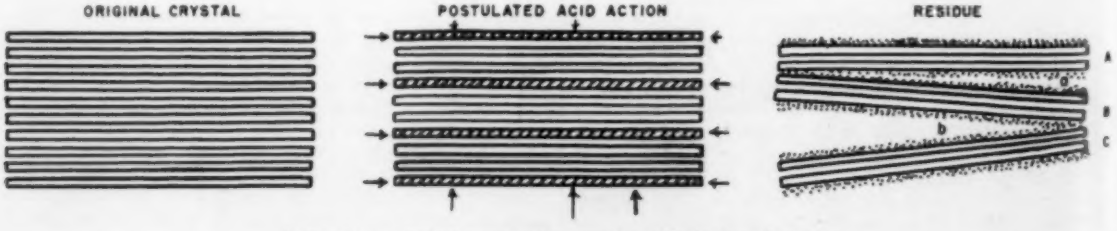

FIGURE 11. *Probable mechanism for the acid attack on bentonite.*

UNIVERSITY OF MICHIGAN LIBRARIES

[3] M. L. Jackson, Ph. D. Thesis, Univ. of Wisconsin (1939).
[4] C. S. Ross and S. B. Hendricks, U. S. Geol. Survey Professional Paper 205–B (1945).
[5] E. G. Rios and F. G. Garcia, Anales Edaf. Fisiol, Veg. T VII, **III,** 605 (1948).
[6] U. Hoffman, K. Endell, and D. Wilm, Z. Krist. **86A**, 340 (1933).
[7] U. Hofmann and W. Vilke, Kolloid-Z. **77,** 239 (1936).
[8] G. H. Edelman and J. Favejee, J. Krist. **102,** 417 (1940).
[9] E. T. Wherry, C. S. Ross and P. F. Kerr, Colloid Symposium Annual 191 (1930).
[10] J. W. Gruner, Am. Mineral. **20,** 475 (1935).
[11] C. E. Marshall, Z. Krist. **91A,** 433 (1936).
[12] J. Holzner, Chem. Erde **9,** 464 (1936).
[13] W. P. Kelley and H. Jenny, Soil Sci. **41,** 367 (1936).
[14] C. L. Thomas, J. Hickey, and G. Stecker, Ind. Eng. Chem. **42,** 866 (May 1950).
[15] T. H. Milliken, Jr., C. A. Mills, and A. G. Oblad, Faraday Soc. Discussion, No. 8, 279 (1950).
[16] G. A. Mills, A. R. Boedeker, and A. G. Oblad, J. Am. Chem. Soc. **72,** 1554 (1950).
[17] A. Hoyos de Castro and J. deD. Lopez-Gonzalez, Anales Edaf. y Fisiol. Veg. **6,** 623 (1950).
[18] J. Mering, Trans. Faraday Soc. **42B,** 205 (1946).
[19] W. P. Kelley, H. Jenny, and S. M. Brown, Trans. Third Int. Congr. Soil Sci. **3,** 84 (1935).
[20] C. S. Ross and S. B. Hendricks, U. S. Geol. Survey Professional Paper 205–B, p. 36 (1945).
[21] W. P. Kelley, H. Jenny, and S. M. Brown, Soil Sci. **41,** 259 (1936).
[22] R. E. Grim and R. A. Rowland, Am. Mineral. **27,** 746 to 761, 801 to 818 (1942).
[23] S. Brunauer, The adsorption of gases and vapors (Princeton Univ. Press, Princeton, N. J., 1943).
[24] S. Brunauer, P. H. Emmett, and E. Teller, J. Am. Chem. Soc. **60,** 309 (1938).
[25] G. F. Hüttig, Monatsh. **78,** 177 (1948).
[26] S. Ross, J. Phys. Colloid Chem. **53,** No. 3, 383 (1949).
[27] R. R. Ferguson and R. M. Barrer, Trans. Faraday Soc. **46,** 400 (1950).
[28] G. F. Hüttig and O. Theimer, Kolloid-Z. **119,** 69 to 73 (1950).
[29] T. L. Hill, J. Am. Chem. Soc. **72,** 5347 (1950).
[30] T. L. Hill, private communication.
[31] R. S. Dyal and S. B. Hendricks, Soil Sci. **69,** 421 to 432 (1950).
[32] J. M. Vivaldi, private communication.
[33] F. G. Garcia, Anales de Fisica y Quimica (Spain) **45,** 1183 to 1210 (Sept.-Oct. 1949).

WASHINGTON, January 8, 1952.

Journal of Research of the National Bureau of Standards Vol. 48, No. 4, April 1952 Research Paper 2310

Arc Spectra of Gallium, Indium, and Thallium

William F. Meggers and Robert J. Murphy

The arc spectra of gallium, indium, and thallium have been systematically investigated photographically in the octave 6500 to 13000 Angstroms. The spectra were excited in direct-current arcs and recorded on infrared sensitive photographic emulsions with a concave diffraction grating 22 feet in radius. In the designated spectral range, 37 new lines were photographed in Ga I, 35 lines in In I, and 25 lines in Tl I. All the observed lines are explained as combinations of doublet terms arising from the axial and orbital momenta of a single-valence electron. The new data led to a revision of Ga I terms, and extension from $n=9$ to 12 for $ns\,^2S$, from $n=7$ to 11 for $nd\,^2D$, and to the discovery of $nf\,^2F^\circ$ terms from $n=4$ to 7. Besides confirming many terms already known for In I and Tl I, two new $nf\,^2F^\circ$ terms were found for each of these spectra.

1. Introduction

This research was inspired by the compilation of "Atomic energy levels as derived from the analyses of optical spectra" [1].[1] While compiling the data on gallium spectra, C. E. Moore noted that the first spectrum of gallium (Ga I) was very incompletely investigated. In particular, no Ga I lines had been observed with wavelengths greater than 6414 A in the red, although two infrared lines (11904 and 12096 A) were predicted in 1914 from spectral-series formulas [2]. These predicted infrared lines have now been recorded photographically, and, in addition, 37 new Ga I lines have been discovered. These observations have led to revision and extension of the known atomic-energy levels as derived from the analysis of the Ga I spectrum.

Inspection of the published papers on In I and Tl I (analogues of Ga I) indicated that these spectra also had not been adequately investigated photographically in the region of longer waves. In 1938 Paschen [3] photographed the arc spectrum of indium to 9170 A, but the arc spectrum of thallium had never been photographed beyond 6900 A, although Paschen [4] in 1909–10 observed Tl lines from 8376.5 to 71170 A with a bolometer. Excepting Paschen's work on indium, the arc spectra of gallium, indium, and thallium have not been investigated photographically for 30 years, during which period infrared-sensitive emulsions permitting observations to 13000 A have become available. Observations on these spectra in the octave 6500 to 13000 A are reported in the present paper; in each case they led to the discovery of new spectral lines and terms so that the atomic-energy levels of Ga I, In I, and Tl I are now essentially complete.

2. Experimental Details

A conventional direct-current arc between copper electrodes was used for most of these experiments, but it was found necessary to employ also an arc at reduced pressure. The arc was operated with an applied potential of 220 v, and the arc current was rheostat regulated at 8 to 10 amp. The anode consisted of a cupped copper rod, ½ in. in diameter, and the cathode was a copper rod ¼ in. in diameter. To observe the spectrum of gallium, indium, or thallium the anodic cup was filled with a sample to be investigated. Liquid gallium was transferred from a vial to the cup with a platinum spoon, whereas pellets of indium or thallium were placed in the cup with tweezers. The arc in air was struck by drawing a graphite rod between the electrodes.

Because the emulsions available for infrared photography are rather insensitive compared with their response to violet light, success in recording spectra beyond 9000 A requires a bright source, ample sample, and long exposure, in addition to an efficient spectrograph. For example, to record the Tl I line at 13013 A required about 20 g of sample in a 10-amp arc exposed for 5 hours, whereas the iron comparison spectrum was recorded in the third order of the same grating in 1 second! Unfortunately, these source conditions produce spectral line images that are more or less hazy and asymmetrical, especially for red and infrared lines of Ga I, In I, and Tl I. That this is due to collision broadening rather than Doppler effect is shown by the fact that it is just as marked for Tl I as for Ga I, although Tl atoms are three times as massive as Ga atoms. Furthermore, analysis shows that the lines in question invariably involve highly excited states of type-*d* or type-*f* electrons; the transitions from type-*p* to type-*s* electrons always yield sharper lines.

Attempts to sharpen the newly observed lines by exciting them in an arc at reduced pressure were not wholly successful because sharpness and intensity are mutually exclusive in most light sources. Experiments were made with an enclosed arc [5] attached to a pump and pressure gage. When the residual air in the chamber was reduced to a few millimeters (Hg) the lines of Ga I, In I, and Tl I were sharp but faint, and mostly obscured by a strong background of N, O, and NO spectra. The sought lines are somewhat stronger when the pressure of residual air is 7 to 10 cm (Hg), but even then this source is too weak to photograph its lines beyond 9000 A with reasonable exposure time. This source, providing a compromise between intensity and sharpness of spectral lines, could be used in this investigation only in the range 6400 to 8900 A, for which region photographic emul-

[1] Figures in brackets indicate the literature references at the end of this paper.

UNIVERSITY OF MICHIGAN LIBRARIES

ons are a hundredfold more sensitive than those sed for longer waves. Without doubt, sharper lines ould be obtained from discharges at very low pressure in a Paschen hollow cathode, but the present observations were restricted to the classical direct-current arc at atmospheric pressure or partial pressure.

Spectrograms were made with the stigmatic concave grating previously described [6], except that both the grating and mirror were aluminized some years ago. In its first-order spectrum this spectrograph has a reciprocal dispersion of 10 A/mm, and it is now used almost exclusively to photograph infrared spectra on 2- by 10-in. plates embracing wavelength ranges of 2500 A. The range from 10500 to 13000 A was photographed with Eastman I–Z plates, the range from 8500 to 11000 A with Eastman I–Q plates, and the range from 6400 to 8900 A with Eastman I–N plates. The I–Z and I–Q plates were hypersensitized by bathing for 2 minutes in 2- to 7-percent solutions of ammonia in water; they were then dried rapidly before loading in the spectrographic plate holder.

A dark-red-glass filter placed in front of the spectrograph slit absorbed overlapping spectral orders when the first-order spectrum was being photographed. Short portions of the slit were exposed to the iron arc to provide standards for wavelength measurement. For the spectral ranges covered by I–Q and I–Z plates, iron standards were taken from the second-, third-, or fourth-order spectra, but for the range observed with I–N plates the iron comparison spectrum was recorded in the same first order as the other spectra, a deep-yellow-glass filter being employed to absorb the overlapping spectral orders.

3. Results

The wavelengths belonging to lines observed in the arc spectra of gallium, indium, and thallium were calculated from linear measurements of the positions of these lines relative to standard lines in the iron spectrum, and then converted to first-order values if the iron standards appeared in higher spectral orders. Because most of these lines were naturally hazy (*H*) and shaded to longer (*l*) waves, it was usually impossible to specify the wavelength closer than ± 0.1 A, and small corrections due to slight departures from standard-air density were therefore neglected.

Relative intensities of the observed lines were estimated from the spectrograms and adjusted somewhat to correct for obviously excessive estimates when lines happened to be on or near the peak of sensitivity of a particular photographic emulsion. These estimates have physical meaning for proximate lines but may be misleading when comparing the intensities of widely separated lines. An example of the latter is discussed under thallium.

The results of this investigation are presented in two tables for each spectrum, the first gives the experimental data on wavelength, relative intensities and line character, and spectral-term combination, whereas the second table contains a complete list of the atomic-energy levels derived from the analyses of the optical spectra. In general, the Ga I, In I, and Tl I spectra are structurally similar, each line represents a transition of a single electron, which, by virtue of its axial and orbital momenta, gives the atomic-energy levels grouped to form doublet spectral terms. The only exception is a ^{4}P term observed in each of these spectra.

3.1. Gallium

The early history of gallium spectra is given in Kayser's Handbuch der Spectroscopie [7]. Briefly, 14 lines (2450 to 6414 A) reported by Exner and Haschek [8] in 1911 were arranged in three spectral series by Paschen and Meissner [2] in 1914. Uhler and Tanch [9] published for 23 arc lines of Ga wavelengths ranging from 2171.9 to 4172.048 A; Sawyer and Lang [10] added five lines (2607.47 to 2691.29 A), which fix a ^{4}P term, and this is all that was known about the Ga I spectrum to the present time. The present investigation more than doubles the total number of lines previously ascribed to Ga I, and because the final list has rejected some lines and substituted others it is given complete in table 1. This list of Ga I lines gives the best agreement with values calculated from established atomic energy levels displayed in table 2. We are indebted to C. E. Moore for selecting and adjusting these values of wavelengths and atomic-energy levels.

Besides revising some earlier term values, the present observations of Ga I lines have extended the series $5p\ ^2\mathrm{P}^\circ - ns\ ^2S$ from n=9 to 12, the series $5p\ ^2\mathrm{P}^\circ - nd\ ^2\mathrm{D}$ from $n=7$ to 11, and revealed the series $4d\ ^2\mathrm{D} - nf\ ^2\mathrm{F}^\circ$ from $n=4$ to 7, inclusive. The limit, 48380 cm^{-1}, corresponds to an ionization potential of 5.997 ev, the energy required to remove a valence electron from a neutral gallium atom.

3.2. Indium

The arc spectrum of indium was first investigated systematically by Kayser and Runge [13], who in 1893 measured the wavelengths (2180 to 4511 A) of 34 lines and arranged them in two subordinate spectral series. About 22 years later Paschen and Meissner [2] observed nine indium lines (4479 to 6900 A) and placed them in a principal series of doublets. In 1922 Uhler and Tanch [9] published wavelengths (2171 to 4511 A) for 34 indium lines, almost, but not quite, identical with the earlier list by Kayser and Runge [13]. An important contribution was made in 1938 by Paschen [3], who measured the In I spectrum emitted by Geissler tubes and by furnaces, and published wavelengths (2179.90 to 9170.2 A) and term combinations for 107 lines, 27 of which lie in the far red and near infrared. Unfortunately, Paschen neglected to give any intensities to these new lines, 21 of which are quoted by Kayser and Ritschl [14] in their table of principal lines, although they are mostly very weak compared with other In I lines. We have tried to supply estimates of the relative intensities of these In I lines, but a few were too weak and hazy to measure on the spectrograms.

TABLE 1. *The first spectrum of gallium*, Ga I

[h=hazy; H=very hazy; l=shaded to longer waves]

Reference	Wave length	Intensity and character	Wave number		Term combination
			Observed	Calculated	
	Å		cm^{-1}	cm^{-1}	
This work	12109.93	200	8255.43	5.48	$5s\ ^2S_{1/2}-5p\ ^2P^0_{3/2}$
Do	11949.24	400	8366.45	6.45	$5s\ ^2S_{1/2}-5p\ ^2P^0_{1/2}$
Do	11103.90	20	9003.38	3.41	$5p\ ^2P^0_{1/2}-7s\ ^2S_{1/2}$
Do	10968.64	10	9114.41	4.38	$5p\ ^2P^0_{3/2}-7s\ ^2S_{1/2}$
Do	10905.96	100*Hl*	9166.79	6.79	$4d\ ^2D_{2½}-4f\ ^2F^0_{3½}$
Do	10898.53	60*Hl*	9173.05	3.04	$4d\ ^2D_{1½}-4f\ ^2F^0_{2½}$
Do	9593.98	20*h*	10420.35	0.35	$5p\ ^2P^0_{1/2}-6d\ ^2D_{1½}$
Do	9589.18	300*h*	10425.56	5.56	$5p\ ^2P^0_{1/2}-6d\ ^2D_{2½}$
Do	9492.88	200*h*	10531.32	1.32	$5p\ ^2P^0_{3/2}-6d\ ^2D_{1½}$
Do	8944.6	30*h*	11176.9	6.9	$5p\ ^2P^0_{1/2}-8s\ ^2S_{1/2}$
Do	8856.6	20*h*	11287.9	7.8	$5p\ ^2P^0_{3/2}-8s\ ^2S_{1/2}$
Do	8813.7	30*Hl*	11342.8	2.8	$4d\ ^2D_{2½}-5f\ ^2F^0_{3½}$
Do	8808.9	20*Hl*	11349.0	9.0	$4d\ ^2D_{1½}-5f\ ^2F^0_{2½}$
Do	8420.3	10*Hl*	11872.8	2.9	$4d\ ^2D_{2½}-6f\ ^2F^0_{3½}$
Do	8415.8	7*Hl*	11879.1	9.1	$4d\ ^2D_{1½}-6f\ ^2F^0_{2½}$
Do	8389.2	10*h*	11916.8	7.0	$5p\ ^2P^0_{1/2}-7d\ ^2D_{1½}$
Do	8386.2	200*h*	11921.1	1.1	$5p\ ^2P^0_{1/2}-7d\ ^2D_{2½}$
Do	8311.5	100*h*	12028.1	7.9	$5p\ ^2P^0_{3/2}-7d\ ^2D_{1½}$
Do	8171.6	5*Hl*	12234.1	4.1	$4d\ ^2D_{2½}-7f\ ^2F^0_{3½}$
Do	8167.5	3*Hl*	12240.3	0.3	$4d\ ^2D_{1½}-7f\ ^2F^0_{2½}$
Do	8074.25	20*h*	12381.65	1.63	$5p\ ^2P^0_{1/2}-9s\ ^2S_{1/2}$
Do	8002.55	15*h*	12492.58	2.60	$5p\ ^2P^0_{3/2}-9s\ ^2S_{1/2}$
Do	7801.6	4*h*	12814.3	4.2	$5p\ ^2P^0_{1/2}-8d\ ^2D_{1½}$
Do	7800.01	100*h*	12816.97	6.97	$5p\ ^2P^0_{1/2}-8d\ ^2D_{2½}$
Do	7734.77	50*h*	12925.08	5.1	$5p\ ^2P^0_{3/2}-8d\ ^2D_{1½}$
Do	7620.5	10*hl*	13118.9	8.9	$5p\ ^2P^0_{1/2}-10s\ ^2S_{1/2}$
Do	7556.6	6*h*	13229.8	9.8	$5p\ ^2P^0_{3/2}-10s\ ^2S_{1/2}$
Do	7464.0	30*Hl*	13393.9	3.9	$5p\ ^2P^0_{1/2}-9d\ ^2D_{2½}$
Do	7403.0	20*Hl*	13504.3	4.2	$5p\ ^2P^0_{3/2}-9d\ ^2D_{1½}$
Do	7349.3	5*hl*	13603.0	3.2	$5p\ ^2P^0_{1/2}-11s\ ^2S_{1/2}$
Do	7289.6	3*hl*	13714.4	4.1	$5p\ ^2P^0_{3/2}-11s\ ^2S_{1/2}$
Do	7251.4	10*Hl*	13786.6	6.6	$5p\ ^2P^0_{1/2}-10d\ ^2D_{2½}$
Do	7193.6	5*Hl*	13897.4	7.5	$5p\ ^2P^0_{3/2}-10d\ ^2D_{1½}$
Do	7172.9	2*h*	13937.5	7.5	$5p\ ^2P^0_{1/2}-12s\ ^2S_{1/2}$
Do	7116.3	1*h*	14048.4	8.5	$5p\ ^2P^0_{3/2}-12s\ ^2S_{1/2}$

Because the sources employed by Paschen emitted sharper lines, we have quoted his wavelength and wave number values in table 3 in addition to the measured wavelengths, estimated intensities, vacuum wave numbers, and term combinations for 40 In I lines ranging in wavelength from 6847.44 to 12912.6 A. The remainder of the In I spectrum is fully presented (excepting intensities) in Paschen's paper [3]. An extension of the ^2D and ^2S series has been reported by Garton [15], but no details of measurement are available at present.

The complete list of atomic energy levels of In I is found in table 4, where Paschen's term values appear (relative to $5s^2\,5p\ ^2P^0_{3/2}=0.00$), and two new terms ($5f\ ^2F^0$ and $6f\ ^2F^0$) have been interpolated from our infrared observations.

From the limit, 46669.9 cm^{-1}, an ionization potential of 5.785 ev is derived for indium atoms.

3.3. Thallium

The last complete compilation of literature on the spectra of thallium was published 40 years ago by Kayser [16]. As in the case of indium, the first careful investigation of the arc spectrum of thallium was made in 1893 by Kayser and Runge [13], who measured the wavelengths (2129 to 5528 A) of 49 lines and assigned nearly all of them to a principal and to two subordinate series. Four additional visible lines were photographed in 1910 by Eder and Valenta [17], but to this day nobody has reported photographing the Tl I spectrum beyond 6714 A in the red. The infrared emission spectrum of thallium was first explored by Paschen [4], who employed a bolometer and galvanometer to detect about three dozen lines with wavelengths ranging from 8376.5 to 71170 A. The most prominent pair of these infrared lines (11513 and 13014 A) was accounted for by the established series terms, and most of the remainder were interpreted as in agreement with values calculated from the Ritz combination principle applied to known Tl I terms. Some

TABLE 1. *The first spectrum of gallium*, Ga I—Continued

[*h*=hazy: *H*=very hazy: *l*=shaded to longer waves]

Reference	Wave length	Intensity and character	Wave number		Term combination
			Observed	Calculated	
	A		cm^{-1}	cm^{-1}	
This work	7106.82	5*hl*	14067.12	7.07	$5p\ ^2P^{\circ}_{1\frac{1}{2}}-11d\ ^2D_{2\frac{1}{2}}$
Do	7051.24	3*hl*	14178.00	8.04	$5p\ ^2P^{\circ}_{0\frac{1}{2}}-11d\ ^2D_{1\frac{1}{2}}$
Do	6413.47	1000	15587.88	7.88	$5s\ ^2S_{0\frac{1}{2}}-6p\ ^2P^{\circ}_{0\frac{1}{2}}$
Do	6396.58	2000	15629.04	9.04	$5s\ ^2S_{0\frac{1}{2}}-6p\ ^2P^{\circ}_{1\frac{1}{2}}$
[11]	5359.8	.....	18652.2	2.2	$5s\ ^2S_{0\frac{1}{2}}-7p\ ^2P^{\circ}_{0\frac{1}{2}}$
[11]	5353.81	2	18673.1	3.1	$5s\ ^2S_{0\frac{1}{2}}-7p\ ^2P^{\circ}_{1\frac{1}{2}}$
[9]	4172.048	10	23962.31	2.34	$4p\ ^2P^{\circ}_{1\frac{1}{2}}-5s\ ^2S_{0\frac{1}{2}}$
[9]	4032.975	10	24788.61	8.58	$4p\ ^2P^{\circ}_{0\frac{1}{2}}-5s\ ^2S_{0\frac{1}{2}}$
[9]	2944.175	6	33955.47	5.43	$4p\ ^2P^{\circ}_{1\frac{1}{2}}-4d\ ^2D_{1\frac{1}{2}}$
[9]	2943.639	6	33961.66	1.68	$4p\ ^2P^{\circ}_{1\frac{1}{2}}-4d\ ^2D_{2\frac{1}{2}}$
[9]	2874.240	6	34781.63	1.67	$4p\ ^2P^{\circ}_{0\frac{1}{2}}-4d\ ^2D_{1\frac{1}{2}}$
[9]	2719.664	3	36758.39	8.38	$4p\ ^2P^{\circ}_{1\frac{1}{2}}-6s\ ^2S_{0\frac{1}{2}}$
[10]	2691.29	(8)	37146	6	$4p\ ^2P^{\circ}_{1\frac{1}{2}}-4p^2\ ^4P_{0\frac{1}{2}}$
[10]	2665.05	(10)	37511	2	$4p\ ^2P^{\circ}_{1\frac{1}{2}}-4p^2\ ^4P_{1\frac{1}{2}}$
[11]	2659.873	3	37584.62	4.62	$4p\ ^2P^{\circ}_{0\frac{1}{2}}-6s\ ^2S_{0\frac{1}{2}}$
[10]	2632.66	(10)	37972	2	$4p\ ^2P^{\circ}_{0\frac{1}{2}}-4p^2\ ^4P_{0\frac{1}{2}}$
[10]	2624.82	(8)	38087	7	$4p\ ^2P^{\circ}_{1\frac{1}{2}}-4p^2\ ^4P_{2\frac{1}{2}}$
[10]	2607.47	(5)	38339	8	$4p\ ^2P^{\circ}_{0\frac{1}{2}}-4p^2\ ^4P_{1\frac{1}{2}}$
[9]	2500.714	3	39976.53	6.48	$4p\ ^2P^{\circ}_{1\frac{1}{2}}-5d\ ^2D_{1\frac{1}{2}}$
[9]	2500.187	7	39984.96	4.96	$4p\ ^2P^{\circ}_{1\frac{1}{2}}-5d\ ^2D_{2\frac{1}{2}}$
[9]	2450.078	6	40802.67	2.72	$4p\ ^2P^{\circ}_{0\frac{1}{2}}-5d\ ^2D_{1\frac{1}{2}}$
[12]	2418.69	(4)	41332.1	2.2	$4p\ ^2P^{\circ}_{1\frac{1}{2}}-7s\ ^2S_{0\frac{1}{2}}$
[12]	2371.29	(3)	42158.25	8.44	$4p\ ^2P^{\circ}_{0\frac{1}{2}}-7s\ ^2S_{0\frac{1}{2}}$
[9]	2338.596	1	42747.57	9.14	$4p\ ^2P^{\circ}_{1\frac{1}{2}}-6d\ ^2D_{1\frac{1}{2}}$
[12]	2338.24	(3)	42754.08	4.35	$4p\ ^2P^{\circ}_{1\frac{1}{2}}-6d\ ^2D_{2\frac{1}{2}}$
[9]	2297.869	1	43505.15	5.6	$4p\ ^2P^{\circ}_{1\frac{1}{2}}-8s\ ^2S_{0\frac{1}{2}}$
[12]	2294.19	(2)	43574.91	5.38	$4p\ ^2P^{\circ}_{0\frac{1}{2}}-6d\ ^2D_{1\frac{1}{2}}$
[9]	2259.227	1	44249.19	9.87	$4p\ ^2P^{\circ}_{1\frac{1}{2}}-7d\ ^2D_{2\frac{1}{2}}$
[9]	2255.034	1	44331.46	1.8	$4p\ ^2P^{\circ}_{0\frac{1}{2}}-8s\ ^2S_{0\frac{1}{2}}$
[9]	2218.039	1	45070.80	2.0	$4p\ ^2P^{\circ}_{0\frac{1}{2}}-7d\ ^2D_{1\frac{1}{2}}$

of Paschen's infrared Tl lines remain unexplained, although all theoretically possible Tl I terms of any importance are now known. Because some of the proposed combinations are discordant and are forbidden by rigid quantum rules, they must be regarded with suspicion. Additional doubt is cast upon some of Paschen's lines by the fact that in the range observed both bolometrically and photographically there are serious disagreements, Paschen reported some lines that we could not photograph and we photographed some that he did not detect. These differences are shown in table 5, which presents the reported lines in the range of wavelengths, 6549.84 to 13013.2 A, 22 lines with greater wavelengths, according to Paschen, being omitted.

The Tl I line at 13013.2 A is the greatest wavelength that has been recorded by direct photography of metallic arc spectra, and it could be recorded only because it is intrinsically intense. By comparing the photographic density of this line with that of its companion at 11512.8 A, one can conclude that the sensitivity of the I–Z emulsion for 13000 A is of the order of one one-thousandth its maximum sensitivity near 11000 A. It would be a great boon to spectroscopy if the proper dyes could be synthesized and incorporated in emulsions to produce photographic sensitivity at still greater wavelengths.

The Tl I data available in 1922 were collected by Fowler [11] in his report on "Series in line spectra," and the relative values of his atomic energy level' referred to the ground state ($6s^2\ 6p\ ^2P^{\circ}_{0\frac{1}{2}}=0.0$) are presented below in table 6, together with the appropriate quantum notation, and with the inclusion of two new terms ($7f\ ^2F^{\circ}$ and $8f\ ^2F^{\circ}$) derived from the infrared observations.

Longer series have been traced in the Tl I spectrum than in any other spectrum excepting hydrogen and alkali metals. Thus in Tl I the principal quantum number, or shell, for *s* electrons has been traced to 20, for *p* electrons to 16, for *d* electrons to 23, and for *f* electrons to 8. The extrapolated limit of these series is 49264.2 cm^{-1} from the ground state, and the corresponding ionization potential of Tl is 6.1063 ev.

TABLE 2. *Atomic energy levels of* Ga I

Electron configuration	Term symbol	J	Level value	Interval
			cm^{-1}	
$4s^2(^1S)$ $4p$	$4p\ ^2P^o$	$0\frac{1}{2}$	*0. 00*	
		$1\frac{1}{2}$	*826. 24*	826. 24
$4s^2(^1S)$ $5s$	$5s\ ^2S$	$0\frac{1}{2}$	24788. 58	
$4s^2(^1S)$ $5p$	$5p\ ^2P^o$	$0\frac{1}{2}$	*33044. 06*	
		$1\frac{1}{2}$	*33155. 03*	110. 97
$4s^2(^1S)$ $4d$	$4d\ ^2D$	$1\frac{1}{2}$	34781. 67	
		$2\frac{1}{2}$	34787. 92	6. 25
$4s^2(^1S)$ $6s$	$6s\ ^2S$	$0\frac{1}{2}$	37584. 62	
$4s\ 4p^2$	$4p^2\ ^4P$	$0\frac{1}{2}$	37972	
		$1\frac{1}{2}$	38338	366
		$2\frac{1}{2}$	38913	575
$4s^2(^1S)$ $6p$	$6p\ ^2P^o$	$0\frac{1}{2}$	*40376. 46*	
		$1\frac{1}{2}$	*40417. 62*	41. 16
$4s^2(^1S)$ $5d$	$5d\ ^2D$	$1\frac{1}{2}$	40802. 72	
		$2\frac{1}{2}$	40811. 20	8. 48
$4s^2(^1S)$ $7s$	$7s\ ^2S$	$0\frac{1}{2}$	42158. 44	
$4s^2(^1S)$ $7p$	$7p\ ^2P^o$	$0\frac{1}{2}$	*43440. 8*	
		$1\frac{1}{2}$	*43461. 7*	20. 9
$4s^2(^1S)$ $6d$	$6d\ ^2D$	$1\frac{1}{2}$	43575. 38	
		$2\frac{1}{2}$	43580. 59	5. 21
$4s^2(^1S)$ $4f$	$4f\ ^2F^o$	$2\frac{1}{2}$, $3\frac{1}{2}$	*43954. 71*	
$4s^2(^1S)$ $8s$	$8s\ ^2S$	$0\frac{1}{2}$	44331. 9	
$4s^2(^1S)$ $7d$	$7d\ ^2D$	$1\frac{1}{2}$	45072. 0	
		$2\frac{1}{2}$	45076. 1	4. 1
$4s^2(^1S)$ $9s$	$9s\ ^2S$	$0\frac{1}{2}$	45536. 66	
$4s^2(^1S)$ $8d$	$8d\ ^2D$	$1\frac{1}{2}$	45969. 2	
		$2\frac{1}{2}$	45972. 0	2. 8
$4s^2(^1S)$ $5f$	$5f\ ^2F^o$	$2\frac{1}{2}$, $3\frac{1}{2}$	*46130. 7*	
$4s^2(^1S)$ $10s$	$10s\ ^2S$	$0\frac{1}{2}$	46273. 9	
$4s^2(^1S)$ $9d$	$9d\ ^2D$	$1\frac{1}{2}$	46548. 3	
		$2\frac{1}{2}$	46548. 9	0. 6
$4s^2(^1S)$ $6f$	$6f\ ^2F^o$	$2\frac{1}{2}$, $3\frac{1}{2}$	*46660. 8*	
$4s^2(^1S)$ $11s$	$11s\ ^2S$	$0\frac{1}{2}$	46758. 2	
$4s^2(^1S)$ $10d$	$10d\ ^2D$	$1\frac{1}{2}$, $2\frac{1}{2}$	46941. 6	
$4s^2(^1S)$ $7f$	$7f\ ^2F^o$	$2\frac{1}{2}$, $3\frac{1}{2}$	*47022. 0*	
$4s^2(^1S)$ $12s$	$12s\ ^2S$	$0\frac{1}{2}$	47092. 52	
$4s^2(^1S)$ $11d$	$11d\ ^2D$	$1\frac{1}{2}$, $2\frac{1}{2}$	47222. 10	
---	---	---	---	
Ga II $(^1S_0)$	*Limit*		**48380**	
$4s\ 4p^2$	$4p^2\ ^2S$	$0\frac{1}{2}$	62100	
$4s\ 4p^2$	$4p^2\ ^2P$	$0\frac{1}{2}$	65796	
		$1\frac{1}{2}$	66422	626

University of Michigan Libraries

TABLE 3. *First spectrum of indium*, In I

[h=hazy, H=very hazy, l=shaded to longer waves]

Wave length	Intensity and character	Wave length Paschen [14]	Wave number		Term combination
			Observed	Calculated	
A		*A*	*cm*$^{-1}$	*cm*$^{-1}$	
12912. 6	10	.....	7442. 2	1. 92	$6s\ ^2S_{0\frac{1}{2}} - 6p\ ^2P^o_{1\frac{1}{2}}$
11731. 5	20*h*	.....	8521. 7	1. 92	$6p\ ^2P^o_{1\frac{1}{2}} - 8s\ ^2S_{0\frac{1}{2}}$
11334. 9	20*h*	.....	8819. 9	20. 10	$6p\ ^2P^o_{0\frac{1}{2}} - 8s\ ^2S_{0\frac{1}{2}}$
10744. 5	100*Hl*	.....	9304. 54	4. 6	$5d\ ^2D_{2\frac{1}{2}} - 5f\ ^2F^o_{3\frac{1}{2}}$
10717. 5	60*Hl*	.....	9327. 98	7. 9	$5d\ ^2D_{1\frac{1}{2}} - 5f\ ^2F^o_{2\frac{1}{2}}$
10283. 9	5*H*	.....	9721. 27	1. 44	$6p\ ^2P^o_{1\frac{1}{2}} - 7d\ ^2D_{1\frac{1}{2}}$
10257. 3	200*hl*	.....	9746. 48	6. 78	$6p\ ^2P^o_{1\frac{1}{2}} - 7d\ ^2D_{2\frac{1}{2}}$
9977. 5	100*hl*	.....	10019. 8	9. 62	$6p\ ^2P^o_{0\frac{1}{2}} - 7d\ ^2D_{1\frac{1}{2}}$
9428. 2	20*h*	.....	10603. 6	3. 76	$6p\ ^2P^o_{1\frac{1}{2}} - 9s\ ^2S_{0\frac{1}{2}}$
9370. 4	60*Hl*	.....	10669. 0	9. 0	$5d\ ^2D_{2\frac{1}{2}} - 6f\ ^2F^o_{3\frac{1}{2}}$
9350. 0	40*Hl*	.....	10692. 3	2. 3	$5d\ ^2D_{1\frac{1}{2}} - 6f\ ^2F^o_{2\frac{1}{2}}$
9170. 2	10*h*	9170. 2	10901. 9	1. 94	$6p\ ^2P^o_{0\frac{1}{2}} - 9s\ ^2S_{0\frac{1}{2}}$
8909. 6	4*h*	8909. 53	11220. 86	0. 84	$6p\ ^2P^o_{1\frac{1}{2}} - 8d\ ^2D_{1\frac{1}{2}}$
8894. 7	40*hl*	8894. 48	11239. 85	9. 83	$6p\ ^2P^o_{1\frac{1}{2}} - 8d\ ^2D_{2\frac{1}{2}}$
8700. 4	50*hl*	8700. 19	11490. 85	0. 84	$5d\ ^2D_{2\frac{1}{2}} - 7f\ ^2F^o_{3\frac{1}{2}}$
8682. 7	20*hl*	8682. 64	11514. 08	4. 08	$5d\ ^2D_{1\frac{1}{2}} - 7f\ ^2F^o_{2\frac{1}{2}}$
8679. 2	30*hl*	8678. 93	11519. 00	9. 02	$6p\ ^2P^o_{0\frac{1}{2}} - 8d\ ^2D_{1\frac{1}{2}}$
8496. 8	15*h*	8496. 70	11766. 05	6. 04	$6p\ ^2P^o_{1\frac{1}{2}} - 10s\ ^2S_{0\frac{1}{2}}$
8315. 0	15*Hl*	8314. 91	12023. 27	3. 28	$5d\ ^2D_{2\frac{1}{2}} - 8f\ ^2F^o_{3\frac{1}{2}}$
8299. 1	10*Hl*	8298. 82	12046. 60	6. 59	$5d\ ^2D_{1\frac{1}{2}} - 8f\ ^2F^o_{2\frac{1}{2}}$
8286. 7	10*h*	8286. 63	12064. 22	4. 22	$6p\ ^2P^o_{0\frac{1}{2}} - 10s\ ^2S_{0\frac{1}{2}}$
8249. 1	2*h*	8248. 93	12119. 46	9. 47	$6p\ ^2P^o_{1\frac{1}{2}} - 9d\ ^2D_{1\frac{1}{2}}$
8238. 8	30*Hl*	8238. 64	12134. 59	4. 58	$6p\ ^2P^o_{1\frac{1}{2}} - 9d\ ^2D_{2\frac{1}{2}}$
8070. 3	3*H*	8070. 18	12387. 90	7. 89	$5d\ ^2D_{2\frac{1}{2}} - 9f\ ^2F^o_{3\frac{1}{2}}$
8055. 0	2*H*	8054. 98	12411. 27	1. 27	$5d\ ^2D_{1\frac{1}{2}} - 9f\ ^2F^o_{2\frac{1}{2}}$
8050. 9	20*Hl*	8050. 81	12417. 70	7. 65	$6p\ ^2P^o_{0\frac{1}{2}} - 9d\ ^2D_{1\frac{1}{2}}$
8010. 0	7*h*	8009. 93	12481. 07	1. 07	$6p\ ^2P^o_{1\frac{1}{2}} - 11s\ ^2S_{0\frac{1}{2}}$
.....	.....	7903. 92	12648. 47	8. 47	$5d\ ^2D_{2\frac{1}{2}} - 10f\ ^2F^o_{3\frac{1}{2}}$
.....	.....	7889. 28	12671. 94	1. 92	$5d\ ^2D_{1\frac{1}{2}} - 10f\ ^2F^o_{2\frac{1}{2}}$
7871. 8	2*H*	7871. 71	12700. 23	0. 27	$6p\ ^2P^o_{1\frac{1}{2}} - 10d\ ^2D_{1\frac{1}{2}}$
7864. 5	10*Hl*	7864. 27	12712. 24	2. 23	$6p\ ^2P^o_{1\frac{1}{2}} - 10d\ ^2D_{2\frac{1}{2}}$
7823. 0	5*h*	7823. 08	12779. 17	9. 25	$6p\ ^2P^o_{0\frac{1}{2}} - 11s\ ^2S_{0\frac{1}{2}}$
.....	.....	7785. 33	12841. 14	1. 14	$5d\ ^2D_{2\frac{1}{2}} - 11f\ ^2F^o_{3\frac{1}{2}}$
.....	.....	7771. 26	12864. 39	4. 38	$5d\ ^2D_{1\frac{1}{2}} - 11f\ ^2F^o_{2\frac{1}{2}}$
.....	.....	7697. 6	12987. 5	7. 50	$5d\ ^2D_{2\frac{1}{2}} - 12f\ ^2F^o_{3\frac{1}{2}}$
7691. 2	6*Hl*	7691. 04	12998. 57	8. 45	$6p\ ^2P^o_{0\frac{1}{2}} - 10d\ ^2D_{1\frac{1}{2}}$
7628. 0	4*H*	7627. 83	13006. 28	6. 29	$6p\ ^2P^o_{1\frac{1}{2}} - 11d\ ^2D_{2\frac{1}{2}}$
7464.	2*H*	7463. 48	13394. 89	4. 90	$6p\ ^2P^o_{0\frac{1}{2}} - 11d\ ^2D_{1\frac{1}{2}}$
6900. 14	1000	6900. 13	14488. 49	8. 48	$6s\ ^2S_{0\frac{1}{2}} - 7p\ ^2P^o_{0\frac{1}{2}}$
6847. 45	2000	6847. 44	14599. 97	9. 97	$6s\ ^2S_{0\frac{1}{2}} - 7p\ ^2P^o_{1\frac{1}{2}}$

TABLE 4. *Atomic energy levels of* In I

Electron configuration	Term symbol	J	Level value	Interval
			cm^{-1}	
$5s^2(^1S)$ $5p$	$5p\ ^2P^\circ$	$0\frac{1}{2}$	*0. 00*	2212. 56
		$1\frac{1}{2}$	*2212. 56*	
$5s^2(^1S)$ $6s$	$6s\ ^2S$	$0\frac{1}{2}$	24372. 87	
$5s^2(^1S)$ $6p$	$6p\ ^2P^\circ$	$0\frac{1}{2}$	*31816. 61*	298. 18
		$1\frac{1}{2}$	*32114. 79*	
$5s^2(^1S)$ $5d$	$5d\ ^2D$	$1\frac{1}{2}$	32892. 12	23. 30
		$2\frac{1}{2}$	32915. 42	
$5s\ 5p^2$	$5p^2\ ^4P$	$0\frac{1}{2}$	34977. 66	1043. 14
		$1\frac{1}{2}$	36020. 80	1431. 10
		$2\frac{1}{2}$	37451. 90	
$5s^2(^1S)$ $7s$	$7s\ ^2S$	$0\frac{1}{2}$	36301. 69	
$5s^2(^1S)$ $7p$	$7p\ ^2P^\circ$	$0\frac{1}{2}$	*38861. 35*	111. 49
		$1\frac{1}{2}$	*38972. 84*	
$5s^2(^1S)$ $6d$	$6d\ ^2D$	$1\frac{1}{2}$	39048. 48	49. 89
		$2\frac{1}{2}$	39098. 37	
$5s\ 5p^2$	$5p^2\ ^2D$	$1\frac{1}{2}$	39707. 29	0. 67
		$2\frac{1}{2}$	39707. 96	
$5s^2(^1S)$ $8s$	$8s\ ^2S$	$0\frac{1}{2}$	40636. 71	
$5s^2(^1S)$ $8p$	$8p\ ^2P^\circ$	$0\frac{1}{2}$	*41827. 10*	54. 34
		$1\frac{1}{2}$	*41881. 44*	
$5s^2(^1S)$ $7d$	$7d\ ^2D$	$1\frac{1}{2}$	41836. 23	25. 34
		$2\frac{1}{2}$	41861. 57	
$5s^2(^1S)$ $5f$	$5f\ ^2F^\circ$	$2\frac{1}{2}$, $3\frac{1}{2}$	*42220. 0*	
$5s^2(^1S)$ $9s$	$9s\ ^2S$	$0\frac{1}{2}$	42718. 55	
$5s^2(^1S)$ $8d$	$8d\ ^2D$	$1\frac{1}{2}$	43335. 63	18. 99
		$2\frac{1}{2}$	43354. 62	
$5s^2(^1S)$ $9p$	$9p\ ^2P^\circ$	$0\frac{1}{2}$	*43369. 09*	30. 44
		$1\frac{1}{2}$	*43399. 53*	
$5s^2(^1S)$ $6f$	$6f\ ^2F^\circ$	$2\frac{1}{2}$, $3\frac{1}{2}$	*43584. 4*	
$5s^2(^1S)$ $10s$	$10s\ ^2S$	$0\frac{1}{2}$	43880. 83	
$5s^2(^1S)$ $9d$	$9d\ ^2D$	$1\frac{1}{2}$	44234. 26	15. 11
		$2\frac{1}{2}$	44249. 37	
$5s^2(^1S)$ $10p$	$10p\ ^2P^\circ$	$0\frac{1}{2}$	*44275. 17*	18. 96
		$1\frac{1}{2}$	*44294. 13*	
$5s^2(^1S)$ $7f$	$7f\ ^2F^\circ$	$2\frac{1}{2}$	*44406. 20*	0. 06
		$3\frac{1}{2}$	*44406. 26*	
$5s^2(^1S)$ $11s$	$11s\ ^2S$	$0\frac{1}{2}$	44595. 86	
$5s^2(^1S)$ $10d$	$10d\ ^2D$	$1\frac{1}{2}$	44815. 06	11. 96
		$2\frac{1}{2}$	44827. 02	
$5s^2(^1S)$ $11p$	$11p\ ^2P^\circ$	$0\frac{1}{2}$	[*44853. 23*]	[12. 56]
		$1\frac{1}{2}$	*44865. 79*	
$5s^2(^1S)$ $8f$	$8f\ ^2F^\circ$	$3\frac{1}{2}$	*44938. 70*	−0. 01
		$2\frac{1}{2}$	*44938. 71*	
$5s^2(^1S)$ $12s$	$12s\ ^2S$	$0\frac{1}{2}$	45067. 19	

UNIVERSITY OF MICHIGAN LIBRARIES

TABLE 4. *Atomic energy levels of* In I—Continued

Electron configuration	Term symbol	J	Level value	Interval
			cm^{-1}	
$5s^2(^1S)11d$	11d ^2D	$1\frac{1}{2}$ $2\frac{1}{2}$	45211. 51 45221. 08	9. 57
$5s^2(^1S)$ 9*f*	9*f* $^2F°$	$3\frac{1}{2}$ $2\frac{1}{2}$	*45303. 31* *45303. 39*	−0. 08
$5s^2(^1S)13s$	13*s* ^2S	$0\frac{1}{2}$	45394. 13	
$5s^2(^1S)12d$	12*d* ^2D	$1\frac{1}{2}$ $2\frac{1}{2}$	45493. 98 45502. 04	8. 06
$5s^2(^1S)10f$	10*f* $^2F°$	$3\frac{1}{2}$ $2\frac{1}{2}$	*45563. 89* *45564. 04*	−0. 15
$5s^2(^1S)14s$	14*s* ^2S	$0\frac{1}{2}$	45630. 44	
$5s^2(^1S)13d$	13*d* ^2D	$1\frac{1}{2}$ $2\frac{1}{2}$	45702. 08 45709. 02	6. 94
$5s^2(^1S)11f$	11*f* $^2F°$	$2\frac{1}{2}$ $3\frac{1}{2}$	*45756. 50* *45756. 56*	0. 06
$5s^2(^1S)15s$	15*s* ^2S	$0\frac{1}{2}$	45806. 88	
$5s^2(^1S)14d$	14*d* ^2D	$1\frac{1}{2}$ $2\frac{1}{2}$	45859. 30 45865. 32	6. 02
$5s^2(^1S)12f$	12*f* $^2F°$	$2\frac{1}{2}$ $3\frac{1}{2}$	--- *45902. 92*	
$5s^2(^1S)15d$	15*d* ^2D	$1\frac{1}{2}$, $2\frac{1}{2}$	45986. 69	
---	---	---	---	
In II ($^1S_0$)	*Limit*		**46669. 93**	
$5s\ 5p^2$	$5p^2$ ^2P	$0\frac{1}{2}$ $1\frac{1}{2}$	59650 60660	1010

TABLE 5. *First spectrum of thallium*, Tl I

[*h*=hazy, *H*=very hazy, *l*=shaded to longer waves]

Wavelength	Intensity and character	Wavelength Paschen [4]	Intensity Paschen [4]	Wave number		Term combination
				Observed	Calculated	
A		*A*		cm^{-1}	cm^{-1}	
13013. 2	2	13013. 8	700	7682. 4	2. 1	$7s\ ^2S_{0\frac{1}{2}} - 7p\ ^2P^o_{0\frac{1}{2}}$
.....	.....	12736. 4	150	7849. 4	51. 8	$7p\ ^2P^o_{0\frac{1}{2}} - 7d\ ^2D_{1\frac{1}{2}}$
.....	.....	12728. 2	20	7854. 4	....	.....
.....	.....	12491. 8	15	8003. 1	5. 2	$7p\ ^2P^o_{1\frac{1}{2}} - 9s\ ^2S_{0\frac{1}{2}}$
.....	.....	11690. 7	10	8551. 5	....	.....
11592. 9	5*hl*	11594. 5	80	8623. 6	3. 6	$6d\ ^2D_{2\frac{1}{2}} - 6f\ ^2F^o_{3\frac{1}{2}}$
11512. 82	1000	11513. 22	1000	8683. 59	3. 2	$7s\ ^2S_{0\frac{1}{2}} - 7p\ ^2P^o_{1\frac{1}{2}}$
11483. 7	4*hl*	11482. 2	50	8705. 6	5. 5	$6d\ ^2D_{1\frac{1}{2}} - 6f\ ^2F^o_{2\frac{1}{2}}$
11101. 61	5*h*	.....	....	9005. 24	6. 6	$7p\ ^2P^o_{0\frac{1}{2}} - 9s\ ^2S_{0\frac{1}{2}}$
.....	.....	10496. 4	80	9524. 5	11. 8	$7p\ ^2P^o_{1\frac{1}{2}} - 8d\ ^2D_{1\frac{1}{2}}$
10488. 80	40*hl*	10492. 5	50	9531. 37	1. 9	$7p\ ^2P^o_{1\frac{1}{2}} - 8d\ ^2D_{2\frac{1}{2}}$
.....	.....	10292. 3	60	9713. 3	22. 4	$7s\ ^2S_{0\frac{1}{2}} - 6d\ ^2D_{2\frac{1}{2}}$
10011. 9	30*hl*	.....	....	9985. 4	5. 4	$6d\ ^2D_{2\frac{1}{2}} - 7f\ ^2F^o_{3\frac{1}{2}}$
9937. 4	2*h*	.....	....	10060. 2	59. 0	$7p\ ^2P^o_{1\frac{1}{2}} - 6p^2\ ^4P_{0\frac{1}{2}}$
9930. 4	20*hl*	.....	....	10067. 3	7. 3	$6d\ ^2D_{1\frac{1}{2}} - 7f\ ^2F^o_{2\frac{1}{2}}$
9863. 4	10*h*	.....	....	10135. 7	6. 0	$7p\ ^2P^o_{1\frac{1}{2}} - 10s\ ^2S_{0\frac{1}{2}}$
9509. 4	40*hl*	9512. 8	30	10513. 0	3. 1	$7p\ ^2P^o_{0\frac{1}{2}} - 8d\ ^2D_{1\frac{1}{2}}$
9252. 6	2*H*	.....	....	10804. 8	4. 7	$6d\ ^2D_{2\frac{1}{2}} - 8f\ ^2F^o_{3\frac{1}{2}}$
9183. 1	2*H*	.....	....	10886. 6	6. 6	$6d\ ^2D_{1\frac{1}{2}} - 8f\ ^2F^o_{2\frac{1}{2}}$
.....	.....	9171. 1	20	10900. 8	....	.....
9130. 5	20*hl*	.....	....	10949. 3	9. 5	$7p\ ^2P^o_{1\frac{1}{2}} - 9d\ ^2D_{2\frac{1}{2}}$
9038. 4	3	.....	....	11060. 9	0. 2	$7p\ ^2P^o_{0\frac{1}{2}} - 6p^2\ ^4P_{0\frac{1}{2}}$
8976. 75	5*h*	.....	....	11136. 8	7. 2	$7p\ ^2P^o_{0\frac{1}{2}} - 10s\ ^2S_{0\frac{1}{2}}$
8850. 4	4*h*	.....	....	11295. 8	5. 4	$7p\ ^2P^o_{1\frac{1}{2}} - 11s\ ^2S_{0\frac{1}{2}}$
8474. 27	10*hl*	.....	....	11797. 2	7. 0	$7p\ ^2P^o_{1\frac{1}{2}} - 10d\ ^2D_{2\frac{1}{2}}$
8373. 6	20*hl*	8376. 5	10	11939. 0	8. 9	$7p\ ^2P^o_{0\frac{1}{2}} - 9d\ ^2D_{1\frac{1}{2}}$
8130. 0	8*h*	.....	....	12296. 7	6. 6	$7p\ ^2P^o_{0\frac{1}{2}} - 11s\ ^2S_{0\frac{1}{2}}$
7815. 80	10*hl*	.....	....	12791. 1	0. 4	$7p\ ^2P^o_{0\frac{1}{2}} - 10d\ ^2D_{1\frac{1}{2}}$
7678. 93	2*h*	.....	....	13019. 1	9. 2	$7p\ ^2P^o_{0\frac{1}{2}} - 12s\ ^2S_{0\frac{1}{2}}$
7493. 6	3*hl*	.....	....	13341. 1	1. 8	$7p\ ^2P^o_{0\frac{1}{2}} - 11d\ ^2D$
6713. 80	300	.....	....	14890. 59	0. 8	$7s\ ^2S_{0\frac{1}{2}} - 8p\ ^2P_{0\frac{1}{2}}$
6549. 84	1000	.....	....	15263. 34	3. 5	$7s\ ^2S_{0\frac{1}{2}} - 8p\ ^2P^o_{1\frac{1}{2}}$

UNIVERSITY OF MICHIGAN LIBRARIES

TABLE 6. *Atomic energy levels of* Tl I

Electron configuration	Term symbol	J	Level value	Interval
			cm^{-1}	
$6s^2(^1S)$ $6p$	$6p\ ^2P^\circ$	$0\frac{1}{2}$	*0. 0*	7792. 7
		$1\frac{1}{2}$	*7792. 7*	
$6s^2(^1S)$ $7s$	$7s\ ^2S$	$0\frac{1}{2}$	26477. 5	
$6s^2(^1S)$ $7p$	$7p\ ^2P^\circ$	$0\frac{1}{2}$	*34159. 6*	1001. 2
		$1\frac{1}{2}$	*35160. 8*	
$6s^2(^1S)$ $6d$	$6d\ ^2D$	$1\frac{1}{2}$	36118. 0	81. 9
		$2\frac{1}{2}$	36199. 9	
$6s^2(^1S)$ $8s$	$8s\ ^2S$	$0\frac{1}{2}$	38745. 9	
$6s^2(^1S)$ $8p$	$8p\ ^2P^\circ$	$0\frac{1}{2}$	*41368. 3*	372. 7
		$1\frac{1}{2}$	*41741. 0*	
$6s^2(^1S)$ $7d$	$7d\ ^2D$	$1\frac{1}{2}$	42011. 4	37. 6
		$2\frac{1}{2}$	42049. 0	
$6s^2(^1S)$ $5f$	$5f\ ^2F^\circ$	$2\frac{1}{2}$, $3\frac{1}{2}$	*42318. 4*	
$6s^2(^1S)$ $9s$	$9s\ ^2S$	$0\frac{1}{2}$	43166. 2	
$6s^2(^1S)$ $9p$	$9p\ ^2P^\circ$	$0\frac{1}{2}$	*44380. 9*	181. 6
		$1\frac{1}{2}$	*44562. 5*	
$6s^2(^1S)$ $8d$	$8d\ ^2D$	$1\frac{1}{2}$	44672. 7	20. 0
		$2\frac{1}{2}$	44692. 7	
$6s^2(^1S)$ $6f$	$6f\ ^2F^\circ$	$2\frac{1}{2}$, $3\frac{1}{2}$	*44823. 5*	
$6s\ ^6p^2$	$6p^2\ ^4P$	$0\frac{1}{2}$	45219. 8	4600
		$1\frac{1}{2}$	49820.	3226
		$2\frac{1}{2}$	53046.	
$6s^2(^1S)10s$	$10s\ ^2S$	$0\frac{1}{2}$	45296. 8	
$6s^2(^1S)10p$	$10p\ ^2P^\circ$	$0\frac{1}{2}$	*45939. 3*	104. 3
		$1\frac{1}{2}$	*46043. 6*	
$6s^2(^1S)$ $9d$	$9d\ ^2D$	$1\frac{1}{2}$	46098. 5	11. 8
		$2\frac{1}{2}$	46110. 3	
$6s^2(^1S)$ $7f$	$7f\ ^2F^\circ$	$2\frac{1}{2}$, $3\frac{1}{2}$	*46185. 3*	
$6s^2(^1S)11s$	$11s\ ^2S$	$0\frac{1}{2}$	46456. 2	
$6s^2(^1S)11p$	$11p\ ^2P^\circ$	$0\frac{1}{2}$	*46853. 8*	63. 3
		$1\frac{1}{2}$	*46917. 1*	
$6s^2(^1S)10d$	$10d\ ^2D$	$1\frac{1}{2}$	46950. 0	7. 8
		$2\frac{1}{2}$	46957. 8	
$6s^2(^1S)$ $8f$	$8f\ ^2F^\circ$	$2\frac{1}{2}$, $3\frac{1}{2}$	*47004. 6*	
$6s^2(^1S)12s$	$12s\ ^2S$	$0\frac{1}{2}$	47178. 8	
$6s^2(^1S)12p$	$12p\ ^2P^\circ$	$0\frac{1}{2}$	*47442. 6*	34. 8
		$1\frac{1}{2}$	*47477. 4*	
$6s^2(^1S)11d$	$11d\ ^2D$	$1\frac{1}{2}$, $2\frac{1}{2}$	47501. 4	
$6s^2(^1S)13s$	$13s\ ^2S$	$0\frac{1}{2}$	47654. 7	
$6s^2(^1S)13p$	$13p\ ^2P^\circ$	$0\frac{1}{2}$, $1\frac{1}{2}$	*47847. 7*	
$6s^2(^1S)12d$	$12d\ ^2D$	$1\frac{1}{2}$, $2\frac{1}{2}$	47876. 0	
$6s^2(^1S)14s$	$14s\ ^2S$	$0\frac{1}{2}$	47983. 2	
$6s^2(^1S)14p$	$14p\ ^2P^\circ$	$0\frac{1}{2}$, $1\frac{1}{2}$	*48129. 6*	

TABLE 6. *Atomic energy levels of* Tl I—Continued

Electron configuration	Term symbol	J	Level value	Interval
			cm^{-1}	
$6s^2(^1S)13d$	$13d\ ^2D$	$1\frac{1}{2}$, $2\frac{1}{2}$	48142. 3	
$6s^2(^1S)15s$	$15s\ ^2S$	$0\frac{1}{2}$	48223. 2	
$6s^2(^1S)15p$	$15p\ ^2P^\circ$	$0\frac{1}{2}$, $1\frac{1}{2}$	*48331. 2*	
$6s^2(^1S)14d$	$14d\ ^2D$	$1\frac{1}{2}$, $2\frac{1}{2}$	48339. 3	
$6s^2(^1S)16s$	$16s\ ^2S$	$0\frac{1}{2}$	48399. 5	
$6s^2(^1S)16p$	$16p\ ^2P^\circ$	$0\frac{1}{2}$, $1\frac{1}{2}$	*48459. 5*	
$6s^2(^1S)15d$	$15d\ ^2D$	$1\frac{1}{2}$, $2\frac{1}{2}$	48488. 6	
$6s^2(^1S)17s$	$17s\ ^2S$	$0\frac{1}{2}$	48534. 8	
$6s^2(^1S)16d$	$16d\ ^2D$	$1\frac{1}{2}$, $2\frac{1}{2}$	48604. 0	
$6s^2(^1S)18s$	$18s\ ^2S$	$0\frac{1}{2}$	48639. 0	
$6s^2(^1S)17d$	$17d\ ^2D$	$1\frac{1}{2}$, $2\frac{1}{2}$	48696. 5	
$6s^2(^1S)19s$	$19s\ ^2S$	$0\frac{1}{2}$	48726. 2	
$6s^2(^1S)18d$	$18d\ ^2D$	$1\frac{1}{2}$, $2\frac{1}{2}$	48770. 5	
$6s^2(^1S)20s$	$20s\ ^2S$	$0\frac{1}{2}$	48796. 2	
$6s^2(^1S)19d$	$19d\ ^2D$	$1\frac{1}{2}$, $2\frac{1}{2}$	48828. 6	
$6s^2(^1S)20d$	$20d\ ^2D$	$1\frac{1}{2}$, $2\frac{1}{2}$	48878. 2	
$6s^2(^1S)21d$	$21d\ ^2D$	$1\frac{1}{2}$, $2\frac{1}{2}$	48920. 6	
$6s^2(^1S)22d$	$22d\ ^2D$	$1\frac{1}{2}$, $2\frac{1}{2}$	48957. 7	
$6s^2(^1S)23d$	$23d\ ^2D$	$1\frac{1}{2}$, $2\frac{1}{2}$	48988. 9	
---	---	---	---	
Tl II ($^1S_0$)	*Limit*		**49264.2**	

4. References

[1] C. E. Moore, Atomic energy levels as derived from the analyses of optical spectra, NBS Circular 467, II (in press).
[2] F. Paschen and K. Meissner, Ann. Physik **348,** 1223 (1914).
[3] F. Paschen, Ann. Physik **424,** 148 (1938).
[4] F. Paschen, Ann. Physik **29,** 625 (1909); **33,** 717 (1910).
[5] H. D. Curtis, J. Opt. Soc. Am. Rev. Sci. Instr. **8,** 697 (1924).
[6] W. F. Meggers and K. Burns, Sci. Pap. BS **18,** 191 (1922) S441.
[7] H. Kayser, Handbuch der Spectroscopie **5,** 460 (1910); H. Kayser and H. Konen, Handbuch der Spectroscopie **7,** 500 (1934).
[8] F. Exner and E. Haschek, Die Spektren der Elemente bei normalen Druck **II,** 98 (1911).
[9] H. S. Uhler and J. W. Tanch, Astrophys. J. **55,** 291 (1922).
[10] R. A. Sawyer and R. J. Lang, Phys. Rev. **34,** 718 (1929).
[11] A. Fowler, Report on series in line spectra (Fleetway Press, London, 1922).
[12] E. Klein, Astrophys. J. **56,** 373 (1922).
[13] H. Kayser and C. Runge, Wiedem. Ann. **48,** 126 (1893).
[14] H. Kayser and R. Ritschl, Tabelle der Hauptlinien der Linienspektren aller Elemente (Springer, Berlin, 1939).
[15] W. R. S. Garton, Proc. Phys. Soc. A, **64,** 509 (1951).
[16] H. Kayser, Handbuch der Spectroscopie **6,** 709 (1912).
[17] J. M. Eder and E. Valenta. Wien. Ber. **119,** IIa, 519 (1910).

WASHINGTON, November 27, 1951.

UNIVERSITY OF MICHIGAN LIBRARIES

Journal of Research of the National Bureau of Standards Vol. 48, No. 4, April 1952 Research Paper 2321

On the Truncation Error in the Solution of Laplace's Equation by Finite Differences[1]

Wolfgang Wasow

The difference between the solution of the Laplace differential equation and the Laplace difference equation, defined in the same rectangle and assuming the same boundary values, is estimated under the assumption that the boundary function possesses a bounded third derivative. The bound obtained is of the order of magnitude of the square of the mesh length.

1. Introduction

Probably the most widely used approach for the numerical solution of differential equations for which simple analytic solutions are not available consists in replacing the differential equation by a finite difference equation. The difference between the exact solutions of these two problems is usually called—somewhat inappropriately—the *truncation error*.

It is highly desirable, for numerical calculations, to have adequate estimates of this truncation error. There exist in the literature numerous investigations of this problem. We shall be primarily concerned with the case of the first boundary value problem for elliptic partial linear differential equations. Some references to the literature for this case are listed at the end of this paper. All these investigations, as far as they are mathematically complete, suffer from the defect that the estimates given depend on bounds for the derivatives of the unknown solution of the differential equation itself. Such bounds can in general not be found without effectively solving the differential equation. Thus the value of these estimates consists essentially in giving information about the order of magnitude of the truncation error in terms of the mesh length used, and in helping to form reasonable guesses as to the size of the error.

It turns out that, with the difference expressions used in most numerical work, and for a square net of mesh length h the truncation error is of the order $O(h^2)$, provided the boundary values and the equations of the boundary curve C possess *bounded fourth derivatives*, and provided the boundary values of the difference equation problem are suitably adjusted (see, e. g. [3][2]). This estimate is then valid in the whole domain B.

The bound for the truncation error given by P. C. Rosenbloom in [6] is somewhat different. It depends only on the modulus of continuity in $B+C$ of the unknown harmonic function, but it is a pointwise estimate that deteriorates indefinitely at points near the boundary.

Thus there remain a number of unsolved problems of theoretical as well as computational interest: The ideal would be a pointwise estimate of the truncation error, valid if the boundary curve and the boundary values are piecewise analytic. This error estimate should have the highest possible order in h, and, at the same time, it should not be unduly wasteful. It should, of course, depend only on quantities that can be easily computed from the data.

From the *theoretical* viewpoint the order of magnitude of the error is the most interesting quantity. In particular, one would like to know the exact way in which a weakening of the smoothness required of the data affects the global and local order of the error.

For *computational* purposes an estimate will be most useful if it yields small bounds for the error at moderate sizes of h. Thus $10h$ is a better bound in practice than $10{,}000h^2$.

The contents of this note are intended as a first exploratory step toward the examination of these questions. The error estimate for Laplace's equation in a rectangle given below in formulas (18) and (19) is of order $O(h^2)$, with coefficients of moderate size, although it depends on bounds for the *third* derivatives of the boundary values only, and in spite of the fact that a rectangle is a domain with corners. It is hoped that this special result may help to stimulate more general investigations.

2. Truncation Error for Dirichlet's Problem in a Rectangle

Let B be the rectangle with vertices (0,0), (1,0), (1,b), (0,b) where b is a rational number. The prescribed boundary function f is assumed to be continuous on the boundary C of B and to possess bounded *third* derivatives on each closed side of C.

We denote the Laplacian, as usual, by Δu and write $\Delta_h v$ for the expression

$$\frac{1}{h^2}[v(x+h,y)+v(x-h,y)+v(x,y+h)+v(x,y-h)-4v(x,y)].$$

For any value of h such that $1/h$ and b/h are integers we denote by $u_h(x,y)$ the function, defined at all netpoints (nh, mh) in $B+C$, where n,m are integers, for which

$$\Delta_h u_h = 0, \quad \text{in } B$$

and

$$u_h = f, \quad \text{on } C.$$

If u designates the solution of the corresponding Dirichlet problem for the operator Δ, then we are concerned with the truncation error $u-u_h$.

[1] This project was sponsored (in part) by the Office of Naval Research.

[2] Figures in brackets indicate the literature references at the end of this paper.

It is desirable to deal with boundary values that vanish at the four vertices. To this end we introduce the harmonic polynominal $Q(x,y)$, defined by $b\cdot Q(x,y)=A_{00}(x-1)(y-b)-A_{10}x(y-b)+A_{1b}xy-A_{0b}(x-1)y$, where A_{00}, A_{10}, etc. are the values of f at the vertices. This function solves both the difference and the differential equation. If we replace the boundary values f by

$$f^*=f-Q,$$

we obtain therefore a new problem for which the truncation error is the same as for the original problem, since the truncation error corresponding to the boundary problem determined by the values of $Q(x,y)$ on C is zero. It is clear that f^* vanishes at the vertices. Also the second and higher derivatives of f^* are the same as those of f.

The truncation error can be considered the sum of four terms, each corresponding to boundary values that are zero except on one of the four sides of the rectangle. Therefore, we assume temporarily that f^* is zero except on the side $y=0$. There $f^*=f^*(x)$ is a function of x alone.

The solutions of $\Delta u=0$ and $\Delta_h u_h=0$ for these boundary values can be written, respectively,

$$u(x,y)=\sum_{n=1}^{\infty} c_n g(y,n\pi)\sin n\pi x, \tag{1}$$

$$u_h(x,y)=\sum_{n=1}^{1/h} \gamma_n g(y,\beta_n/h)\sin n\pi x, \tag{2}$$

where

$$c_n=2\int_0^1 f^*(t)\sin n\pi t\,dt \tag{3}$$

$$\gamma_n=2h\sum_{r=1}^{1/h} f^*(rh)\sin n\pi rh \tag{4}$$

$$g(y,z)=\sinh(b-y)z/\sinh bz, \tag{5}$$

and β_n is the solution of

$$\sinh\frac{\beta_n}{2}=\sin\frac{nh\pi}{2}. \tag{6}$$

These well-known formulas can be readily verified by substitution.

We next collect a few facts needed for the comparison of u and u_h.

To find an estimate of the Fourier coefficients c_n we integrate the right member of formula (3) by parts three times, obtaining the formula

$$c_n=\frac{2}{(n\pi)^3}[(-1)^{n-1}f''(1)-f''(0)]+\frac{2}{(n\pi)^3}\int_0^1 f'''(t)\cos n\pi t\,dt. \tag{7}$$

This implies

$$|c_n|\le Kn^{-3}, \tag{7}$$

where

$$K=\frac{2}{\pi^3}[|f''(1)|+|f''(0)|]+\frac{4}{\pi^3}\max|f'''(x)|. \tag{8}$$

The Fourier coefficients c_n and the "interpolation coefficients", γ_n, are related by the equation

$$\gamma_n=C_n+\sum_{k=1}^{\infty}(c_{2k/h+n}-c_{2k/h-n}),\quad (n=1,2,\ldots,1/h).$$

This relation can readily be proved by expressing $f^*(rh)$ in (4) by its Fourier series. (See also the references in [7].) Combining (7) with the last formula we find, for $n\le 1/h$,

$$|c_n-\gamma_n|\le K\sum_{k=1}^{\infty}\{(2k/h+n)^{-3}+(2k/h-n)^{-3}\}$$
$$\le K\frac{h^3}{8}\left\{\left(1+\frac{nh}{2}\right)^{-3}+\left(1-\frac{nh}{2}\right)^{-3}+\int_1^{\infty}\left[\left(x+\frac{nh}{2}\right)^{-3}+\left(x-\frac{nh}{2}\right)^{-3}\right]dx\right\}.$$

Hence,

$$|c_n-\gamma_n|\le 1.7Kh^3,\quad \text{for } n\le 1/h. \tag{9}$$

Next we need an estimate of the difference $g(y,n\pi)-g(y,\beta_n/h)$. To this end we express $\beta_n/2$, as given by (6), in terms of $nh\pi/2$ by means of Taylor's formula. A straightforward calculation shows that

$$\frac{\beta_n}{2}=\frac{nh\pi}{2}+\left(\frac{nh\pi}{2}\right)^3 R$$

where R is the value of

$$-\frac{1}{3}\cos\sigma(1-2\sin^2\sigma)(1+\sin^2\sigma)^{-5/2}$$

at a certain mean value of σ in the interval

$$0<\sigma<nh\pi/2.$$

Hence

$$|\beta_n-nh\pi|\le(nh\pi)^3/12. \tag{10}$$

In order to estimate the difference $g(y,n\pi)-g(y,\beta_n/h)$ with the help of the theorem of the mean we have to estimate the right member of the formula

$$\frac{d}{dz}g(y,z)=\frac{1}{2}\sinh^{-2}bz\times\{(2b-y)\sinh yz-y\sinh(2b-y)z\}. \tag{11}$$

We observe that $\sinh t/t$ is an increasing function of t, for $t>0$. Therefore,

$$0\le\frac{d}{dz}g(y,z)\le\frac{y}{2}\sinh^{-2}bz\sinh(2b-y)z,\quad \text{for } z\ge 0,\ y\ge 0. \tag{12}$$

UNIVERSITY OF MICHIGAN LIBRARIES

This expression we shall apply the inequalities

$$\sinh kt \leq e^{(k-1)t} \sinh t, \quad \text{for } 0 \leq k \leq 1, \tag{13}$$

and

$$\sinh t \geq \frac{1}{2}(1-e^{-2t_1})e^t, \quad t \geq t_1 > 0. \tag{14}$$

The second of these inequalities is obvious. The first follows from

$$\sinh kt / \sinh t = e^{(k-1)t}(1-e^{-2kt})/(1-e^{-2t}).$$

we shall need the inequalities

$$\frac{4}{3} n \leq \beta_n/h \leq \pi n, \quad \text{for } 1 \leq n \leq 1/h. \tag{15}$$

The second of these is a consequence of (6); the first can be proved as follows:

$$\sinh \frac{\beta_n}{2} = \frac{nh\pi}{2}\left(\sin \frac{nh\pi}{2} \Big/ \frac{nh\pi}{2}\right) \geq \frac{nh\pi}{2} \cdot \frac{2}{\pi} = nh,$$

and

$$\sinh \frac{\beta_n}{2} \leq \frac{nh\pi}{2} < \frac{\pi}{2}.$$

Since $\sinh x/x$ is an increasing function of x for $x=0$,

$$\sinh \frac{\beta_n}{2} \Big/ \frac{\beta_n}{2} \leq \frac{\pi}{2} \Big/ \operatorname{arsinh} \frac{\pi}{2} \leq \frac{3}{2}.$$

Hence

$$\frac{\beta_n}{2} \geq \frac{2}{3} \sinh \frac{\beta_n}{2} \geq \frac{2}{3} nh,$$

which completes the proof of (15). Applying (13), (14) and (15) to (12) we obtain

$$\left|\frac{d}{dz} g(y,z)\right| \leq (1-e^{-8b/3})^{-1} y e^{-yz}, \text{ for } \begin{cases} 1 \leq n \leq 1/h \\ \beta_n/h < z < n\pi \\ 0 \leq y \leq b \end{cases}$$

and therefore, using (10),

$$\left|g(y, \frac{\beta_n}{h} - g(y, n\pi)\right| \leq (1-e^{-8b/3})^{-1} \frac{\pi^3}{12} y e^{-4\pi y/3} n^3 h^2, \quad \text{for } 1 \leq n \leq 1/h. \tag{16}$$

We conclude these preparatory remarks with the inequality

$$0 \leq g(y,z) \leq 1, \quad \text{for } 0 \leq y \leq b, \tag{17}$$

which is an immediate consequence of the definition of $g(y,z)$.

We are now ready to estimate $|u-u_h|$. To this end we write, using (1) and (2),

$$|u-u_h| \leq R_1 + R_2 + R_3,$$

$$R_1 = \sum_{n=1}^{1/h} |c_n - \gamma_n| g(y, n\pi)$$

$$R_2 = \sum_{n=1}^{1/h} |\gamma_n| \cdot |g(y, n\pi) - g(y, \beta_n/h)|$$

$$R_3 = \sum_{n=1+1/h}^{\infty} |c_n| g(y, n\pi).$$

From (9) and (17) we conclude that

$$R_1 \leq 1.7Kh^2$$

and from (7) it follows that

$$R_3 \leq K \sum_{n=1+1/h}^{\infty} n^{-3} = Kh^2/2.$$

In order to estimate R_2, we note that, in view of (7) and (9),

$$|\gamma_n| \leq K(n^{-3} + 1.7h^3).$$

Using also (16) we obtain, by summation,

$$R_2 \leq (1-e^{-8b/3})^{-1} K(2.7) \frac{\pi^3}{12} y(e^{4y/3}-1)^{-1} h^2.$$

Since

$$y/(e^{4y/3}-1) \leq \frac{3}{4}, \quad \text{for } y \geq 0,$$

this yields

$$R_2 \leq 5.24(1-e^{-8b/3})^{-1} Kh^2$$

and, hence, adding these inequalities,

$$|u-u_h| \leq [2.3 + 5.24(1-e^{-8b/3})^{-1}] Kh^2.$$

If we denote by M_2 the numerical maximum of the second derivative of the given boundary function at the vertices of the rectangle, and by M_3 the numerical maximum, anywhere on C, of the third derivative of the boundary function, the last inequality can be replaced, in view of (8), by

$$|u-u_h| \leq [.297 + .676(1-e^{-8b/3})^{-1}][M_2 + .319M_3]h^2.$$

Finally, if the sides of the rectangle are A, B instead of 1,b a homothetic transformation yields the formula

$$|u-u_h| \leq [.297 + .676(1-e^{-8B/3A})^{-1}][M_2 + .319AM_3]h^2.$$

We recall that this formula is valid only for boundary values that vanish except on the side $y=0$. For the full truncation error three analogous expressions have to be added to the right member of the last inequality, leading—with some rounding off to shorten the expression—to

$$\begin{aligned} |u-u_h| \leq {} & [.6 + 1.4(1-e^{-8B/3A})^{-1}][M_2 + .32AM_3]h^2 \\ & + [.6 + 1.4(1-e^{-8A/3B})^{-1}][M_2 + .32BM_3]h^2. \end{aligned} \tag{18}$$

For the square of side A this reduces to

$$|u-u_h| \leq (4.3M_2+1.4AM_3)h^2. \quad (19)$$

Added in proof: The function

$$u_h^*(x,y)=\sum_{n=1}^{\infty} c_n g(y,\beta_n/h) \sin n\pi x$$

coincides with $u_h(x,y)$ at all net points. Its use instead of $u_h(x,y)$ simplifies the calculations somewhat and leads to better estimates for the truncation error, namely

$$|u-u_h^*| \leq [.13+.5(1-e^{-8B/3A})^{-1}][M_2+0.32AM_3]h^2$$
$$+[.13+.5(1-e^{-8B/3A})^{-1}][M_2+0.32BM_3]h^2$$

and

$$|u-u_h^*| \leq (1.4M_2+0.43AM_3)h^2$$

instead of (18) and (19).

3. References

[1] L. F. Richardson, The approximate arithmetic solution by finite differences of physical problems involving differential equations, etc., Phil. Trans. [A] **210**, 307 to 357 (1911).

[2] S. Gerschgorin, Fehlerabschätzung für das Differenzenverfahren zur Lösung partieller Differentialgleichungen, Z. Angew. Math. Mech. [4] **10**, 373 to 382 (1930).

[3] L. Collatz, Bemerkungen zur Fehlerabschätzung für das Differenzenverfahren bei partiellen Differentialgleichungen, Z. Angew. Math. und Mech. **12**, 56 to 57 (1933).

[4] L. Collatz, Das Differenzenzenverfahren mit höherer Approximation für lineare Differentialgleichungen, Schriften des Mathematischen Seminars, Univ. Berlin **3**, 1 to 34 (1935).

[5] M. Inoue, Sur les fonctions de noeud et leurs applications à l'integration numérique des équations aux dérivées partielles, Mem. Faculty Science, Kyusyu Univ. [A], IV, No. 2, 107 to 178 (1949).

[6] P. C. Rosenbloom, The difference equation method for solving the Dirichlet problem, To appear in Proc. of a Symposium on the Construction and Application of Conformal Maps, NBS Applied Mathematics Series.

[7] H. Burkhardt, Trigonometrische Interpolation, Enzyklopädie der mathematischen Wissenschaften [A] II, 9A, p. 651 (1904).

Los Angeles, July 26, 1951.

University of Michigan Libraries